

**Microstructural Investigation of Current Barriers in  
High Temperature Superconducting  
Tapes and Coated Conductors**

**by**

**Jodi Reeves**

A dissertation submitted in partial fulfillment of the requirements  
for the degree of

Doctor of Philosophy

(Materials Science Program)

at the

UNIVERSITY OF WISCONSIN – MADISON

2001

## Acknowledgements

I would like to thank a number of people who have helped me at various times during my graduate school career: my advisors (official and unofficial) Sue Babcock, Eric Hellstrom, and David LARBALÉSTIER; my thesis committee members Mark RZCHOWSKI and Chang-Beom EOM; present and past members of ASC including Xueyan Song, Mark Rikel, Wei Zhang, Nicole Scarbrough, Matt Feldmann, Ron Parella, John Anderson, Bill Starch, Milan Polak, Jyh-Lih Wang, I-Fei Tsu, Yuehong Wu, Mei Zhou, and Na Zhang. Various undergraduate students have helped me with experiments including REU students Vivian Irizarry, Chris Reinsel, Candice Williams, Max Siker, and Darrin Adolphs; Chem 116 students Matt McGinley, Anders Olson, Laura Ellwein, David Zwicky, and Maura Jenkins; and student hourly Allison Arndt. Many staff members of the Materials Science Center, especially Rick Noll, have aided me with equipment when “Ctrl-alt-del” didn’t do the trick.

These experiments wouldn’t have been possible without those who provided samples or aided with BEKP or FIB analysis: Tim Peterson and coworkers at Air Force Research Laboratory; Ron Feenstra and Amit Goyal and coworkers at Oak Ridge National Laboratory; David Dingley at TSL, Pat Camus and David Rohde at Noran Instruments, Richard McLaughlin at Oxford Instruments, and Bill Carmichael at MATC.

I would also like to thank the staff of the Applied Superconductivity Center and Material Science Program and Department including Chris Kailhofer, Lynn Neis, and Diana Rhoads. Melinda Adams deserves a special thank you for being a great friend, administrator, social event

coordinator, and source of good advice on a wide variety of topics that range from career counseling to finding the best watering holes in Madison.

Finally, I would like to thank my family and “adopted family” for their patience, encouragement and support throughout my grad school career: John, Pat, Jana, Rob, Julie, Jason, Simon, Angie, Valerie and the Nelson and Kailhofer clans, Joan and Kathy. I am finally getting a real job.

## ***Table of Contents***

<b>PROJECT SUMMARY .....</b>	<b>1</b>
<b>1. INTRODUCTION TO CURRENT BARRIERS IN HIGH TEMPERATURE SUPERCONDUCTORS .....</b>	<b>4</b>
1-1. MOTIVATION.....	4
1-2. COMPARISON OF YBCO AND Bi-2212 .....	5
1-3. Bi-2212 SUPERCONDUCTORS .....	9
1-4. YBCO COATED CONDUCTORS .....	13
1-5. OVERVIEW OF THESIS WORK .....	16
1-6. REFERENCES .....	17
<b>2. BSCCO STUDIES .....</b>	<b>20</b>
2-1. OVERPRESSURE PROCESSING OF Ag-SHEATHED Bi-2212 MONOCORE TAPES.....	21
2-2. OVERPRESSURE PROCESSING OF Ag-SHEATHED Bi-2212 MULTIFILAMENTARY TAPES.....	31
2-3. PAIR PROCESSING OF Ag-SHEATHED Bi-2212 MONOCORE TAPES .....	41
2-4. SUMMARY .....	49
2-5. REFERENCES .....	50
<b>3. YBCO ANALYSIS TECHNIQUES.....</b>	<b>52</b>
3-1. BACKSCATTERED ELECTRON KIKUCHI PATTERN ANALYSIS TO DETERMINE CRYSTAL ORIENTATION .....	52
3-2. MAGNETO-OPTICAL IMAGING TO IDENTIFY CURRENT BLOCKING DEFECTS .....	67
3-3. FOCUSED ION BEAM TECHNOLOGY TO INVESTIGATE GRAIN BOUNDARY MICROSTRUCTURE.....	70
3-4. REFERENCES .....	72
<b>4. YBCO STUDIES.....</b>	<b>74</b>
4-1. ORIGIN OF CURRENT BARRIERS .....	74

4-2. DISTRIBUTION OF NICKEL GRAIN BOUNDARIES .....	81
4-3. INFLUENCE OF NICKEL GRAIN BOUNDARIES .....	103
4-4. SUMMARY .....	125
4-5. REFERENCES .....	126
<b>5. CONCLUSIONS .....</b>	<b>128</b>
<b>6. APPENDIX .....</b>	<b>131</b>

## Project Summary

Microstructural barriers to supercurrent occur on many length scales in all high temperature superconductors. Eliminating microstructural barriers is key to making these potentially valuable materials more favorable for commercial applications. In silver-sheathed  $\text{Bi}_2\text{Sr}_2\text{CaCu}_2\text{O}_x$  (Bi-2212) tapes and multifilaments, the principal barriers on the scale of 10-100's of microns are bubbling, porosity, second phase particles, and poorly aligned grains. In the early part of this thesis work, trapped gases inside the silver sheath that caused bubbling were identified. Two of the processing means that have been proposed for reduction of bubbling and porosity and enhancement of grain alignment in Bi-2212 were investigated. Overpressure processing was shown to stop the bubbling of the silver sheath and decrease porosity in the Bi-2212 core. The preanneal and intermediate rolling (PAIR) process developed by researchers at the Japanese National Research Institute for Metals was found to reduce the size and volume fraction of porosity and second phase particles in the superconducting core. Also, PAIR optimized grain alignment at the superconductor/silver interface. These two improvements in microstructure resulted in increased critical current density ( $J_c$ ) of Bi-2212 tapes and multifilaments.

In state-of-the-art  $\text{YBa}_2\text{Cu}_3\text{O}_x$  (YBCO) coated conductors, supercurrent barriers on the 0.1-100 $\mu\text{m}$  scale are grain boundaries. This thesis work clarifies the role of grain boundaries in the nickel substrate of RABiTS (Rolling Assisted Biaxially Textured Substrate) coated conductors. The combined techniques of plan-view SEM imaging, focused ion beam cutting,

magneto-optical imaging, and grain orientation mapping were used to determine barriers to supercurrent.

Experiments showed enhanced magnetic flux penetration, and hence reduced  $J_c$ , in the YBCO above nearly all nickel grain boundaries that have misorientation angles ( $\theta$ ) greater than  $4^\circ$ , independent of the rotation axis, in samples from the Air Force Research Laboratory. Similarly, reduced  $J_c$  was found in the YBCO above most nickel grain boundaries with  $\theta > 5^\circ$  in state-of-the-art samples from Oak Ridge National Laboratory.  $\theta > 4-5^\circ$  grain boundaries in the substrate were not randomly distributed, but rather clustered. The detrimental effect of clustering is best illustrated using grain boundary maps instead of the hitherto more commonly published percolation maps. Monochromatic percolation maps imply that there is a fully connected current path through the YBCO microstructure that is within the chosen tolerance angle criterion of the map. However, it is the grain boundary map that displays the constrictions of the current path. Therefore, grain boundary maps are better tools for illustrating supercurrent barriers than percolation maps.

Grain boundary maps and grain orientation maps were used to investigate how the texture of the substrate was transferred to the buffer layers and to the superconductor. Most grain boundaries in the nickel were replicated in the buffer and superconductor layers with the same misorientation angle. Approximately 9% of the grain boundaries in the buffer layer had lower misorientation angles ( $1.9^\circ \pm 0.9^\circ$ ) compared to the underlying nickel grain boundaries, while 8% of YSZ boundaries had higher misorientation angles ( $1.6^\circ \pm 0.8^\circ$ ) than the underlying nickel boundaries. This variation in misorientation angle from substrate to buffer may be due to mosaic spread in the buffer layer. Anisotropic growth and/or surface energy minimization may be

responsible for the improvement in c-axis alignment in the YBCO compared to the buffer layer. However, the YBCO mosaic spread did not eliminate high angle grain boundaries, since  $>5^\circ$  boundaries were still seen in YBCO grain boundary maps.

The results of this study on microstructural current barriers show that  $J_c$  improvements in RABiTS-type coated conductors require the reduction of  $\theta > 4-5^\circ$  boundaries in the nickel substrate.

# 1. Introduction to Current Barriers in High Temperature Superconductors

## ***1-1. Motivation***

Almost fifteen years ago, the breakthrough discovery of high-temperature superconductors [1] promised to make superconducting technology widespread. These copper oxide ceramic materials, such as  $\text{YBa}_2\text{Cu}_3\text{O}$  (YBCO) with a transition temperature at approximately 90K [2], only have to be cooled with liquid nitrogen to become superconducting. Therefore, high temperature superconductors would be more economical and more easily engineered into systems than low-temperature superconductors such as  $\text{Nb}_3\text{Sn}$  and  $\text{NbTi}$ . Over the past decade, expectations have remained high regarding the potential uses of high temperature superconductors for electric power generation and distribution devices such as wire, cables, motors, generators, transformers, and fault current limiters [3]. One project currently underway is replacing copper cables with high temperature superconducting wire in a utility power grid in downtown Detroit [3]. However, to achieve commercially viable conductors for broader-based applications, it is necessary to increase the supercurrent-carrying capability of the superconductor, which has proven to be difficult.

Current barriers in high temperature superconductors are microstructural in character and occur on many different length scales: nanometer-sized disruptions at grain boundaries, micron-sized second phase particles and voids, and millimeter-sized cracks. The diagram in Figure 1-1 lists these microstructural defects and the range of length scales on which they arise. The defects

that control critical current density ( $J_c$ ) in  $\text{Bi}_2\text{Sr}_2\text{CaCu}_2$  (Bi-2212) superconductors on the micron and millimeter scale include bubbling of the silver sheath, porosity, second phase particles, and grain alignment. In the recently developed YBCO coated conductors, grain boundaries on the scale of hundreds of nanometers to tens of microns are the primary obstacles to current flow in the superconducting layer.

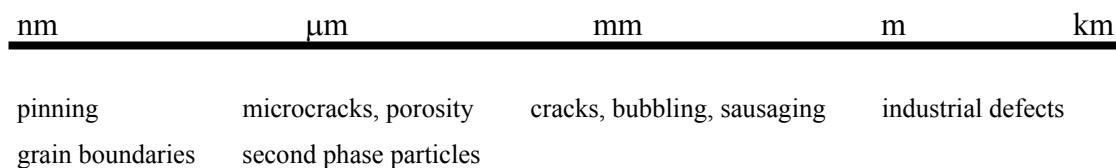


Figure 1-1. Diagram showing defects in high temperature superconductors on different length scales.

The general problem to be addressed in this thesis is current-limiting defects in two types of high temperature superconductors: polycrystalline oxide powder-in-tube Bi-2212 tapes and YBCO coated conductors. The next section begins by comparing and contrasting the electromagnetic properties, microstructural properties, and manufacturability of Bi-2212 and YBCO. Subsequent sections will describe processing and current barriers in each material.

## **1-2. Comparison of YBCO and Bi-2212**

YBCO grown epitaxially on single crystalline substrates has  $J_c = 2\text{-}4 \times 10^6 \text{ A/cm}^2$  (0T, 77K) and strong flux pinning properties that make this material a candidate for high current and high field applications at 77K. Figure 1-2 shows that compared to BSCCO compounds, YBCO has a much larger irreversibility field ( $B^*$ ) – the maximum magnetic field for loss-free current [4]. However, a major factor limiting  $J_c$  in YBCO is weak electromagnetic coupling across grain

boundaries [5-13]. YBCO bicrystal studies have investigated the dependence of the grain boundary  $J_c$  on the grain boundary misorientation [14-19]. Figure 1-3 shows that the ratio of grain boundary  $J_c$  to grain  $J_c$  decreases with increasing misorientation angle. In this figure, Heinig et. al. [17, 19] showed for [001] tilt grain boundaries with misorientation angles  $>7^\circ$ , the  $J_c$  across a boundary can be reduced to a very small fraction of the  $J_c$  in the grain interior. This weak link behavior makes it necessary for long lengths of YBCO to contain few, if any, high angle grain boundaries in order to optimize  $J_c$  for commercial applications. The needed degree of texture in the superconductor has only recently been achieved in short lengths of the coated conductor.

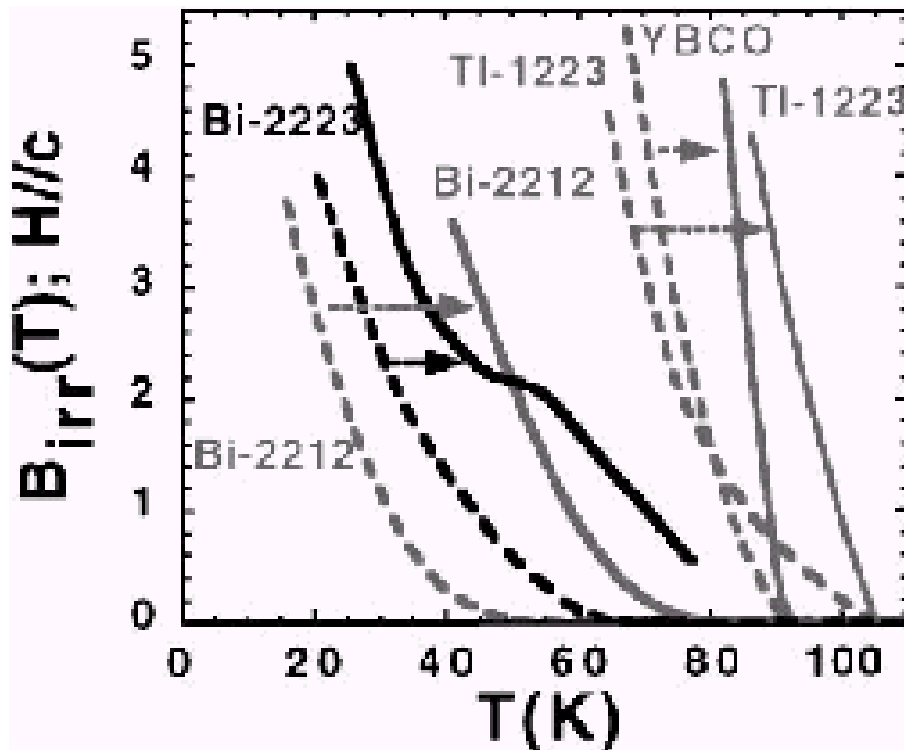


Figure 1-2. Comparison of irreversibility fields for different high temperature superconductors. The solid lines are from samples with optimum pinning. From [4].

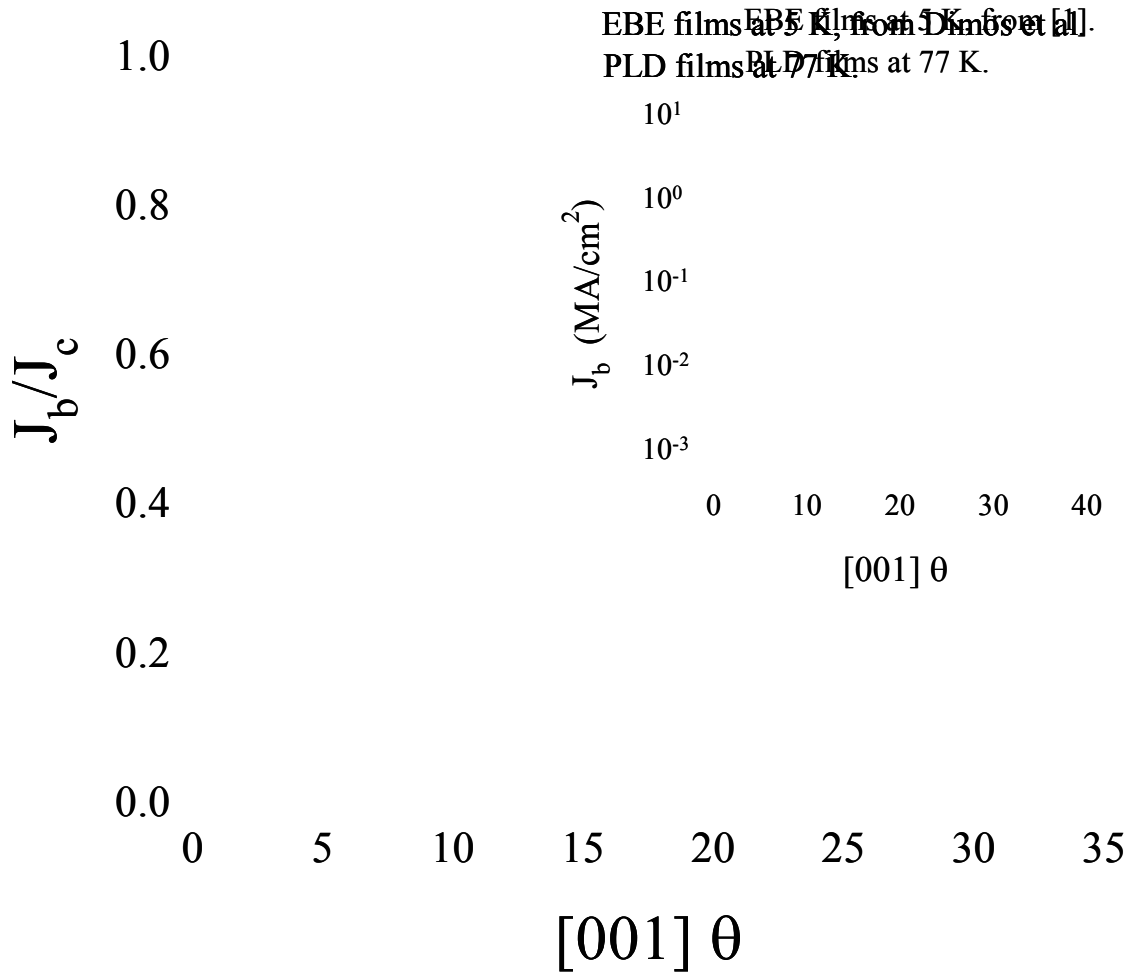


Figure 1-3: Graph showing the ratio of grain boundary  $J_c$  to grain  $J_c$  ( $J_b/J_c$ ) as a function of misorientation angle ( $\theta$ ). The YBCO was grown on [001] tilt  $\text{SrTiO}_3$  bicrystals via EBE (electron beam evaporation) or PLD (pulsed laser deposition). There is a sharp drop in grain boundary  $J_c$  above  $7^\circ$ . From [19].

The main advantage of BSCCO materials is that the superconductor can be aligned mechanically in bulk scale processing. Reasonably high  $J_c$  values ( $10^4 \text{ A/cm}^2$ ) have been obtained in long lengths of commercially produced polycrystalline wires. Thermomechanical processing of Bi-2212, including wire drawing, tape rolling, and furnace heat treatment, leads to a

crystallographically textured grain structure. However, the superconducting properties of Bi-2212 at 77K are not as favorable as YBCO; the strongly two-dimensional nature of the electronic structure in Bi-2212 leads to poor flux pinning in the grains until the temperature is reduced below 30K. Thus, Bi-2212 is a viable alternative to low temperature superconductors in high magnetic field applications such as an insert magnet in magnetic resonance imaging (MRI) devices [20], but its potential applications at and near 77K are few.

Disadvantages of both superconductors are that they are brittle ceramics and susceptible to fracturing under small applied stresses. Bi-2212 is therefore encased in a silver sheath and YBCO is grown on buffer layers on nickel tape to give flexibility and strength to the conductor form.

### **1-3. Bi-2212 Superconductors**

#### **Processing**

This section will describe the methods used to process, on a laboratory scale, Bi-2212 tapes (monocore and multifilamentary). Bi-2212 tapes are fabricated using the oxide powder-in-tube (OPIT) process schematically shown in Figure 1-4. Precursor powders of  $\text{Bi}_2\text{O}_3$ ,  $\text{SrCO}_3$ ,  $\text{CaCO}_3$ , and  $\text{CuO}$  are prereacted to form Bi-2212 powder that is packed into a silver tube. The tube is sealed and drawn through successively smaller diameter dies to form a thin wire. The wire is then rolled into a green tape, which for these experiments was approximately 150  $\mu\text{m}$  thick and 3 mm wide. Wire can also be bundled together and put into another silver sheath, then drawn and rolled, to form multifilamentary conductors. Figure 1-5 shows typical transverse cross-sections illustrating the geometry of Bi-2212 tape and multifilaments. In these experiments the number of filaments and size of the multifilamentary tape was varied.

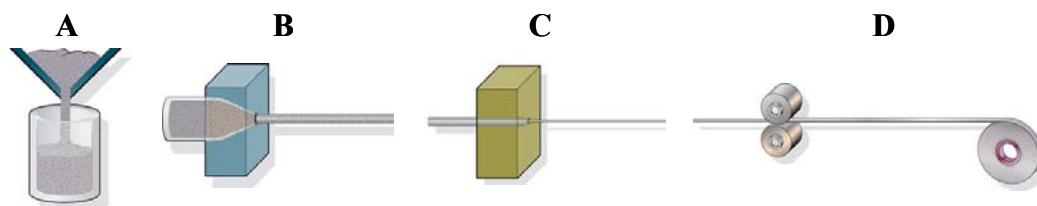


Figure 1-4. Schematic drawing of the OPIT process for producing Bi-2212 tape. The powder is packed into a silver tube (A), drawn into wire (B;C), and rolled into tape (D). From [3].

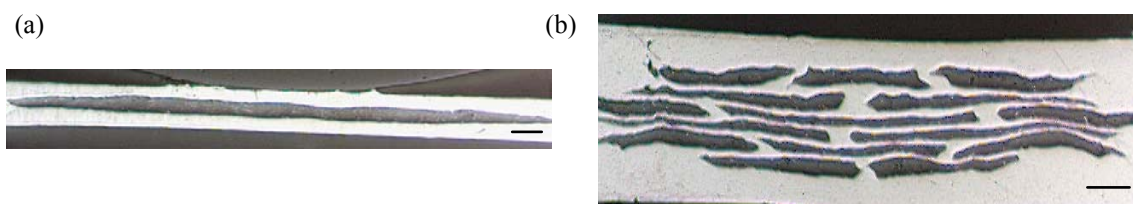


Figure 1-5. Light micrographs of (a) Bi-2212 tape and (b) Bi-2212 multifilamentary tape after melt-processing. The black material is Bi-2212 encased in a silver sheath. Length marker represents 200 μm.

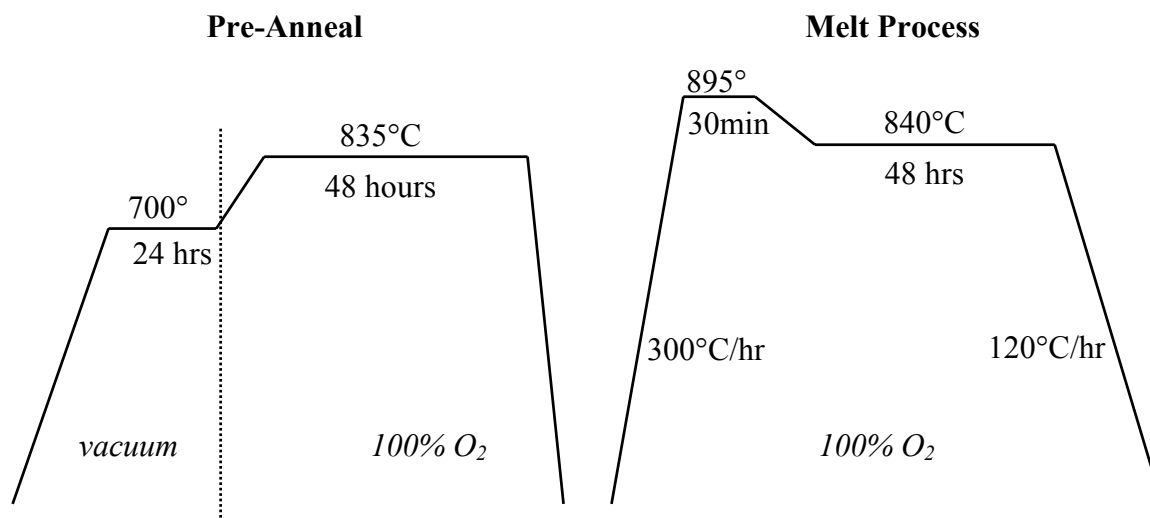


Figure 1-6. Schematic drawing of the heat treatment of Bi-2212 tapes and multifilaments.

The green tape is heat treated (Figure 1-6) in a furnace in order to fully melt the precursor powder and regrow the superconducting grains by solidification. Among the high temperature superconductors, this heat treatment, called melt processing, is unique to Bi-2212 material. Another commercially available high temperature superconductor,  $\text{Bi}_2\text{Sr}_2\text{Ca}_2\text{Cu}_3\text{O}_x$  (Bi-2223), is also produced by an OPIT process but it is not melt-processed. Adjustment of the various heat treatment parameters (time, temperatures, oxygen partial pressure ( $p\text{O}_2$ )) is necessary for optimization of the volume fraction and crystallographic alignment of the superconducting grains. The growth of significant volume fractions of second phase particles during melt processing has remained a significant problem in Bi-2212 processing.

There are many issues that remain to be solved for scaling up these laboratory-scale processing methods to the industrial scale. For Bi-2212, scale-up issues include the difficulty of obtaining a uniform hot zone in large furnaces necessary for long lengths of conductor and isolated bubbling in kilometer lengths of tape. Also, laboratory heat treatments are conducted in low thermal mass furnaces that are capable of “fast” cooling ( $700^\circ\text{C}/\text{hr}$ ), which is not possible with furnaces with large thermal masses.

### **Current barriers**

The defects believed to be primary barriers to current flow in silver-sheathed Bi-2212 polycrystalline tapes and multifilaments occur on the mm scale (macroscale) and the  $\mu\text{m}$  scale (microscale). On the macroscale, bubbling of the silver sheath [21-23] occurs when gases (water and  $\text{CO}_2$ ) cause the sheath to distend and huge pores to form in the superconducting core.

Bubbling causes  $J_c$  to fall to nearly zero in the bubbled area. On the microscale, only about 10% of the superconductor volume carries current. The other 90% contains small pores, second phase particles, and misaligned grains, as shown in Figure 1-7 and Figure 1-8, which disrupt the current. These defects arise during the heat treatment of the superconducting tapes. The most productive (best for  $J_c$ ) heat treatment requires melting and resolidification of 2212 powders that are encased in silver. Upon melting,  $O_2$  evolution can cause porosity. After the Bi-2212 powder inside the silver sheath melts at  $870^\circ\text{C}$ , second phase particles nucleate and grow. This growth disturbs the formation, growth, and alignment of the superconducting grains [24]. Research on improving the heat treatment of state-of-the-art Bi-2212 tapes focuses on eliminating defects such as pores as well as reducing the number and size of second phase particles.

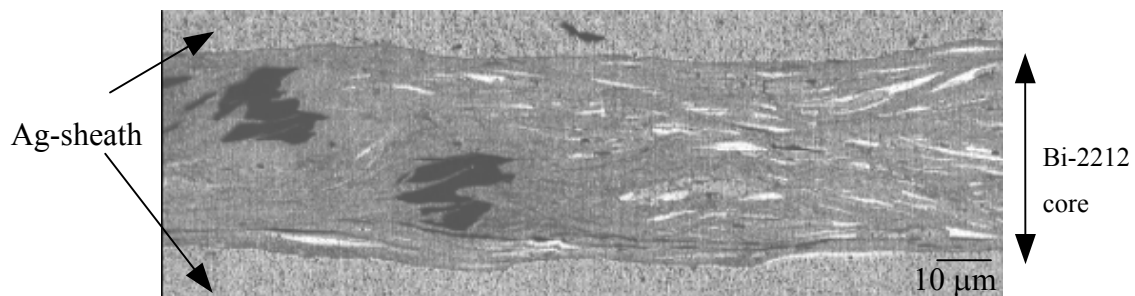


Figure 1-7. Scanning electron microscope (SEM) image of a longitudinal cross-section of Bi-2212 tape. The light gray matrix is Bi-2212. The dark gray and white particles are second phase particles that are not superconducting.

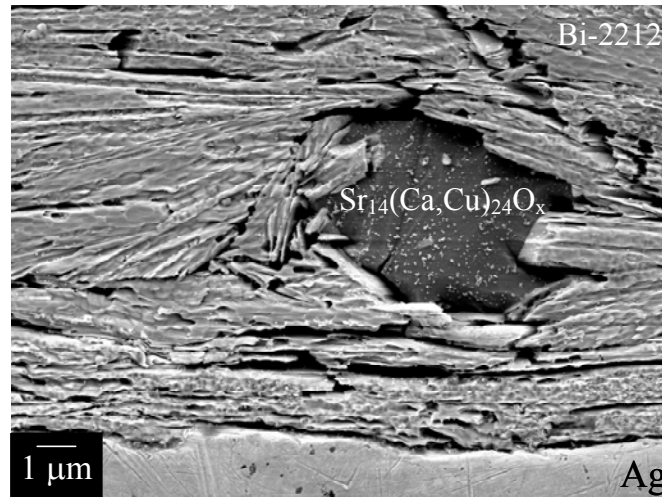


Figure 1-8. SEM image of a longitudinal cross-section of Bi-2212 tape showing grain misalignment in the region of a non-superconducting second phase particle of  $\text{Sr}_{14}(\text{Ca,Cu})_{24}\text{O}_x$ .

#### **1-4. YBCO Coated Conductors**

YBCO films with the highest  $J_c$  are grown on single crystal substrates. Since it is impractical to make long lengths of single crystal oxide substrates, alternate substrates that are inexpensive, easily manufactured, strong and flexible are needed. The two principle methods of producing high  $J_c$  YBCO films on well-textured substrates are Rolling Assisted Bi-axially Textured Substrates (RABiTS) and Ion-Beam Assisted Deposition (IBAD). A third, although less-widely used technique, is the Inclined Substrate Deposition (ISD) method. The difference between these three methods is where the texture is introduced. RABiTS use a substrate with strong biaxial texture produced by rolling and recrystallization. IBAD and ISD produce a textured buffer layer on a non-textured substrate.

A comparison of the general architecture of RABiTS and IBAD coated conductors is shown in Figure 1-9. In both methods, a thin metal tape (nickel or an alloy) is used as the initial substrate. YBCO cannot be grown epitaxially on the nickel because the nickel oxidizes to NiO in the  $\langle 111 \rangle$  orientation. Therefore, suitable oxide buffer layers are used. A common buffer layer sequence on rolled and recrystallized Ni is  $\text{CeO}_2/\text{YSZ}/\text{CeO}_2$ . The first thin epitaxial layer of  $\text{CeO}_2$  protects the metal substrate from oxidizing; it is thin to prevent cracking in the  $\text{CeO}_2$ . The next epitaxial layer of YSZ serves as a barrier for nickel diffusion from the substrate to the superconductor. YSZ is a favorable substrate due to its low cost, mechanical strength, chemical stability, and resistance to nickel diffusion. However, it has poor lattice match with YBCO. The result of poor lattice mismatch is that two YBCO orientations arise in epitaxial films:  $[100]\text{YBCO}/[100]\text{YSZ}$  and  $[100]\text{YBCO}/[110]\text{YSZ}$ . There may also be an interfacial reaction

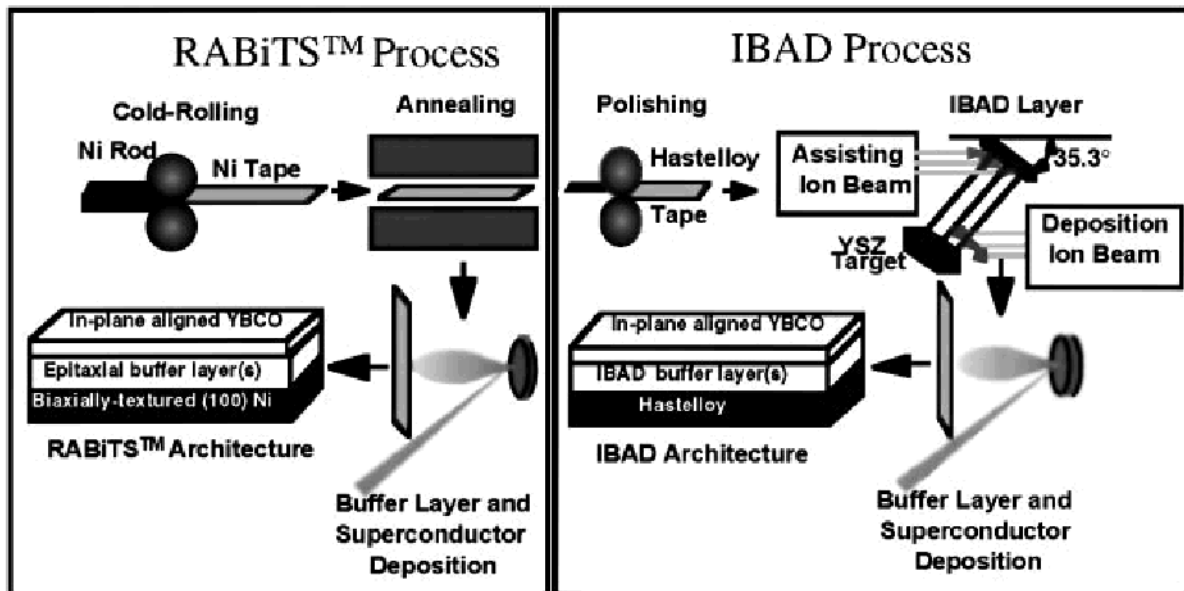


Figure 1-9. Comparison of Comparison of RABiTS and IBAD substrate architecture for YBCO coated conductors. From [4].

between the YSZ and the YBCO to form  $\text{BaZrO}_3$ . Growing a thin  $\text{CeO}_2$  layer between the YSZ and YBCO prevents  $\text{BaZrO}_3$  from forming and leads to just one epitaxial orientation [4]. The final epitaxial layer of  $\text{CeO}_2$  has a good lattice match and is chemically compatible with the YBCO layer.

The coated conductor technologies offer promising methods of producing long lengths of YBCO with a highly textured microstructure. In the RABiTS-type coated conductors, the texture produced in the rolled and recrystallized substrate should be transferred to the YBCO, reducing the density of high angle grain boundaries in the superconductor. However, many  $J_c$  enhancement issues still remain in coated conductor technology. In this work, we will focus on a crucial current-limiting factor in RABiTS-type coated conductors: the influence of the nickel texture and grain boundary network on the YBCO microstructure and properties. In addition, there are many issues that remain to be solved for scaling up these processing methods to the industrial scale. For YBCO coated conductors with sputtered buffer or superconducting layers, problems include the difficulties associated with vacuum processes such as incorporating feed-through mechanisms necessary for long lengths of conductor, reproducibility of deposition conditions, contamination, and inhomogeneity of sputter-deposited materials. Finally, it is difficult to produce uniform texture in long lengths of rolled and recrystallized metal substrates.

## **1-5. Overview of Thesis Work**

Chapter 1 introduced the “barriers to current” problem in the two high-temperature superconducting materials studied – Bi-2212 tapes and RABiTS-type YBCO coated conductors. Chapter 2 describes and discusses results published in four papers [25-28] on Bi-2212 tapes and multifilaments: the cause of bubbling and how microstructure and  $J_c$  are affected by overpressure processing and the PAIR (Pre-Anneal, Intermediate Rolling) process. The experimental techniques used to investigate the structure-property relationship between supercurrent barriers in RABiTS-type YBCO coated conductors will then be described in Chapter 3. These techniques include magneto-optical (MO) imaging to identify barriers, focused ion beam cutting to determine the origin of barriers seen in MO images, and backscattered electron Kikuchi pattern (BEKP) analysis in the scanning electron microscope to determine how crystallographic texture is affected at these barriers. Chapter 4 summarizes results [29, 30] on YBCO coated conductors and discusses how BEKP can be used to illustrate current paths in coated conductors as well as determine a “threshold angle” in the nickel substrate and the texture transfer from substrate to superconducting layer.

## 1-6. References

- [1] J.G. Bednorz and K.A. Muller, *Proceedings Comm. Eur. Communities* (Brussels, Belgium: Commission of the European Communities European Workshop on High  $T_c$  Superconductors and Potential Applications, 1987) 43.
- [2] M.K. Wu, J.R. Ashburn, C.J. Torng, P.H. Hor, R.L. Meng, L. Gao, Z.J. Huang, Y.Q. Wang and C.W. Chu, *Phys. Rev. Lett.* **58** (1987) 908-10.
- [3] ASC website: <http://www.amsuper.com>
- [4] D. Norton, *Ann. Rev. Mater. Sci.* **28** (1998) 302, and references contained therein.
- [5] J. Mannhart, P. Chaudhari, D. Dimos, C.C. Tsuei, and T.R. McGuire, *Phys. Rev. Lett.* **61** (1988) 2476-9.
- [6] S. E. Babcock, X. Cai, D.L. Kaiser, and D.C. Larbalestier, *Nature* **347** (1990) 167-9.
- [7] S.E. Babcock, *MRS Bulletin* **17** (1992) 20-6.
- [8] S.W. Chan, *Materials Science Forum* **207-209** (1996) 797-800.
- [9] C. Prouteau, G. Duscher, D.K. Christen, N.D. Browning, S.J. Pennycook, M.F. Chisholm, D.P. Norton, A. Goyal, and C. Park, *Advances in Superconductivity X* (Proceedings of the 10th International Symposium Tokyo, Japan; 1998) 1015-18.
- [10] M. Mironova, Du Guoping, and K. Salama, *IEEE Trans. Appl. Super.* **9** (1999) 1630-3.
- [11] S. Oktyabrsky, R. Kalyanaraman, K. Jagannadham, and J. Narayan, *JMR* **14** (1999) 2764-72.
- [12] N. Koshizuka, T. Takagi, J.G. Wen, K. Nakao, T. Usagawa, Y. Eltsev, and T. Machi, *Physica C* **337** (2000) 1-6.

- [13] M. Carmody, K.L Merkle, Y. Huang, L.D. Marks, and B.H. Moeckly, *Interface Science* **8** (2000) 231-42.
- [14] D. Dimos, P. Chaudhari and J. Mannhart, *Phys. Rev. B* **41** (1990) 4038-49.
- [15] M.B. Field, D.C. Larbalestier, A. Parikh, and K. Salama, *Physica C* **280** (1997) 221-233.
- [16] V.R. Todt, X.F. Zhang, D.J. Miller, M. StLouisWeber, and V.P. Dravid, *Appl. Phys. Lett.* **69** (1996) 3746-3748.
- [17] N. Heinig, R.D. Redwing, I.F. Tsu, A. Gurevich, J.E. Nordman, S.E. Babcock and D.C. Larbalestier, *Appl. Phys. Lett.* **69** (1996) 577-79.
- [18] D.T. Verebelyi, D.K. Christan, R. Feenstra, C. Cantoni, A. Goyal, D.F. Lee, P. Paranthaman, P.N. Arendt, R.F. DePaula, J.R. Groves, and C. Prouteau, *Appl. Phys. Lett.* **76**, (2000) 1755-7.
- [19] N.F. Heinig, R.D. Redwing, J.E. Nordman and D.C. Larbalestier, *Phys Rev B* **60** (1999), 1409-17.
- [20] IGC website: <http://www.igc.com/Td/pages/ADS/htsconductors.htm>
- [21] E. Hellstrom and W. Zhang, *Supercond. Sci. Technol.* **8** (1995) 317-23.
- [22] T. Hase, K. Shibusani, S. Hayashi, M. Shimada, R. Ogawa and Y. Kawate, *J. Jap. Inst. Metals* **60** (1996), 1020-28.
- [23] T. Haugan, S. Patel and D. Shaw, *Physica C* **266** (1996)183-190.
- [24] D. Yuan and J. Kajuch, *J. Supercond.* **11** (1998) 569-73.
- [25] J.L. Reeves, M. Polak, W. Zhang, E.E. Hellstrom, S.E. Babcock, D.C. Larbalestier, N. Inoue, and M. Okada, *IEEE Trans. Appl. Super.* **7** (1997) 1541-43.

- [26] J.L. Reeves, E.E. Hellstrom, V. Irizarry, and B. Lehndorff, *IEEE Trans. Appl. Super.* **9** (1999) 1836-39.
- [27] B. Lehndorff, J.L. Reeves, A. Polyanskii, M.O. Rikel, E.E. Hellstrom, and D.C. Larbalestier, *Proceedings EUCAS* (Barcelona, Spain: 4<sup>th</sup> *European Conference on Applied Superconductivity*, 1999).
- [28] J. Reeves, D. Adolphs, A. Arndt, D. Zwicky, M. Rikel, and E. Hellstrom, *Physica C* **341-348** (2000) 2021-2.
- [29] D.M. Feldmann, J.L. Reeves, A.A. Polyanskii, G. Kozlowski, R.R. Biggers, R.M. Nekkanti, I. Maartense, M. Tomsic, P. Barnes, C.E. Oberly, T.L. Peterson, S.E. Babcock, and D.C. Larbalestier, *APL* **77** (2000) 2906-8.
- [30] J.L. Reeves, D.M. Feldmann, C-Y. Yang, and D.C. Larbalestier, *IEEE Trans. Appl. Supercon.* (2001).

## 2. BSCCO Studies

Eliminating current barriers caused by microstructural defects is important in the commercialization of  $\text{Bi}_2\text{Sr}_2\text{CaCu}_2\text{O}_x$  (Bi-2212) tapes and multifilaments. These macroscale defects include bubbling of the silver sheath, porosity, second phase particle content, and superconductor grain misalignment. Trapped gases including water and  $\text{CO}_2$  caused bubbling of the silver sheath. A preannealing process at high temperature reduced the amount of water and  $\text{CO}_2$  trapped inside. However, it was not possible to remove all gases that caused bubbling, so overpressure processing was developed to counteract the effects of the residual gases that caused porosity and poor superconductor grain alignment within the monocoil and multifilamentary tapes. The effects of another process, Pre-Anneal and Intermediate Rolling (PAIR) developed by researchers in Japan, was also investigated. With optimized parameters, the PAIR process reduced porosity and improved Bi-2212 grain alignment in monocoil tapes.

This chapter is a compilation and discussion of results from four published papers [1-4] on Bi-2212 tapes and multifilaments: the cause of bubbling and how microstructure and  $J_c$  were affected by overpressure processing and the PAIR process.

## **2-1. Overpressure Processing of Ag-sheathed Bi-2212 Monocore Tapes**

### **Introduction**

A critical problem for melt-processed silver-sheathed Bi-2212 tapes is gas release during heat treatment. When meter-long lengths of Bi-2212 tapes are processed in pure oxygen at 1 atmosphere (atm) pressure, the silver sheath may bubble [5]. The tape bubbles because the gas pressure inside the tape is greater than the silver sheath yield strength and the external gas pressure. To partially prevent bubbling, the tapes could be processed in lower oxygen partial pressure ( $pO_2$ ), as researchers have seen that processing Bi-2212 tapes in air does not lead to bubbling [5]. However, researchers [6,7] have found that processing in 100% oxygen ( $pO_2=1\text{atm}$ ) results in a more homogeneous microstructure and higher  $J_c$  than processing in air ( $pO_2=0.21\text{atm}$ ). With changing  $pO_2$ , the non-superconducting second phase particle content also changes [8]. In the  $pO_2$  range from 0.075 to 0.30 atm, small  $Sr_{14}(Ca,Cu)_{24}O_x$  particles are present, while very large  $Sr_1(Ca,Cu)_1O_y$  particles form in the  $pO_2$  range from 0.40 to 1 atm. These large  $Sr_1(Ca,Cu)_1O_y$  second phase particles can span the superconductor core, resulting in lower  $J_c$ . Therefore, processing in 100%  $O_2$  is preferable to processing in air, if bubbling of the silver sheath can be eliminated.

One approach to eliminating bubbling was developed by researchers at Hitachi who used a “gas pressure melting” method with total pressure ( $P_{\text{total}}$ ) greater than 1 atm during processing of Bi-2212 wires [9]. They found that increasing  $P_{\text{total}}$  resulted in a more homogeneous

distribution of small voids in the superconductor, rather than the large bubbles, which in turn increased  $J_c$ .

We developed a similar approach called “overpressure processing” – the application of inert gas pressure above the equilibrated  $pO_2$ . In these overpressure experiments, a mixture of  $O_2$  and Ar was used. Since  $O_2$  diffuses rapidly through the silver sheath, the  $pO_2$  inside and outside the tape quickly equilibrates (the  $pO_2$  was fixed at 1atm in order to optimize the second phase particle content). In contrast, Ar does not diffuse through the silver; thus, Ar supplies an external pressure that was greater than the gas pressure inside the tape.

The effect of overpressure processing on bubbling, critical current density ( $J_c$ ), and microstructure was investigated and compared to conventionally processed tapes with different starting carbon content.

## **Experimental Procedures**

The Bi-2212 tapes with powder composition Bi:Sr:Ca:Cu = 2.1:2:1:1.95 were made using the oxide powder in tube (OPIT) process described in section 1-3-1 and had a final thickness of 140 $\mu$ m. To ascertain the role of carbon in bubble formation, two tapes with different carbon content were made. The initial carbon content of the powder was 710 ppmwt (parts per million by weight) as measured by high-temperature combustion infrared detection at Anderson Laboratories. To lower the carbon content to 220 ppmwt, the powder was heated to 700°C in partial vacuum with flowing  $O_2$  for 24 hours. The powder was made into monocoil tape using the OPIT process. Coils were made by sealing the ends of 30 cm of monocoil tape and winding

the tape around a 3.2 cm diameter MgO-coated Inconel mandrel. The two coils with 710 ppmwt and 220 ppmwt carbon were heated at 5°C/min to 900°C in pure O<sub>2</sub> with P<sub>total</sub> = 1atm, held at 900°C for 15 minutes, and then furnace cooled. This process was repeated for P<sub>total</sub> = 2 atm, 4.6 atm, 6 atm, 8 atm, and 9 atm to see what effect P<sub>total</sub> had on bubbling in low and high carbon content tapes. For P<sub>total</sub> > 1atm, an O<sub>2</sub>/Ar gas mixture was used to maintain a fixed pO<sub>2</sub> = 1atm. The gas pressure was established in the furnace before heating and was maintained with the pressurized flowing gas mixture until cooling to room temperature. The design of our overpressure furnace is unique, in that the gas mixture with fixed pO<sub>2</sub> is flowed through the furnace at constant P<sub>total</sub> throughout the heat treatment.

For the electromagnetic and microstructural characterization of fully processed tapes, short lengths (4-8 cm) of tape with sealed ends were melt processed in the overpressure furnace using the heat treatment depicted in Figure 2-1.

The cooling rate of 120°C/hr during the last step of the heat treatment was the fastest cooling rate possible with the overpressure furnace. In order to see what effect a faster cooling rate had on J<sub>c</sub>, one set of samples was processed at P<sub>total</sub> = pO<sub>2</sub> = 1atm using the same heat treatment as in Figure 2-1, except for the final cooling rate. Instead, a different furnace capable of cooling much more quickly (700°C/hr) was used.

The transport critical current was measured with multiple voltage taps over 3 cm sections using the standard four point probe technique at 0T, 4.2K, with a 1μV/cm criterion. Backscattered electron imaging was done on the JEOL JEM6100 scanning electron microscope (SEM), and energy dispersive x-ray spectroscopy (EDS) was used for phase identification.

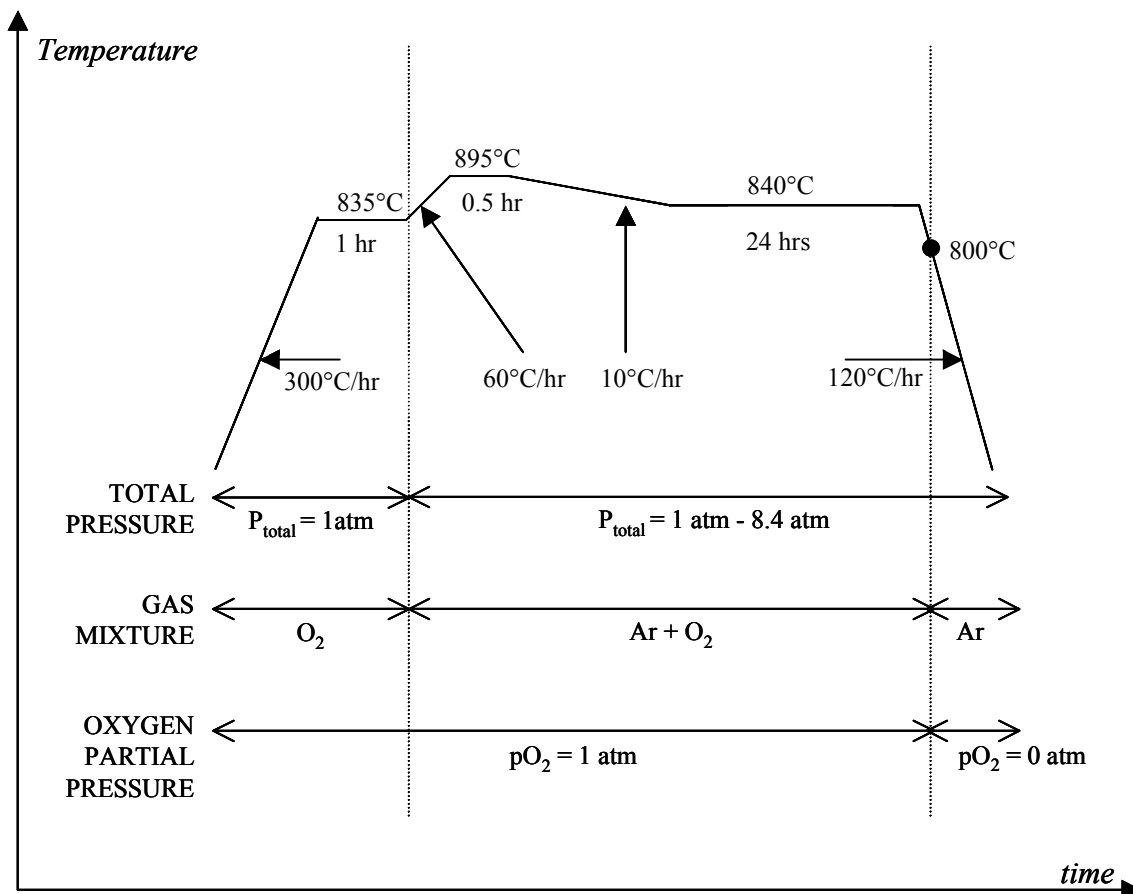


Figure 2-1. Heat treatment for Bi-2212 tapes processed in the overpressure furnace. The final cooling rate of 120°C/hr is the fastest rate possible with this furnace.

## Results and Discussion

### A. Effect of overpressure on bubbling

To illustrate the effect of carbon content and  $P_{\text{total}}$  on bubble formation in Bi-2212 coils, the length and thickness of individual bubbles that formed at a lower pressure ( $P_{\text{total}} = 2 \text{ atm}$ ,  $p_{\text{O}_2} = 1 \text{ atm}$ ) and a higher pressure ( $P_{\text{total}} = 8 \text{ atm}$ ,  $p_{\text{O}_2} = 1 \text{ atm}$ ) were measured. Figure 2-2 shows that with increasing  $P_{\text{total}}$ , the calculated volume and number of bubbles decreased for both high and

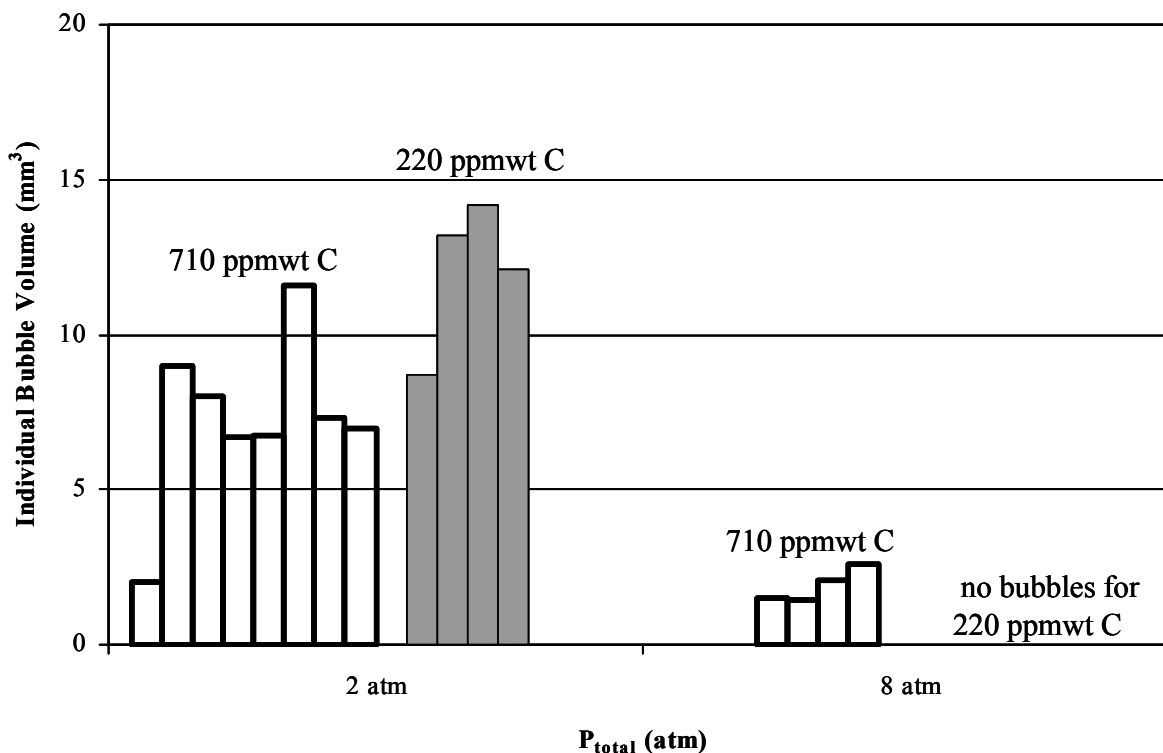


Figure 2-2. Histogram showing volume and number of bubbles for  $P_{\text{total}}=2\text{atm}$  and  $P_{\text{total}}=8\text{atm}$ ,  $p\text{O}_2=1\text{atm}$  for Bi-2212 tapes with different carbon content.

low carbon content tapes. Also, at both 2 atm and 8 atm, the high carbon content tape had more bubbles than the low carbon content tape. This result, that higher carbon content tape bubbled more, was not surprising as previous work implicated  $\text{CO}_2$  as the bubble forming gas [10].

The percentage of the tape length that bubbled was plotted as a function of  $P_{\text{total}}$  in Figure 2-3. In pure oxygen where  $P_{\text{total}} = p\text{O}_2 = 1\text{atm}$ , the entire coil bubbled. Even 1 atm of overpressure ( $P_{\text{total}}=2\text{atm}$ ) significantly reduced bubbling. The percentage of tape length that bubbled continued to slowly decrease as the overpressure increased. The  $P_{\text{total}}$  needed to eliminate bubbling increased with increasing carbon content.  $P_{\text{total}} = 8\text{atm}$  and  $P_{\text{total}} = 9\text{atm}$  eliminated bubbling in the lower and higher carbon content tapes respectively.

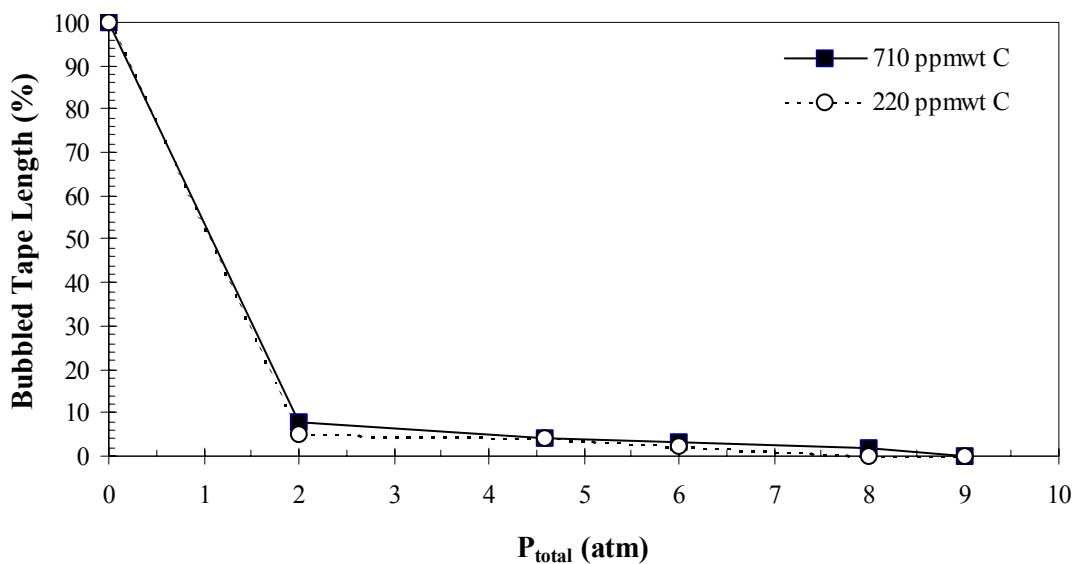


Figure 2-3. Graph of percentage of bubbled tape length vs. total pressure with  $p_{O_2}=1\text{atm}$  for tapes with different carbon content.

Applying a large enough overpressure while heating to the melting temperature stopped bubbling of the silver sheath even in high carbon content tapes. However, the trapped gas can still cause problems. The consequences of having gas still trapped inside the core were seen during a follow-up experiment conducted at Hitachi Ltd. on high carbon content tape that had overpressure applied during the entire heat treatment. One meter of tape with 500 ppmwt carbon was wrapped into a 3.2 cm diameter coil and processed in the Hitachi overpressure system with the following heat treatment at  $P_{\text{total}} = 6\text{atm}$  and  $p_{O_2} = 1\text{atm}$ : anneal at  $740^\circ\text{C}$  for 16 hours, heat to  $890^\circ\text{C}$  at  $5^\circ\text{C}/\text{min}$ , hold at  $890^\circ\text{C}$  for 30 minutes, cool at  $10^\circ\text{C}/\text{hr}$  to  $840^\circ\text{C}$ , hold at  $840^\circ\text{C}$  for 24 hours, and furnace cool to room temperature. The silver sheath did not bubble; however,  $J_c$  was low. The microstructure of this tape showed large voids in the core. Therefore, even when the outside of the silver sheath does not bubble, large voids can be present inside the core of high

carbon content tape. These voids degrade the electromagnetic properties of the superconductor. As a result, in later experiments low carbon content tape (<200ppmw) was used in conjunction with overpressure processing in order to eliminate bubbling and increase  $J_c$ .

### **B. Effect of overpressure on $J_c$**

Figure 2-4 shows that increasing  $P_{total}$  from 1atm to 8.1atm with  $pO_2 = 1atm$  results in the substantial increase in  $J_c$  for the fully processed, slow-cooled (120°C/hr) tapes. Also, there was less scatter in the  $J_c$  values at 8.1atm than at 1atm. The overpressure compressed the core during processing to encourage Bi-2212 grain alignment, reduce porosity, and thus improve the  $J_c$  of the superconductor. If this is indeed the case, overpressure-processed tapes should carry more current than conventionally processed tapes.

The data in Figure 2-4 also shows that the cooling rate has a significant effect on  $J_c$ ; the tapes that were cooled quickly (700°C/hr) had substantially higher  $J_c$  than the slow-cooled (120°C/hr) samples. However, fast cooling was not feasible for coils with a large thermal mass. Modifications in the cooling process need to be developed that allow slow cooling while retaining high  $J_c$  of overpressure-processed Bi-2212 tapes.

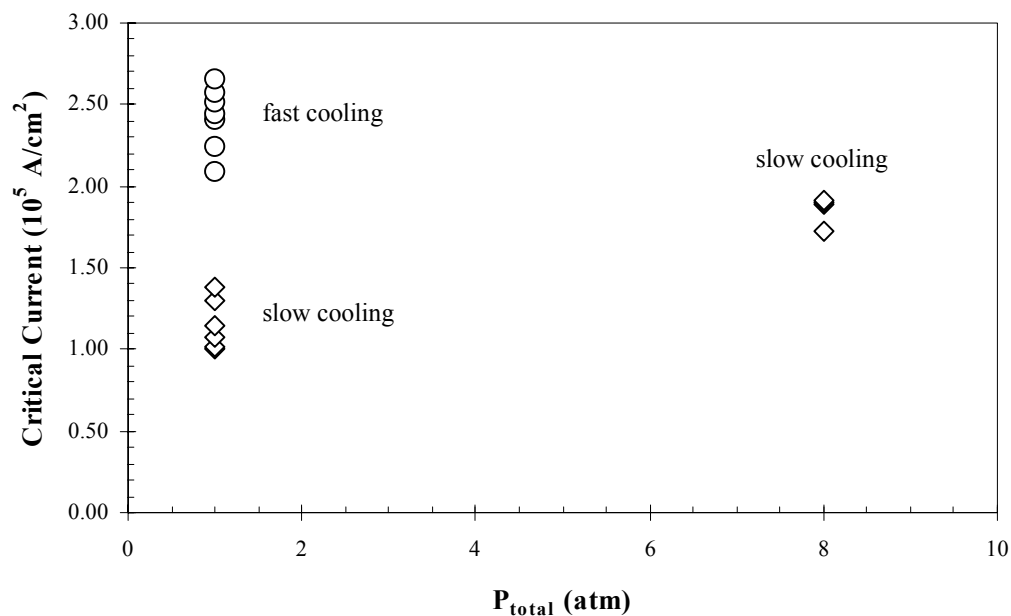


Figure 2-4.  $J_c$  vs. total pressure with fixed  $pO_2=1$ atm. The fast (700°C/hr) and slow (120°C/hr) cooling rates refer to the last step in the heat treatment shown in Figure 2-1.

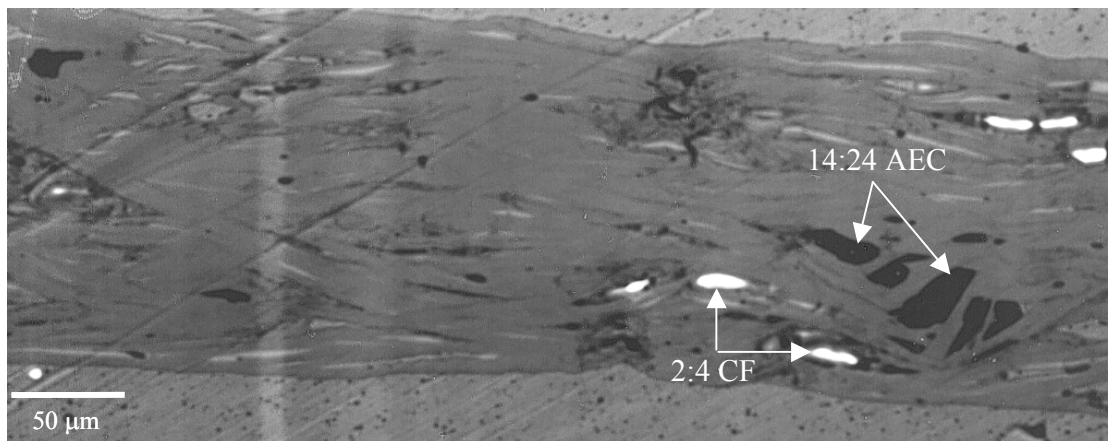


Figure 2-5. Backscattered electron image of overpressure-processed tape with furnace cooling =120°C/hr,  $P_{\text{total}}=8.1$  atm,  $p\text{O}_2=1$ atm. The non-superconducting phase particles include 14:24 AEC and 2:4 CF.

### C. Effect of overpressure on microstructure

Figure 2-5 shows a representative backscattered electron image of a sample processed in the overpressure furnace with  $P_{\text{total}} = 8.1$ atm,  $p\text{O}_2 = 1$ atm, and furnace cooling = 120°C/hr. The microstructure contained the expected phase assemblage for processing in  $p\text{O}_2 = 1$ atm. The majority of the core consisted of Bi-2212 grains that appear gray in Figure 2-5. Also present were small grains of  $(\text{Sr,Ca})_{14}\text{Cu}_{24}\text{O}_x$  (14:24 AEC (alkaline earth cuprate)) particles that appear black in Figure 2-5 as well as some small grains of  $\text{Bi}_2(\text{Sr,Ca})_4\text{O}_x$  (2:4 CF (Cu free)) particles that appear bright white in Figure 2-5. The thin, long, white grains of  $\text{Bi}_2\text{Sr}_2\text{CuO}_x$  (Bi-2201) visible in Figures 2-5 and 2-6 were from the liquid that transformed to Bi-2201 on cooling from 840°C to room temperature and possibly from Bi-2212 that decomposed during cooling. The same phase assemblage was seen in tapes processed at  $P_{\text{total}} = p\text{O}_2 = 1$ atm and furnace cooling = 120°C/hr, but there was a large amount of Bi-2201 in this tape (Figure 2-6). The SEM pictures in

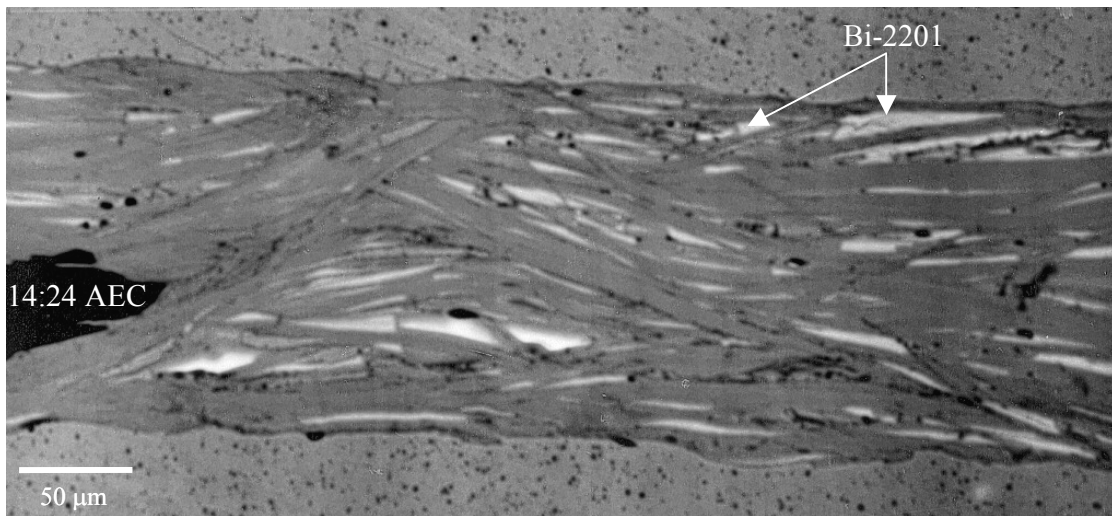


Figure 2-6. Backscattered electron image of overpressure-processed tape with furnace cooling =120°C/hr,  $P_{\text{total}}=1 \text{ atm}$ ,  $p\text{O}_2=1 \text{ atm}$ . The non-superconducting phase particles include 14:24 AEC and Bi-2201.

Figures 2-5 and 2-6 show that overpressure processing did not affect the type of non-superconducting second phase particles present in the core of Bi-2212 tapes.

## Conclusions

Overpressure processing, defined as the application of inert gas pressure in addition to the equilibrated  $p\text{O}_2$ , was developed to counteract bubbling of the silver sheath while processing meter-long lengths of Bi-2212 tape. Regardless of the initial carbon content of the Bi-2212 powder (220 or 710 ppmwt), overpressure processing was successful in eliminating the bubbling of the silver sheath at total pressures of 8-9atm and fixed  $p\text{O}_2=1 \text{ atm}$ . The types of second phase particles in the overpressure-processed tapes were unchanged compared to conventionally processed tapes. Also,  $J_c$  increased with increasing  $P_{\text{total}}$ . The results suggest that overpressure

processing may decrease porosity in the core and encourage grain alignment resulting in higher  $J_c$ . However, one drawback to overpressure processing was the slow final cooling rate due to the large thermal mass of the overpressure furnace. The slow final cooling rate may cause the Bi-2212 to decompose, thus degrading the current paths and decreasing the  $J_c$ . Either incorporating fast cooling or otherwise modifying the slow cooling process may result in even higher  $J_c$  of overpressure-processed Bi-2212 tapes.

## **2-2. Overpressure Processing of Ag-Sheathed Bi-2212 Multifilamentary Tapes**

### **Introduction**

The next overpressure experiments were conducted on multifilamentary tapes. While short lengths (centimeters) had maximum  $J_c > 10^5 \text{ A/cm}^2$ , this value was difficult to achieve in long lengths (meters) due to bubbling and porosity arising from gases formed in the initial stages of the heat treatment and the initial packing density of the Bi-2212 powder in the silver tube.

As was the case with monocoil tapes, one source of porosity in multifilamentary tapes was gases that evolve during heating to cause bubbling of the silver sheath and porosity in the core. Fourier Transform Infrared (FTIR) spectroscopy was used to measure the absorption of infrared radiation by the gases that evolved during heating the tapes from room temperature to 900°C, which was the temperature range where bubbling of the silver sheath occurred. Molecules in the evolved gases selectively absorb radiation at frequencies that match the characteristic vibrations of their individual chemical bonds. Thus, unique “molecular fingerprints” were present in FTIR spectra that can be used to determine what gases evolved upon heating.

Another source of porosity was the low initial packing density. Studies done on the powder density during the OPIT process showed that core density reached a maximum of 75% of the theoretical density and leveled off with increasing deformation [11]. That leaves 25% porosity in the green (unprocessed) wire or tape that can contain trapped gases. During heat

treatment, the silver can creep [12], which allows the silver sheath to collapse if it is thin enough. Applying an overpressure during processing may help the silver sheath collapse and densify the core. In one experiment the total pressure was varied from 1 atm to 5 atm to see how multifilamentary and monocoil samples with different geometries (round wires and rectangular tapes) were affected. In a second experiment, a tape-thickness dependence of the critical current density was found for multifilaments that were overpressure processed at 5 atm total pressure. Comparison of  $J_c$  results with microstructural observations in a SEM offer insight into the origin of the dependence of  $J_c$  on sample thickness.

## **Experimental Procedures**

Multifilamentary Bi-2212 tape from Cryoelectra GmbH was prepared using the OPIT process. The 15-filament tapes were cold rolled from an initial thickness of 1420  $\mu\text{m}$  to a final thickness of 160, 260, 330 and 760  $\mu\text{m}$ . Also included in the study were 165  $\mu\text{m}$  thick monocoil tape and multifilamentary wire from IGC (810  $\mu\text{m}$  in diameter, 290 filaments).

Short samples were pre-annealed at 700°C for 24 hrs in vacuum and then at 835°C in 1 atm  $\text{O}_2$  for 48 hours as shown in Figure 2-7a. This pre-processing step will be referred to as “VA+835.” Some samples were incompletely melt-processed as shown in Figure 2-7b after VA+835 in order to study how conductor geometry, total pressure, and preannealing affected porosity. The thickness or diameter of the green and VA+835 tapes and wires was measured before and after this heat-treatment. The change in thickness or diameter was an indirect measure

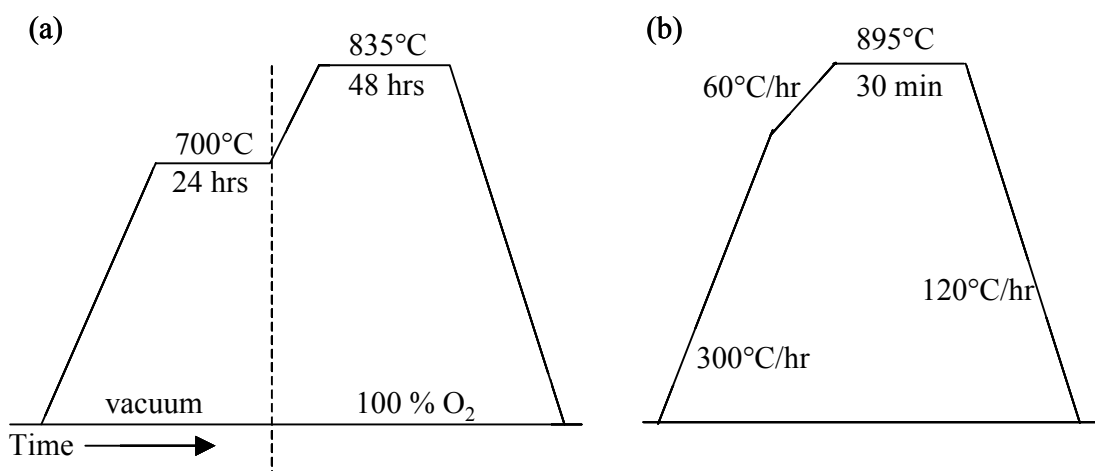


Figure 2-7. Vacuum anneal and anneal at 835°C (a) and heat treatment of samples in overpressure furnace (b).

of the porosity in the superconductor – becoming thinner corresponds to becoming denser and less porous.

Other samples were completely melt processed (see Figure 2-1) in air in the overpressure furnace with  $P_{\text{total}}=5$  atm,  $p_{\text{O}_2} = 1$  atm. The transport  $J_c$  of the fully processed samples was measured at 4.2K in self-field using the  $1 \mu\text{V}/\text{cm}$  criterion. Longitudinal cross-sections were mounted in epoxy and polished for imaging. The LEO 982 scanning electron microscope and a light microscope were used to investigate sausaging, porosity, and second-phase particle content in overpressure-processed multifilamentary tape of different thickness.

## Results and Discussion

Fourier Transform Infrared (FTIR) spectroscopy was used to determine what gases evolved during heating and were responsible for bubbling and porosity. FTIR was also used to

determine if the VA+835 pre-annealing steps reduced the amount of porosity-causing gases. One meter of green Bi-2212 tape was cut into small (1-2 cm) long pieces and placed in the FTIR crucible. The samples were heated in air at 5°C/min from room temperature to 900°C. FTIR spectra were collected at regular time intervals (3-4 per minute) during heating. Figure 2-8 includes plots showing the amount of water and CO<sub>2</sub>, which was proportional to the absorbance plotted on the y-axis, that evolved upon heating green tape. FTIR showed water evolution from room temperature to 500°C and CO<sub>2</sub> evolution beginning at about 250°C.

Another meter of Bi-2212 tape was processed using the VA+835 heat treatment. FTIR spectra were again collected upon heating from room temperature to 900°C in air. Figure 2-8 shows the amount of water and CO<sub>2</sub> that evolved after the tapes were subjected to VA+835. Almost no water was detected, within the FTIR detection limits of 0.1-1 wt%. VA+835 greatly reduced the amount of CO<sub>2</sub> over most of the temperature range. FTIR showed a smaller amount

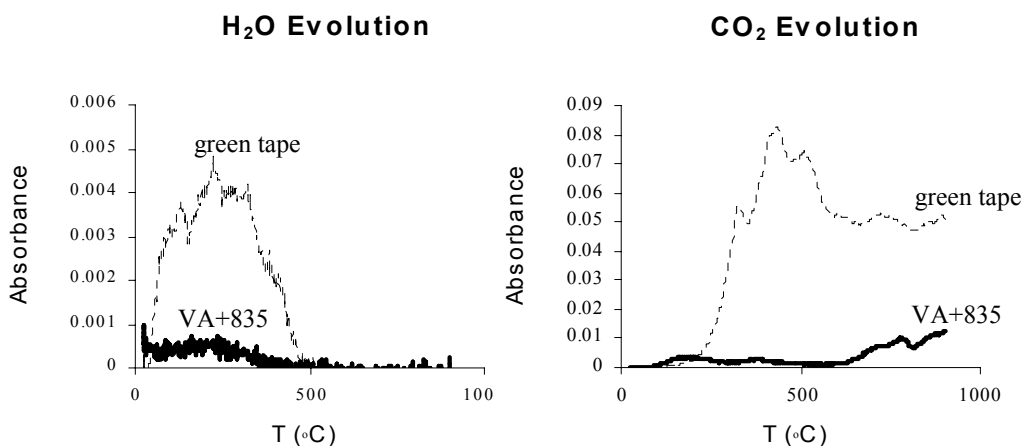


Figure 2-8. Fourier Transform Infrared spectroscopy results showing the amount of water (left) and CO<sub>2</sub> (right) evolving from either green (unprocessed) samples or samples pre-annealed with the VA+835 step.

of CO<sub>2</sub> evolving above 750°C. Therefore, FTIR showed that the VA+835 pre-annealing process eliminated H<sub>2</sub>O and reduced CO<sub>2</sub> that evolved during heating.

Thickness or diameter was measured on samples before and after all stages of the heat treatment shown in Figure 2-7b. The percent change in thickness was calculated by subtracting the initial thickness from the final thickness and dividing by the initial thickness. Table I lists the percent change in thickness for samples of different geometry incompletely melt processed at either 1 atm or 5 atm total pressure. One half of the samples were not subjected to a VA+835 preprocessing step. Of these, both the monocoreshape tape and the thin multifilament tape bubbled when processed at 1 atm, while the thick tape and round wire did not bubble. Even without VA+835, applying an overpressure stopped the Ag-sheath from bubbling and reduced the thickness of the monocoreshape tape and thin multifilament tape. Although overpressure did not collapse the thick multifilament or the round wire, the swelling was comparable in the thick multifilament at P<sub>total</sub> = 1 or 5 atm, and the swelling was reduced in the round wire for P<sub>total</sub> = 5 atm compared to P<sub>total</sub> = 1 atm.

TABLE I

Effect of increasing pressure on thickness of samples with different geometries with and without VA+835 and pO<sub>2</sub>=1atm. Positive numbers mean the tape thickness or wire diameter increased after processing; negative numbers mean the thickness/diameter decreased after processing.

Sample	t <sub>0</sub> (μm)	Without VA+835		With VA+835	
		P <sub>total</sub>		P <sub>total</sub>	
		1 atm	5 atm	1 atm	5 atm
Monocoreshape tape	165	109%	-3.0%	-3.0%	-4.8%
Thin multifilamentary tape	160	281%	-3.6%	-4.2%	0.3%
Thick multifilamentary tape	760	0.4%	0.9%	0%	-0.8%
Round multifilamentary wire	810	2.4%	0.9%	0.2%	-0.4%

Table I also shows the effect of increasing pressure on thickness when the samples were subjected to a VA+835 preprocessing step before the heat treatment shown in Figure 2-7b. With VA+835, none of the samples bubbled when processed at 1 atm. The decrease in thickness of the monocoire tape, thick multifilament tapes, and round multifilament wires was larger at 5 atm than at 1 atm. This trend was also expected for the thin multifilament tape, so the 5 atm data point seems suspect.

Light microscope images of transverse cross-sections of samples after heat treatment (Figure 2-7b) at 1 atm both with and without a VA+835 step are shown in Figure 2-9. The severe deformation in the monocoire and thin multifilament tapes was a result of gas evolution during

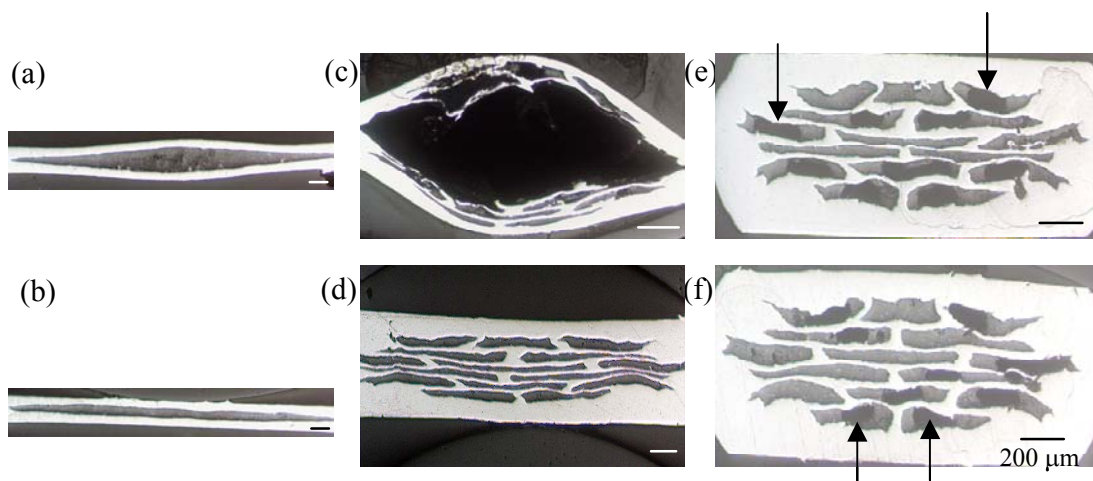


Figure 2-9. Light micrographs of transverse cross-sections of monocoire tape (a, b), thin multifilament (c, d), and thick multifilament (e, f) showing bubbling and porosity. The top row (a, c, e) shows samples that were not pretreated with the VA+835 step before processing at 1 atm. The samples in the bottom row (b, d, f) were preannealed with the VA+ 835 step before processing at 1 atm. Some pores are indicated with arrows.

heating. Figure 2-9e, f also shows a large amount of porosity in the core of the thick multifilament tape due to either the initial packing porosity or gas evolution. Samples with thin silver walls (Figure 2-9a, c) that were not preprocessed with the VA+835 step could not withstand the pressure due to evolving gases. Removing water and CO<sub>2</sub> during the VA+835 step prevented the Ag-sheath from bubbling (Figure 2-9b, d) when processed at 1atm. The thick multifilamentary tape (Figure 2-9e) had thick enough silver to withstand the evolving gas pressure. However, even though water and CO<sub>2</sub> were removed by VA+835, porosity remained in the core of the thick multifilament (Figure 2-9f) because the silver walls could not collapse under the external pressure of only 1 atm.

Figure 2-10 shows the engineering critical current ( $j_e$ ) as a function of tape thickness of fully processed (Figure 2-1) multifilaments with  $P_{\text{total}} = 5\text{atm}$  and  $p\text{O}_2 = 1\text{atm}$ . The different data

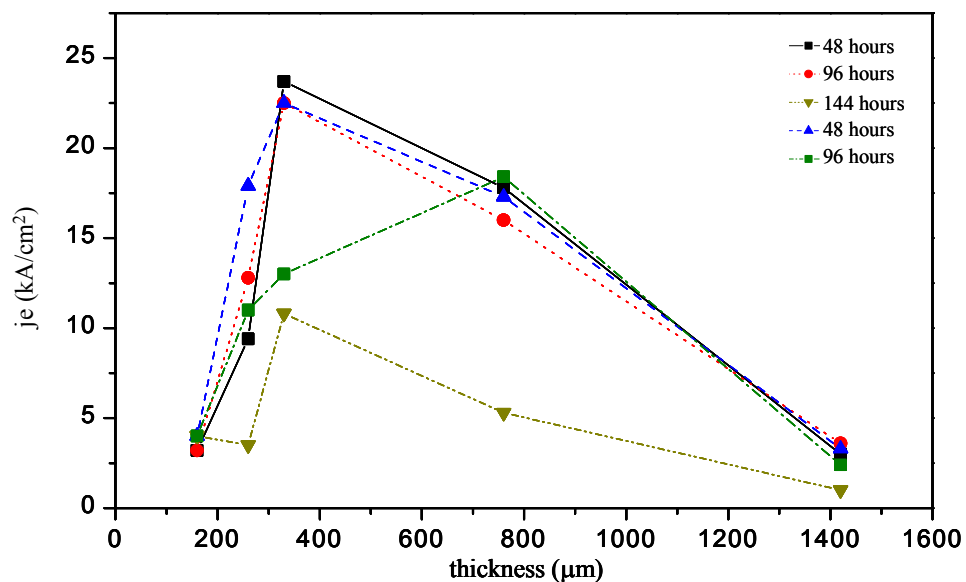


Figure 2-10. Engineering critical current density ( $j_e$ ) of overpressure-processed Bi-2212 multifilamentary tapes as a function of tape thickness for various preanneal times at 835°C.  $P_{\text{total}}=5\text{atm}$ ,  $p\text{O}_2=1\text{atm}$ .

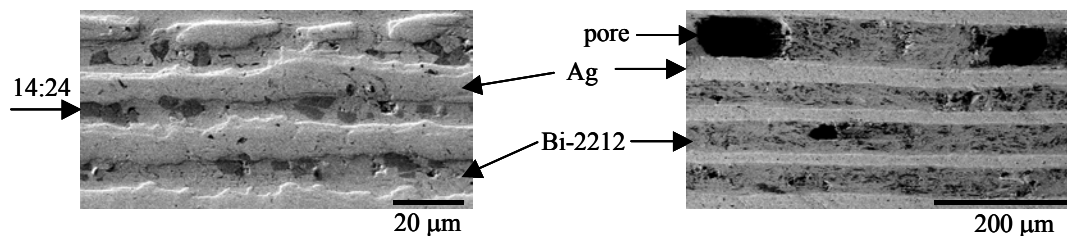


Figure 2-11. Secondary electron images of portions of the 160 mm thick sample (left) and the 760 mm thick sample (right). The magnifications were selected to show multiple filaments in each sample.

points at each thickness value represent samples with different preannealing times at  $835^{\circ}\text{C}$  – 48, 96, or 114 hours. For all of the pre-annealing treatments,  $j_c$  varied strongly with thickness, having a maximum at  $330\mu\text{m}$ .

Longitudinal cross-sections were examined in the SEM. The secondary electron micrographs of the thinnest ( $160\mu\text{m}$ ) and thickest samples ( $760\mu\text{m}$ ) are shown in Figure 2-11. Differences in sausing, porosity, and second-phase content were evident. The thinnest sample had severe sausing. In contrast, the thickest sample had smooth, uniform interfaces between the silver and superconductor. The amount of porosity was also different in these two tapes. Overpressure processing was successful in reducing porosity in the thinnest samples; very few, and relatively small, uniform pores were seen. However, substantial porosity remained in the thickest sample; large pores often spanned the entire filament thickness. Finally, the largest second-phase particles in all samples were  $(\text{Sr,Ca})_{14}\text{Cu}_{24}\text{O}_x$  (14:24 AEC). In the thinnest tape, the second-phase particles were round and  $5\text{-}10\mu\text{m}$  in size. The 14:24 AEC particles in the thickest tape were more rectangular, with the dimensions  $\approx 10\text{-}20\mu\text{m}$  long and less than  $5\mu\text{m}$  in thickness. While the absolute size of the second-phase particles in the samples was comparable, the area of the filament being blocked by second-phase particles was quite different. In numerous

places in the thinnest tape, the entire filament was blocked by 14:24 AEC. Therefore, the intermediate thickness samples probably had higher critical current because the trade-off between sausaging, porosity, and second-phase content was optimized.

The reduction of the critical current density with increasing thickness for the thicker tapes can be understood in terms of incomplete texturing and enhanced porosity due to the thickness of the superconducting core. Better texturing close to the Ag/BSCCO interface is a well-known phenomenon in both Bi-2223 [13] and Bi-2212 tapes [14]. Thus, the reduced relative contribution from Bi-2212 regions close to Ag/Bi-2212 interface might contribute to decreasing  $j_e$  with increasing tape thickness. Another reason for smaller  $j_e$  in thicker tapes was large pore size, possibly due to enhanced mechanical stability of the thicker Ag sheath, so that the overpressure used might be not high enough to cause the Ag sheath to collapse.

In contrast, the  $j_e$  reduction in the thinnest tapes may be due to the size of the second phase particles. The large 14:24 AEC particles can significantly reduce the cross-section for current flow through the thinnest filaments.

## Conclusions

The percent change in sample thickness, an indirect measurement of the change in porosity, was measured for a number of variables: with and without the VA+835 pre-processing step;  $P_{\text{total}} = 1$  or 5 atm; and sample geometry such as round wires and rectangular multifilamentary tapes with different thickness (160-760  $\mu\text{m}$ ). Light micrographs show that overpressure processing was effective at eliminating bubbling and reducing porosity in

monocore and thin multifilamentary tapes. In addition, using a combination of vacuum annealing at 700°C and holding for two days at 835°C in 100% O<sub>2</sub> was effective in reducing the amount of water and CO<sub>2</sub> in the core, which FTIR spectroscopy showed was responsible for bubbling of the silver sheath.

In overpressure-processed multifilamentary tapes, a thickness dependence of  $J_c$  was found. The maximum  $J_c$  was measured in 330 μm thick tapes; thinner and thicker tapes had reduced  $J_c$ . Compared to the optimum sample thickness of 330 μm, SEM images showed that the thicker tapes were more porous, whereas thinner tapes contained a greater amount of second phases. In these non-optimized cases, the current path can be blocked by either large pores or large non-superconducting particles of Sr<sub>14</sub>(Ca,Cu)<sub>24</sub>O<sub>x</sub>. Thus, the observed thickness dependence of  $J_c$  was interpreted as the result of competition between porosity that can decrease  $J_c$  in the thickest samples and second phase particles that can decrease  $J_c$  in the thinnest samples.

### **2-3. PAIR Processing of Ag-sheathed Bi-2212 Monocore Tapes**

#### **Introduction**

Several microstructural defects can reduce  $J_c$  in Bi-2212 tapes. As discussed earlier, porosity from low packing density and gas evolution during heat treatment can disturb the alignment of superconducting grains in the core. The presence of non-superconducting second phase particles reduces the cross-section available for supercurrent flow as well as disturbing the superconductor grain alignment (see Figure 2-12). As described in earlier sections, common second phase particles in Bi-2212 tapes were  $(\text{Sr,Ca})_{14}\text{Cu}_{24}\text{O}_x$  (14:24 AEC) and  $\text{Bi}_2\text{Sr}_2\text{CuO}_x$  (Bi-2201). The grain alignment near the superconductor-silver sheath interface is especially critical, as studies have shown that the majority of supercurrent flow is near the interface [15].

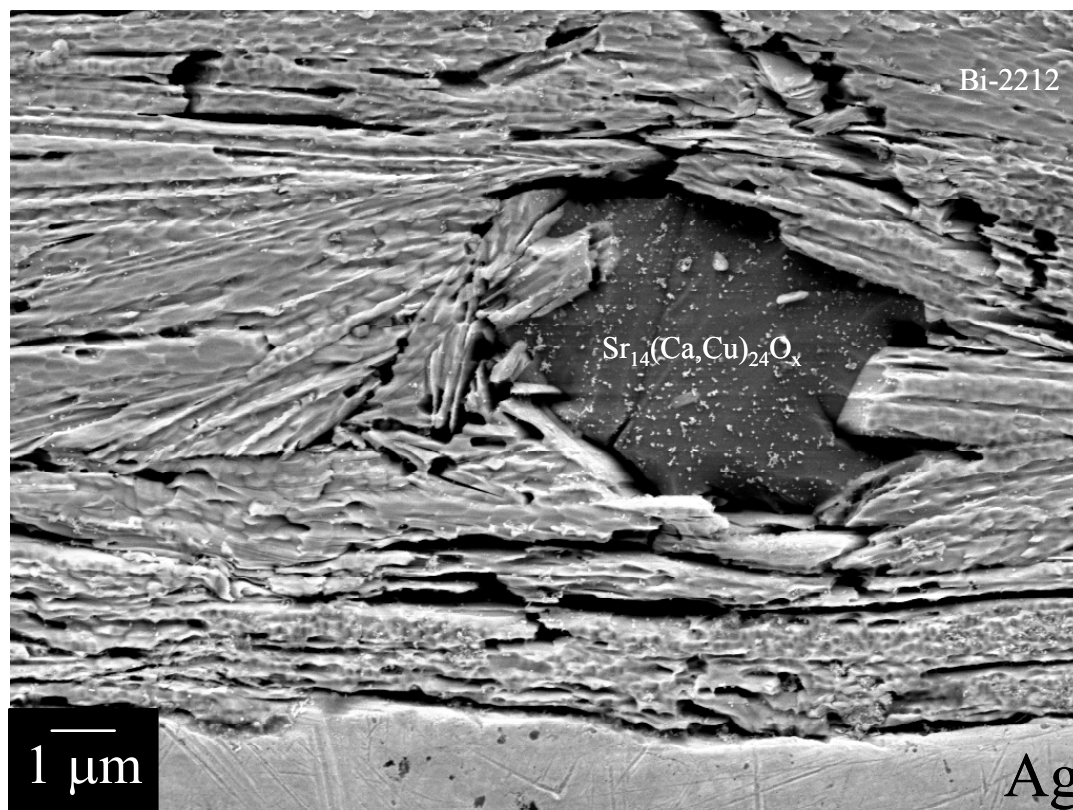


Figure 2-12. SEM image of a longitudinal cross-section of Bi-2212 tape showing grain misalignment in the vicinity of a non-superconducting second phase particle of  $\text{Sr}_{14}(\text{Ca,Cu})_{24}\text{O}_x$ .

Recently a new Bi-2212 conductor fabrication method, called the Pre-Anneal and Intermediate Rolling (PAIR) process, has been introduced that may increase superconductor grain alignment while reducing porosity and non-superconducting second phase particle content. With this fabrication method, record-setting critical current densities  $>500,000 \text{ A/cm}^2$  (4.2K, 10T) have been produced in Ag-wrapped, dip-coated, multilayer Bi-2212 conductors [16-19].

In the PAIR process, the first step was pre-annealing. It consisted of heating the green (unprocessed) Bi-2212 tapes in a furnace at a temperature below the melting point of Bi-2212 ( $T < 880^\circ\text{C}$ ) but high enough for water and  $\text{CO}_2$  to evolve ( $T > 800^\circ\text{C}$ ). The pre-annealing time

must also be long enough for the evolved gases to diffuse through the silver sheath. Powder sintering and densification can occur during pre-annealing. For dip-coated tapes, the organic binder was also burned out during pre-annealing, leaving many large pores in the Bi-2212 layer.

After pre-annealing, the next step in the PAIR process was intermediate rolling at room temperature. The amount of cold rolling was measured by the percentage reduction in thickness of the Bi-2212 tape and was varied from 0-35% in the initial PAIR experiments on dip-coated Bi-2212 tape [17]. While a small percent reduction may be beneficial, larger percent reductions may cause sausaging – undulation of the interface between the superconductor and silver.

In this study, the PAIR process was applied to monocoil Bi-2212 tapes before standard heat treatments to study the effect of pre-anneal time, pre-anneal temperature, and percent rolling reduction on superconductor grain alignment, porosity, and second phase particle content.

## **Experimental Procedures**

This experiment utilized six sets (Table II) of monocoil silver-sheathed Bi-2212 monocoil tapes with composition 2.29:2:1:2.016. Each of the four samples within a given set had the same pre-anneal time and pre-anneal temperature but different rolling reductions.

TABLE II  
Experimental variables of PAIR processed tapes.

<b>Pre-Anneal Temperature</b>	<b>Pre-Anneal Time</b>	<b>% Intermediate Rolling</b>
835°C	6 hours	0, 10, 19, 35
835°C	24 hours	0,14, 17, 28
835°C	48 hours	0, 8, 23, 31
850°C	6 hours	0, 9, 20, 30
850°C	24 hours	0, 12, 17, 27
850°C	48 hours	0, 13, 17, 30

The Bi-2212 tapes underwent a two-step pre-anneal. The samples were layered in a ceramic crucible with calcium zirconium powder to prevent the samples from bonding to each other during preannealing. As shown in Figure 2-13, the first pre-anneal was in vacuum at 700°C for 24 hours followed by a second pre-anneal at elevated temperature (835°C or 850°C) for varying lengths of time (6-48 hours). As discussed in section 3-2, during the first pre-anneal step, water was removed from the core; during the second step, carbon dioxide was removed.

Intermediate rolling of samples with 150  $\mu\text{m}$  initial thickness resulted in percent reductions of approximately 0%, 10%, 20% and 30%. Due to mechanical fluctuations during rolling, there were 1-5% variations in percent reductions. The actual percent reduction for each set of pre-anneal temperatures and times are shown in Table II.

After pre-annealing and intermediate rolling, the samples were melt-processed. The ends of the tape were mechanically sealed by wrapping with silver foil and then crimping in order to prevent leakage during heat treatment. As shown in Figure 2-14, the samples were melt-processed as follows: heat to 835°C, hold for 1 hour, heat to 895°C, hold for 30 minutes, cool to

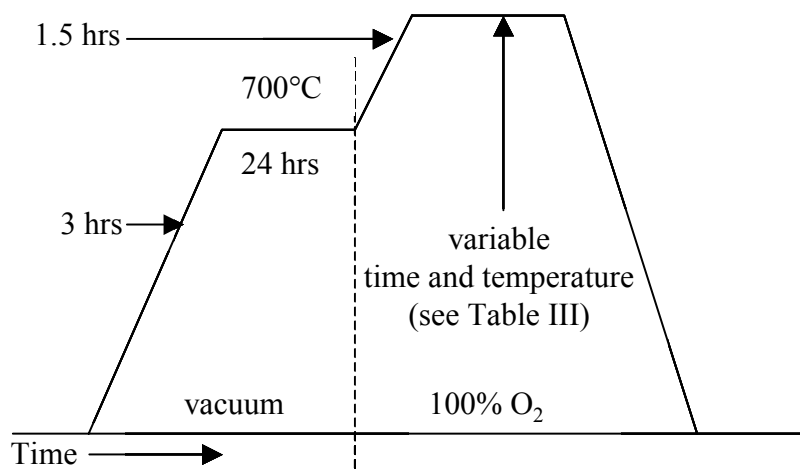


Figure 2-13. Preannealing times and temperatures for PAIR samples.

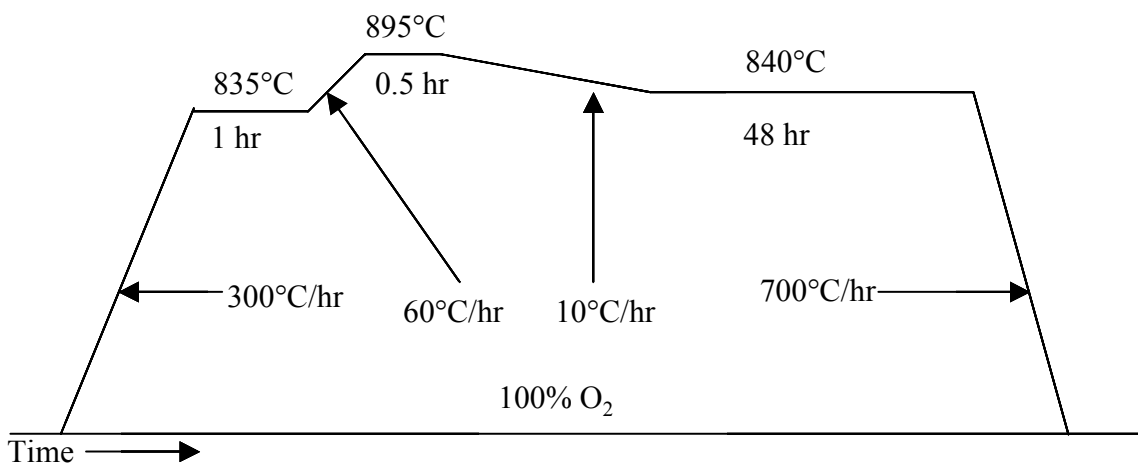


Figure 2-14. Melt processing of PAIR samples.

840°C at 10°C/hr, hold for 48 hours, and cool rapidly to room temperature at 700°C/hr. All melt processing was done in 100% O<sub>2</sub> in order to optimize the second phase particle content.

After the samples were melt-processed, longitudinal and transverse cross-sections of each sample were mounted and polished for microstructural analysis in the SEM. The change in second phase content, porosity, and grain alignment of PAIR processed tapes were studied using

SEM, EDS, and x-ray diffraction. Adobe Photoshop™ image processing software was used to calculate the area fraction of second phase particles and porosity from at least five representative cross-sectional images of each sample.

## Results and Discussion

Second phase particle content and distribution as a function of percent reduction was first investigated. The samples that were rolled to nominally 20–30% reduction contained fewer second phase particles than the samples with 0–10% reductions. As shown in Figure 2-15, the 0% and 10% samples contained more 14:24 AEC particles than the 20% and 30% samples. In addition, the 20% and 30% samples had more Bi-2201 phase dispersed throughout than the 0%

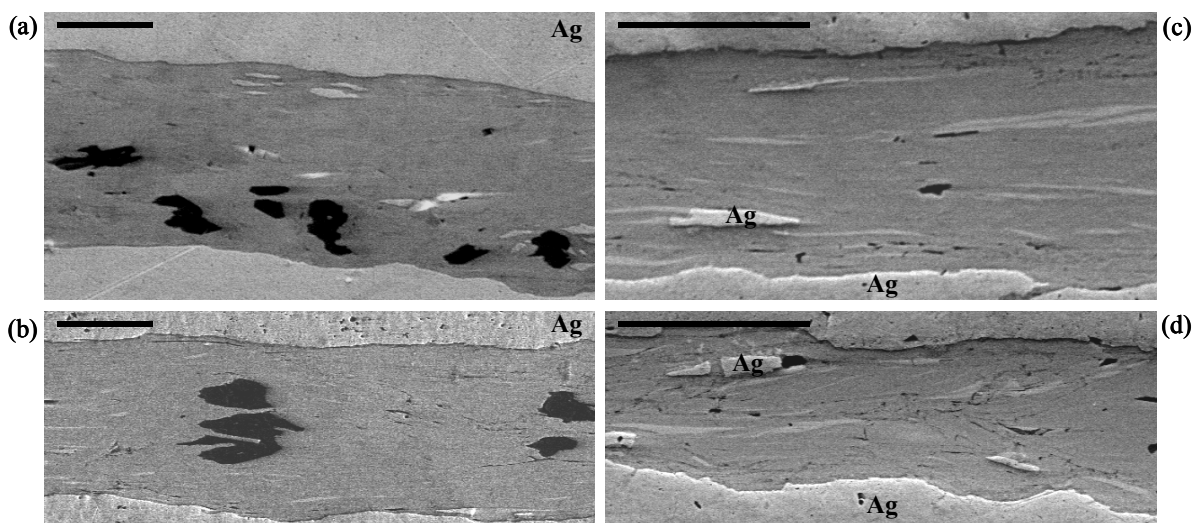


Figure 2-15. SEM micrographs of PAIR processed samples with different percent reductions: (a) through (d) are 0, 10, 20, 30% reduction, respectively. The black phase is 14:24AEC, the bright white phase is Cu-free, and the light gray phase is Bi-2201. The length marker is 20 $\mu$ m.

and 10% samples. This is significant because Bi-2201 is superconducting at low temperatures, whereas the 14:24 AEC phase is not. The Bi-2201 phase was also generally long and thin, whereas the 14:24 AEC particles were large, blocky grains 10-20  $\mu\text{m}$  in size. The SEM images suggest that the narrow Bi-2201 phase did not disturb grain alignment as much as the blocky 14:24 AEC particles. The different pre-anneal times and temperature did not appear to affect the phase assemblage of these samples in any significant way.

Porosity in the fully processed tapes was also examined. It did not appear that there was a direct correlation between porosity and either percent reduction or pre-anneal temperature. However, one may form an indirect correlation between porosity and percent reduction. 14:24 AEC particles tend to grow around pores formed early in the melt processing. Since the amount of 14:24 AEC decreased when a higher percent reduction was used, porosity may also decrease with increasing percent reduction.

The x-ray diffraction results (Figure 2-16) showed that texture decreased in the tapes with increasing percent reduction beyond 15-20%. SEM images showed severe sausaging at the maximum percent reduction. The lowest FWHM (full width, half maximum) value of approximately  $7^\circ$  was at a rolling reduction of 10-15%.

All of the results suggest a trade-off between optimizing the second phase particle distribution and grain alignment near the superconductor/silver interface. Since sausaging disrupted grain alignment along the interface, rolling to more than 20% reduction should be avoided. However, a more favorable phase assemblage appeared at 20% and 30% reductions, and there may be less porosity in these samples. Thus, the optimal reduction for maximum  $J_c$  likely falls in the 15%-25% rolling reduction range.

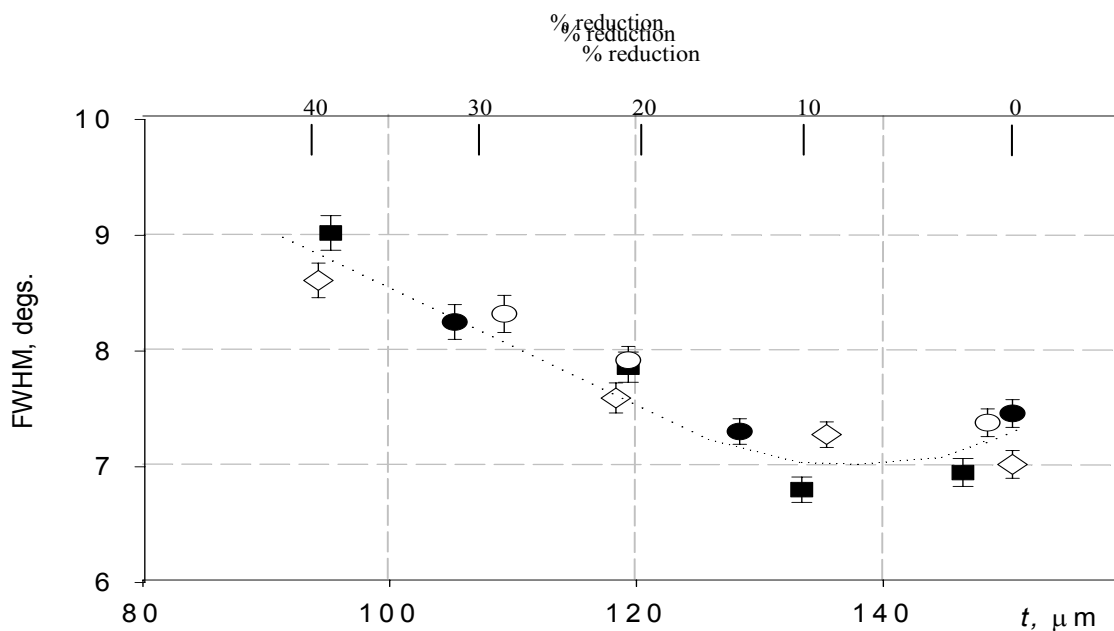


Figure 2-16. FWHM of the 00-20 peak as a function of the sample thickness of PAIR-processed monocoil tapes. Courtesy of Mark Rikel.  
 Figure 2-16. FWHM of the 00-20 peak as a function of the sample thickness of PAIR-processed monocoil tapes. Courtesy of Mark Rikel.

## Conclusions

The effects of the PAIR process, consisting of pre-annealing steps followed by cold rolling, were investigated in Bi-2212 tapes. Cross-sectional SEM images showed that increasing the percent rolling reduction decreased the area fraction of 14:24AEC and Cu-free non-superconducting particles while increasing the area fraction of the Bi-2201 phase. However, grain alignment was adversely affected by sausaging in tapes with the highest percent reduction. X-ray diffraction results confirmed the worsening texture above 20% rolling reduction. The PAIR process may have increased  $J_c$  by optimizing grain alignment at the superconductor/Ag interface and reducing the occurrence of porosity and second phases.

## **2-4. Summary**

Microstructural defects in melt-processed Bi-2212 tapes and multifilaments included bubbling, porosity, and second phase particles. Overpressure processing, defined as the application of inert gas pressure in addition to the equilibrated  $pO_2$ , was developed to eliminate bubbling of the silver sheath while processing meter-long lengths of Bi-2212 tape. In overpressure-processed monocoil tapes,  $J_c$  increased with increasing total pressure.

In overpressure-processed multifilamentary tapes, a thickness dependence of  $J_c$  was found. Compared to the optimum sample thickness of 300  $\mu\text{m}$ , SEM images showed that the thicker multifilamentary tapes were more porous, whereas thinner multifilamentary tapes contained a greater amount of second phases. In these non-optimized cases, the current path can be blocked by either large pores or non-superconducting particles of  $\text{Sr}_{14}(\text{Ca,Cu})_{24}\text{O}_x$ . Thus, the observed thickness dependence of  $J_c$  was interpreted as the result of competition between porosity and second phase particles.

With optimized parameters, the PAIR process reduced porosity and improved Bi-2212 grain alignment in monocoil tapes. Cross-sectional SEM images showed that increasing the percent rolling reduction above 20% decreased the area fraction of non-superconducting particles. However, X-ray diffraction showed worsening texture above 20% rolling reduction. The PAIR results suggested that optimizing  $J_c$  involves a trade-off between minimizing the second phase particle content and maximizing the grain alignment near the superconductor/silver interface.

## 2-5. References

- [1] J.L. Reeves, M. Polak, W. Zhang, E.E. Hellstrom, S.E. Babcock, D.C. Larbalestier, N. Inoue, and M. Okada, *IEEE Trans. Appl. Super.* **7** (1997) 1541-43.
- [2] J.L. Reeves, E.E. Hellstrom, V. Irizarry, and B. Lehndorff, *IEEE Trans. Appl. Super.* **9** (1999) 1836-39.
- [3] B. Lehndorff, J.L. Reeves, A. Polyanskii, M.O. Rikel, E.E. Hellstrom, and D.C. Larbalestier, *Proceedings EUCAS* (Barcelona, Spain: 4<sup>th</sup> European Conference on Applied Superconductivity, 1999).
- [4] J. Reeves, D. Adolphs, A. Arndt, D. Zwicky, M. Rikel, and E. Hellstrom, *Physica C* **341-348** (2000) 2021-2.
- [5] E. Hellstrom and W. Zhang, *Supercond. Sci. Technol.* **8** (1995) 317-23.
- [6] A. Endo and S. Nishikida, *IEEE Trans. Appl. Supercond.* **3** (1993) 931-934.
- [7] T. Kanai, N. Inoue, and T. Kamo, *J. Mater. Res.* **9** (1994) 1363-8.
- [8] W. Zhang and E.E. Hellstrom, *Supercond. Sci. Technol.* **8** (1995) 430-8.
- [9] T. Kanai and N. Inoue, *J. Mat Sci.* **30** (1995) 3200-3206.
- [10] W. Zhang and E. Hellstrom *Physica C* **234** (1994) 137-145.
- [11] M. Karuna, J. A. Parrell and D. C. Larbalestier, *IEEE Trans. on Appl. Supercond.* **5** (1995) 1279-82.
- [12] K. C. Goretta, W. E. Delaney, J. L. Routbort, J. Wolfenstine, W. Zhang and E. E. Hellstrom, *Supercond. Sci. and Tech.* **9** (1996) 422-6.

- [13] C. Zhang, Y. Z. Wang, D. C. Zeng, Z. Q. Yang, Z. R. Li, G. W. Qiao, J. R. Fang, and Y. C. Chuang, *J. Appl. Physics* **79** (1996) 8112-4.
- [14] H. Kitaguchi, H. Miao, H. Kumakura, K. Togano and B. Chenevier, *Physica C* **301** (1998) 111-5.
- [15] T. Muroga, J. Sato, H. Kitaguchi, H. Kumakura, K. Togano and M. Okada, *Physica C* **309** (1998) 236-44.
- [16] H. Miao, H. Kitaguchi, H. Kumakura, K. Togano, T. Hasegawa and T. Koizuma, *Physica C* **303** (1998) 81-90.
- [17] H. Miao, H. Kitaguchi, H. Kumakura, K. Togano and T. Hasegawa, *Physica C* **301** (1998) 116-22.
- [18] Y. Hishinuma, H. Kitaguchi, H. Miao, H. Kumakura, K. Itoh and K. Togano, *Supercond. Sci. & Tech.* **11** (1998) 1237-40.
- [19] H. Miao, H. Kitaguchi, H. Kumakura and K. Togana, *Cryogenics* **38** (1998) 257-9.

### 3. YBCO Analysis Techniques

This section describes the three main experimental techniques that were used to characterize the YBCO coated conductors: Backscattered Electron Kikuchi Pattern (BEKP) analysis of local grain orientation and calculation of grain boundary misorientation, Magneto-optical (MO) imaging to locate barriers to current flow, and Focused Ion Beam (FIB) cutting.

#### ***3-1. Backscattered Electron Kikuchi Pattern Analysis to Determine Crystal Orientation***

BEKP is an electron diffraction technique that can be implemented in an SEM to obtain electron diffraction patterns from the near surface region of bulk samples. BEKP analysis provides a point-by-point measure of crystallographic orientation. In a typical experiment, SEM images reveal the sample's microstructure — grain size, morphology and spatial distribution. BEKP analysis measures the **local** orientation of the microstructural features of interest. BEKP provides complementary information to x-ray diffraction, which measures texture on a more global scale without any positional information. BEKP can map grain orientations and calculate misorientations on the sub-micron to millimeter scale. A disadvantage of BEKP is that the depth resolution is only on the order of 10-50 nm, which means that this technique is very sensitive to surface damage. It also becomes difficult to obtain BEKP patterns from rough surfaces because the sample surface normal is tilted at approximately  $70^\circ$  with respect to the electron beam.

Surface roughness is usually not a problem with polished metal samples; however, as-grown superconducting films can be very rough and therefore difficult to obtain high quality Kikuchi patterns from.

The next paragraphs describe the basics of Kikuchi pattern formation and how local grain orientation is measured [1-10], followed by a discussion of how BEKP was used in this work.

Kikuchi patterns have traditionally been used to measure the misorientation between nanosized grains in transmission electron microscopy (TEM). In 1973, researchers [4] showed how backscattered electrons could theoretically produce Kikuchi patterns in the SEM. Advantages of Kikuchi pattern analysis in the SEM instead of the TEM include easier sample preparation and the ability to investigate grain orientations and misorientations on the micron to millimeter length scale. Eleven years later, other researchers [3] detected these backscattered electron Kikuchi patterns using a video camera inside an SEM and were also the first to use a computer to index the Kikuchi patterns. Although an experienced operator could index approximately 120 Kikuchi patterns in an hour, thousands of patterns need to be collected and analyzed to determine the orientation of micron-sized grains. BEKP analysis in the SEM utilizes a computer to control both the SEM stage and the camera so that Kikuchi patterns could be quickly collected and rapidly indexed (1800 patterns in an hour). The advances in hardware and software in the past decade have increased the speed with which the technique can be implemented and thus have led to its popularization. The following paragraphs describe how diffracted electrons produce Kikuchi patterns in the SEM and how Kikuchi patterns are analyzed.

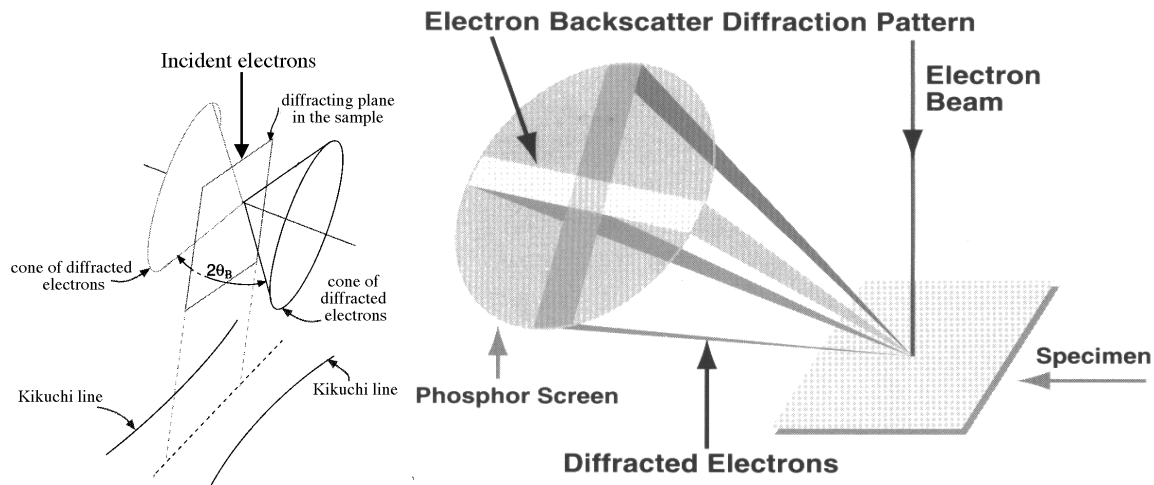


Figure 3-1. Production of BEKPs in an SEM. From [11,12].

Kikuchi patterns are formed from Bragg diffraction of monochromatic, incoherent radiation. Consider a focused 20 keV electron beam in an SEM. All the accelerated electrons have approximately the same energy, and therefore the same  $\lambda$ , so the electron beam is monochromatic. Also, an electron's path can be described by the wavevector  $\mathbf{k}$ , where the direction of  $\mathbf{k}$  represents the direction of the electron's path. Electrons in a focused beam have a wide distribution of  $\mathbf{k}$ , so the electron beam is incoherent. Therefore, the electron beam in an SEM is both monochromatic and incoherent.

When a focused beam of energetic (20keV) electrons impinges upon the sample surface, backscattered electrons are Bragg diffracted as shown in Figure 3-1 to form Kikuchi patterns. For a range of  $\mathbf{k}$ s, the diffracted paths of the backscattered electrons lie on the surfaces of cones. For one incident  $\mathbf{k}$ , one diffracted beam is produced. A phosphor screen is placed near the sample to detect the backscattered electrons that form the Kikuchi pattern. A Kikuchi line is seen

where a cone of diffracted electrons intersects the flat screen. The line's position and intensity will depend on which crystallographic planes are oriented in a favorable diffracting condition. The pair of Kikuchi lines makes up a Kikuchi band; a collection of Kikuchi bands makes up a Kikuchi pattern. Each band in the Kikuchi pattern represents a specific set of diffracting planes in the volume of the sample excited by the incident electron beam. The band's position on the screen depends on the crystallographic orientation of the diffracting planes, while the band's width is a function of the lattice plane spacing (band width =  $2\theta_B$ ). The band median corresponds to the trace of the diffracting lattice planes. The intersection of Kikuchi bands is a pole. From the distances and angles between the poles in the Kikuchi pattern, the poles are identified and indexed. The orientation of the crystal with respect to the sample coordinate system is determined from the spatial distribution of poles. To illustrate how lattice orientation can be determined from the information contained in a Kikuchi pattern, Figures 3-2a and b are two Kikuchi patterns from different grains in a metal substrate sample. The arrangement of Kikuchi bands into the star-shaped feature indicates a pole, in this case of  $\langle 110 \rangle$  type. The Kikuchi bands in the pattern are indexed (Figure 3-2c, d) and the orientation corresponding to the arrangement of Kikuchi bands is calculated. The change in position of the pole indicates a change in grain orientation between the two points where Kikuchi patterns in Figure 3-2 were acquired.

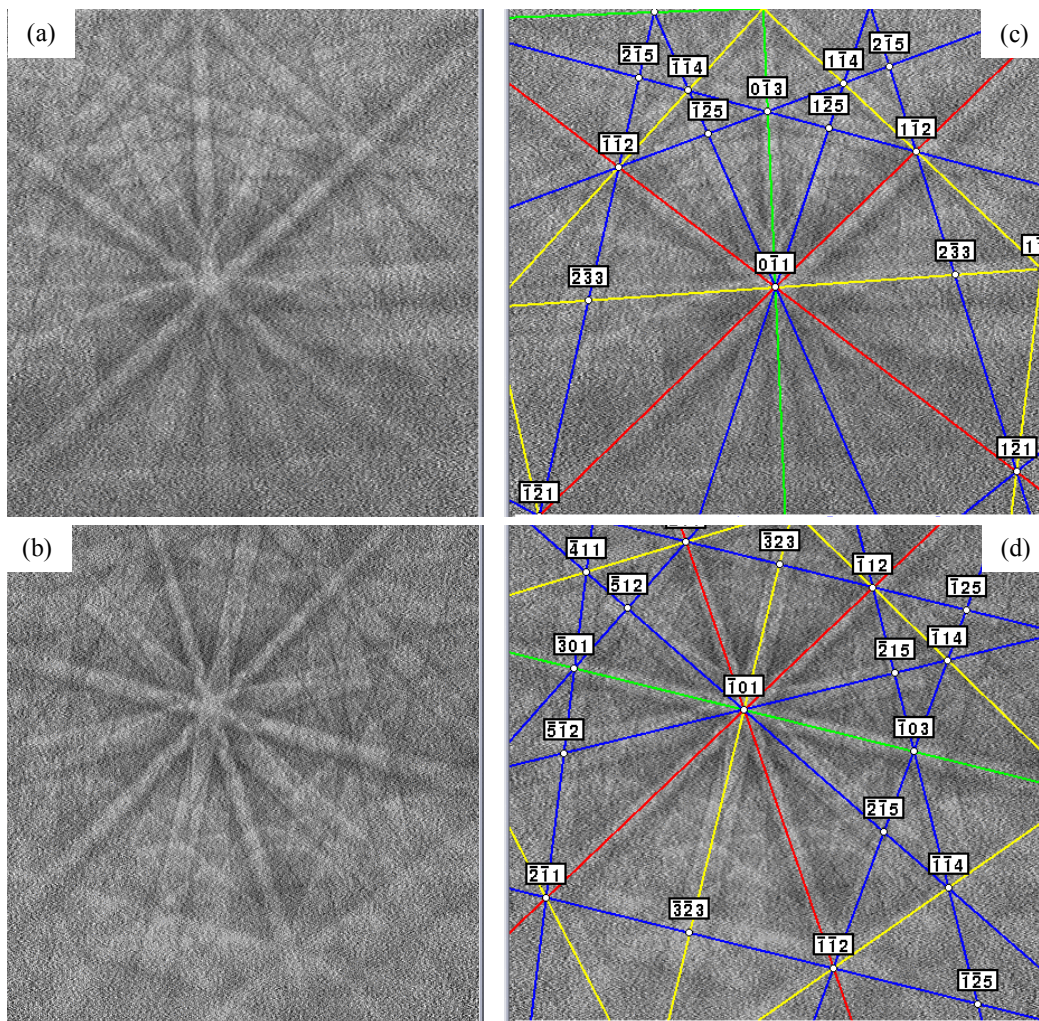


Figure 3-2. (a, b) Typical Kikuchi patterns and (c,d) indexing of Kikuchi bands from a polished metal substrate sample.

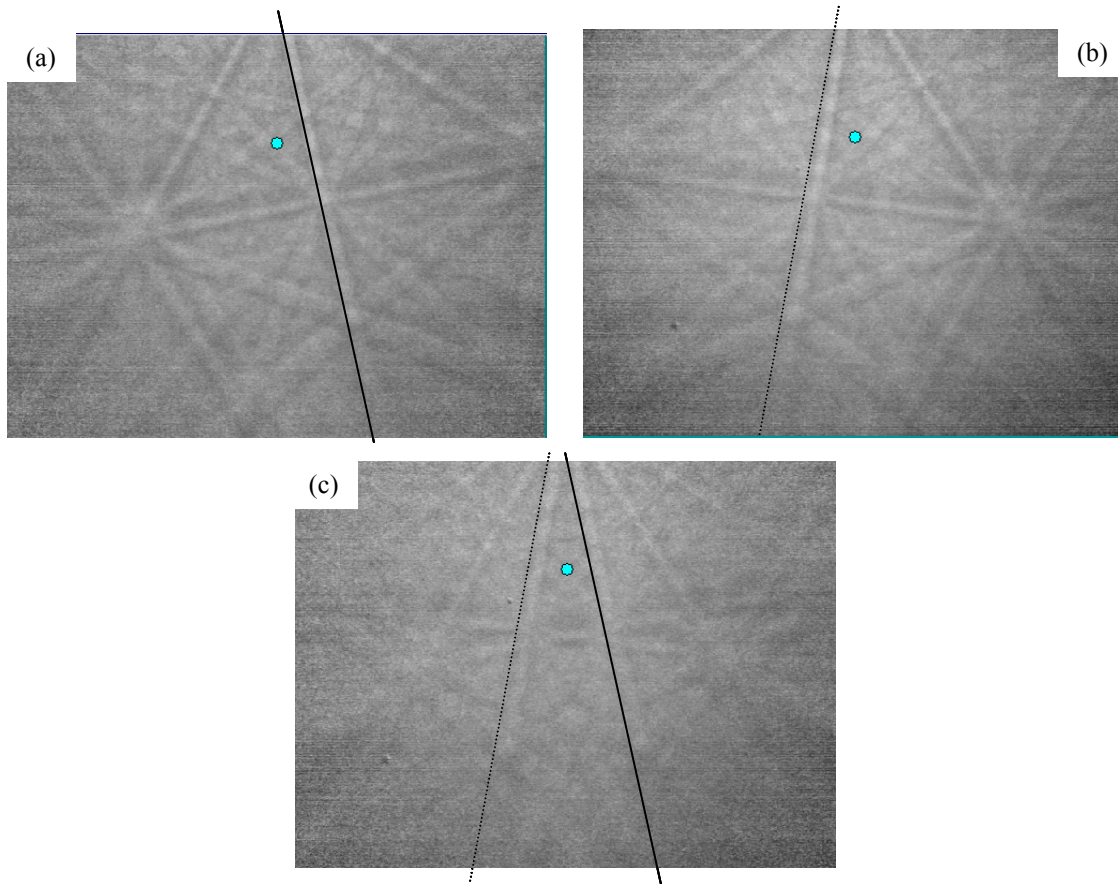


Figure 3-3. (a, b) Kikuchi patterns taken on each side of a  $24^\circ$  [001] YBCO grain boundary. (c) Kikuchi pattern taken at the grain boundary to illustrate the  $24^\circ$  rotation.

To illustrate how Kikuchi patterns change across a grain boundary, Figure 3-3a, b shows representative Kikuchi patterns from the YBCO surface on each side of a  $24^\circ$  [001] grain boundary. The Kikuchi pattern acquired at the grain boundary (Figure 3-3c) shows two overlapping patterns that are rotated approximately  $24^\circ$  with respect to one another.

With an SEM, the beam can be rastered across the sample. Computer-automated acquisition of Kikuchi patterns obtains crystallographic data on a point-by-point basis over a

selected area of the sample. Due to the accuracy of the Kikuchi band detection algorithm, grain orientations can be determined at each point with an accuracy of 0.1 - 0.5°. The practical spatial resolution of this technique ranges from 0.1 - 0.5  $\mu\text{m}$ , depending on the values of several experimental parameters such as SEM voltage, aperture size, working distance, sample composition, and beam current. For example, with typical BEKP conditions using the LEO 1530 SEM (20 kV, 120  $\mu\text{m}$  aperture, 14 mm working distance), the spatial resolution is determined by the probe diameter of 200 nm [13]. Decreasing the voltage would improve the spatial resolution by decreasing the probe diameter; however the Kikuchi pattern quality declines with decreasing voltage. Therefore, optimization of pattern quality and spatial resolution is an issue.

A BEKP scan is a collection of Kikuchi patterns obtained on a point-by-point basis from large areas, typically a few hundred microns in length and width on the sample. In this work, BEKP data were acquired using different systems: OIM<sup>TM</sup> (Orientation Imaging Microscopy) by TexSem Laboratories, ORKID (ORientation from KIkuchi Diffraction) and COM (Crystal Orientation Mapping) by Noran Instruments, and OPAL<sup>TM</sup> by Oxford Instruments. Each BEKP manufacturer has its own software that takes the data collected in a BEKP scan and produces BEKP maps to show grain orientation and misorientation. While each map is usually given a different name by the different software programs, the maps fall into 4 categories – percolation maps, grain orientation maps, grain boundary maps, and pole figures.

In a **percolation map**, a BEKP “grain” is defined by an algorithm that groups connected and similarly oriented points into a grain and then assigns that grain a color. For each point in the BEKP scan, the neighboring points are checked to see if they are within a certain tolerance angle determined by the user. If the second neighboring point is found to be within the tolerance angle of the first point, then the neighbors of the second point are checked to see if they too comply with the tolerance angle. The procedure is repeated until the set of connected and similarly oriented points are surrounded by points that exceed the tolerance angle. Figure 3-4 shows examples of percolation maps with different tolerance angles. With increasing tolerance angle, the “grain” size becomes larger while the number of “grains” becomes smaller. At some tolerance angle the percolation map can become monochromatic, indicating that the region is composed of one “grain” in which all the points have a nearest neighbor within the tolerance

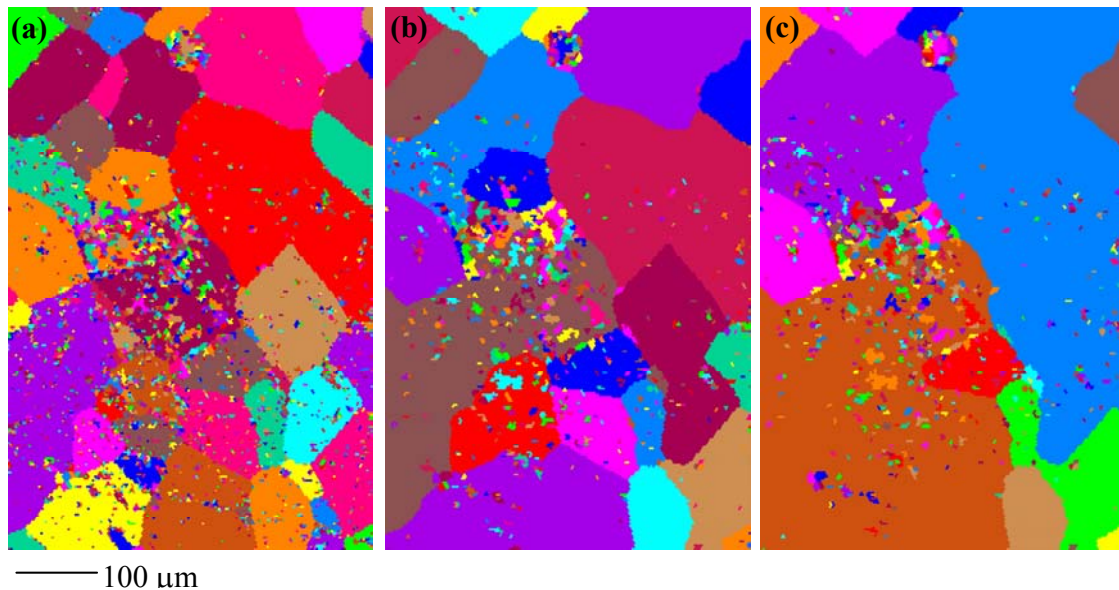


Figure 3-4. Percolation map examples for tolerance angles of (a)  $1^\circ$  (b)  $2^\circ$  and (c)  $3^\circ$ .

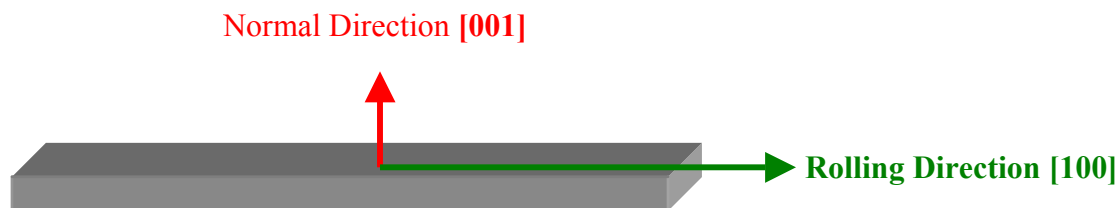


Figure 3-5. Schematic showing the BEKP frame of reference with respect to the sample geometry.

angle. In this case, the point-to-point misorientation will be quite small, but the spread of orientations can be relatively large. In effect, the algorithm used to make percolation maps is the least restrictive definition of connectivity. In the literature, monochromatic percolation maps have been made on high temperature superconductors to show the percolatively connected region for supercurrent flow [14]. A common interpretation of the monochromatic percolation maps shown in the literature is that the superconductor is single-crystalline below the tolerance angle of the percolation map. However, it is possible for a percolation map to be monochromatic, but still contain grain boundaries with larger misorientation angles than the tolerance angle of the percolation map. This will be discussed further in Chapter 4-2.

Unlike percolation maps, neighboring points in **grain orientation maps** are not compared to each other in order to be grouped into grains. Instead, grain orientation maps show color-coded grains based on how the crystallographic orientation of the points within a grain relate to the sample reference frame. For these maps, care must be taken to properly align the sample in the SEM since the orientation of each point is compared to the frame of reference illustrated in Figure 3-5. For rolled and recrystallized metal substrates, the optimum texture produced is “cube-on-cube” which means that the c-axis ( $a_3$  in a cubic structure or the [001]

direction) of each grain should be parallel to the normal direction in the sample reference frame. Similarly, the a-axis (or [100] direction) of the grains should be parallel to the rolling direction. For epitaxially grown buffer and superconducting layers, this texture should be copied from the substrate. Figure 3-6 shows a sequence of grain orientation maps that illustrate how well the c-axes of grains are aligned with respect to the sample normal direction. The c-axis alignment is also referred to as “out-of-plane” alignment. In each figure, the darkest red color corresponds to the “best” c-axis alignment while the white color corresponds to the “worst” c-axis alignment. “Best” and “worst” alignment is relative, based on the angle criterion of grain orientation map. For example, Figure 3-6a is a grain orientation map with an angle criterion of  $5^\circ$ . White areas in Figure 3-6a correspond to grains that have their c-axis misaligned by more than the angle criterion, in this case  $5^\circ$ , with respect to the sample normal direction (the [001] direction in Figure 3-5). The other areas in Figure 3-6 are shaded according to the alignment of their c-axes with the sample normal direction where the closer the alignment, the more intense the color. Figure 3-6c is an example of a grain orientation map with an angle criterion of  $15^\circ$ . In this map, white areas have c-axis alignment greater than  $15^\circ$  from the sample normal direction. These white areas correspond to contamination on the sample surface. Again, the remaining areas are shaded such that the closer the c-axis is aligned to the sample normal direction, the darker the red color will be. From the change in shading in BEKP grain orientation maps, one can calculate the fraction of grain area that is aligned to within specific angle criteria in order to quantify the texture in the sample.

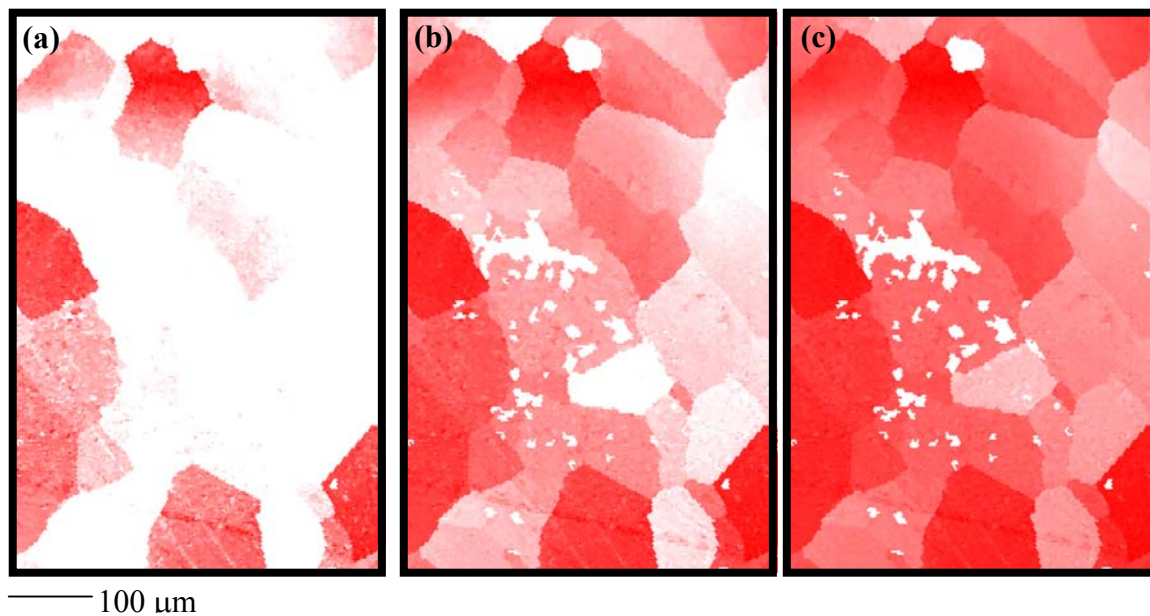


Figure 3-6. Grain orientation maps showing the alignment of the c-axis to within (a) 5°, (b) 10°, and (c) 15° of the normal direction. The darkest red color corresponds to the most well-aligned grains.

**Grain boundary maps** illustrate the misorientation between grains. There are many ways to describe the misorientation between two grains, but in this work the grain boundary misorientation will be described in terms of the angle/axis pair: the common axis shared by the two grains and the angle of rotation about that common axis that will bring them into coincidence. In highly symmetric crystal structures, there are many possible axis/angle pairs that can describe the same misorientation between two grains. For cubic symmetry, as an example, there are 24 crystallographically equivalent angle/axis pairs for a given orientation. The rotation angle shown in a grain boundary map is the minimum rotation angle among all possible angle/axis pairs. Examples of grain boundary maps are shown in Figure 3-7. A line segment separating two points in the BEKP scan is drawn and labeled with the calculated misorientation

between the two points. For example, blue line segments in Figure 3-7a are drawn if the point-to-

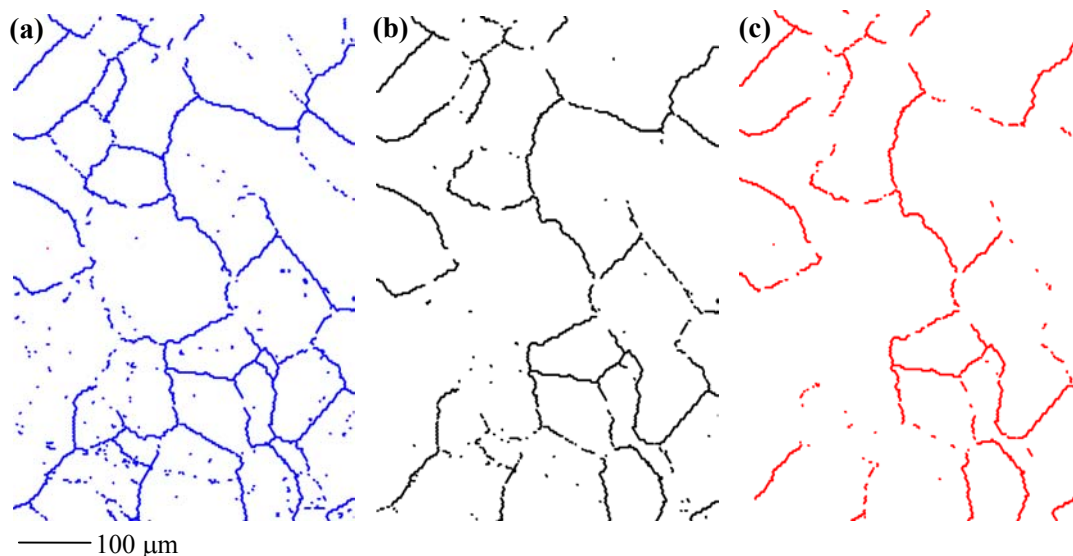


Figure 3-7. Grain boundary maps with misorientation angles greater than (a) 3°, (b) 4°, and (c) 5°.

point misorientation is greater than 3°. Most of the colored line segments in Figure 3-7 appear to delineate grain boundaries; however, some of the randomly dispersed line segments may be due to noise in the BEKP scan and not associated with actual grain boundaries in the microstructure.

Some BEKP software programs allow grain boundary maps to be combined with other kinds of maps. For example, Figure 3-8 shows grain boundaries on grain orientation maps. Like Figure 3-6, Figure 3-8a shows the alignment of the grains' c-axes with respect to the normal direction in the sample reference frame. The red shading illustrates the “out-of-plane” (c-axis) alignment. In a similar fashion, Figure 3-8b shows the “in-plane” (a-axis) alignment. The darkest green color corresponds to the a-axis being parallel to the rolling direction in the sample reference frame. The grain boundaries are colored according to the range of misorientations:

blue lines represent grain boundaries with 1-5° misorientation whereas black boundaries have 5-15° misorientation. Examining the grain orientation shading on either side of grain boundaries can yield insight into the grain boundary axis of rotation. For example, consider the circled grain boundary in Figure 3-8. The grain shading on either side of the boundary is different in the red map but the same in the green map. This indicates that the common axis of rotation for this boundary is [100]. The grain boundary marked by the square is just the opposite – same shading in the red map and different shading in the green map. This grain boundary has a different axis of rotation, namely [001].

**Pole figures** and inverse pole figures show the global texture of the area studied (but the spatial information is lost) and can be compared directly to x-ray diffraction pole figures. A pole figure is a stereographic projection showing the orientation of a pole (a normal to a lattice plane) relative to the sample reference frame (where RD and TD indicate the “rolling” and “transverse” directions in the plane of the sample). Examples of (001) and (111) pole figures are shown in Figure 3-9a. The interpretation of the (001) pole figure is that each grain is oriented with its (001) planes nearly parallel to the surface and the [001] direction in these planes nearly parallel to the sample surface normal direction. This (001) pole figure indicates a specific kind of texture, namely the cube texture that is common in rolled and recrystallized FCC metals.

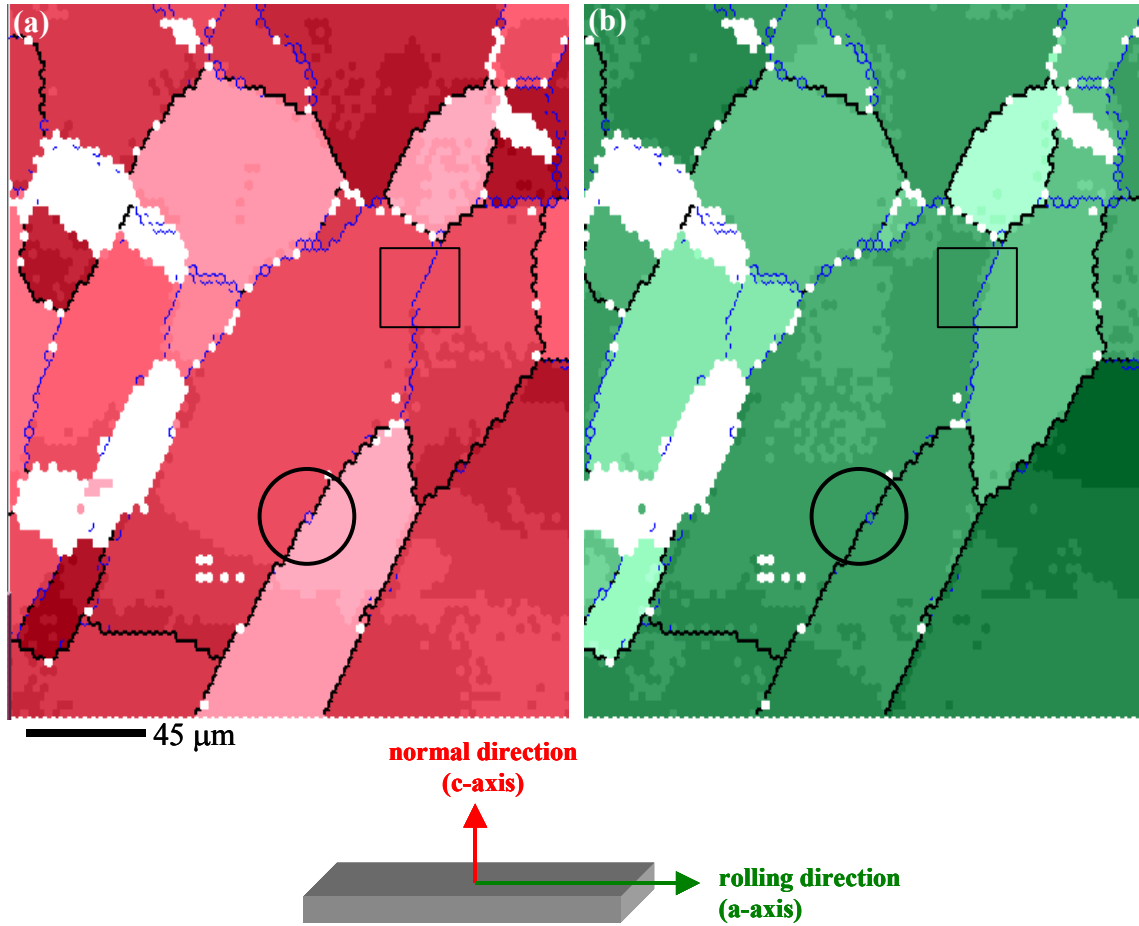


Figure 3-8. Grain boundaries overlaid on grain orientation maps where (a) is c-axis alignment and (b) is a-axis alignment with respect to the sample reference frame shown schematically below the maps. Grain boundary misorientations: 1-5° are blue and 5-15° are black.

An inverse pole figure is a stereographic projection showing the orientation of a sample direction relative to the crystal reference frame. The reference axes on the three corners of the inverse pole figure are the crystal directions [001], [101], and [111]. Thus, an [001] inverse pole figure (as shown in Figure 3-9b) shows that the [001] sample direction (or surface normal) is aligned with the [001] or c-axis. The degree of alignment is described by the scale to the right of the inverse pole figure in Figure 3-9b. The larger number represents a higher density of points within the colored contour in the inverse pole figure.

In this project, BEKP maps were produced on the superconductor, buffer layers, and nickel substrate to determine the local grain orientation and misorientation corresponding to regions of reduced  $J_c$  evident in MO images of magnetic flux penetration. The relative merits of the different kinds of BEKP maps, specifically the interpretation of percolation and grain boundary maps, will be further discussed in section 4-2.

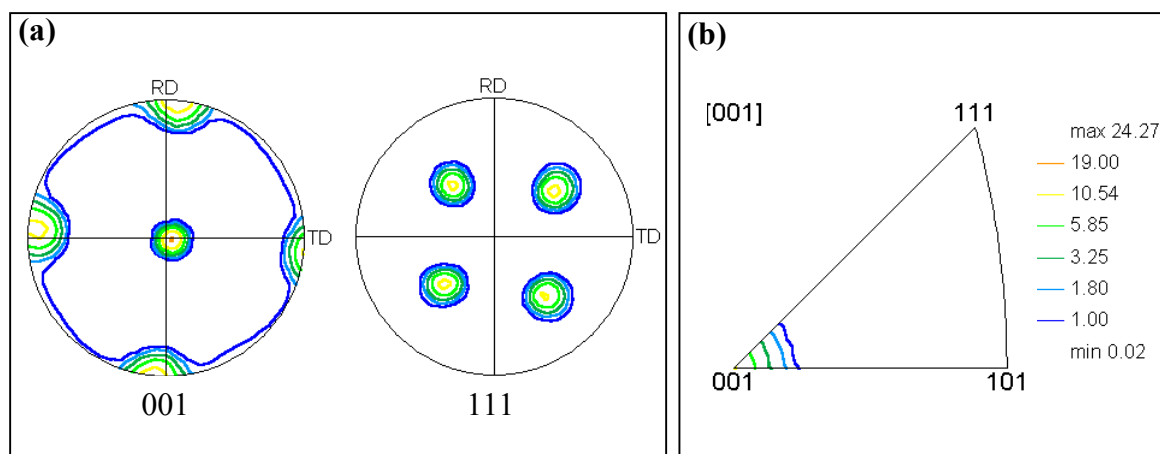


Figure 3-9. Examples of (a) pole figures and (b) inverse pole figures.

### **3-2. Magneto-Optical Imaging to Identify Current Blocking Defects**

Magneto-Optical (MO) imaging exploits the Faraday effect [15] to image the magnetic flux distribution above a sample. A layer of magneto-optically sensitive material is placed on top of the sample. Magneto-optically active materials have the valuable property that they rotate the polarization vector of incident light an amount that is proportional to the applied magnetic field. The local variations in the magnetic field “applied” to the indicator film by the sample below it correspond to changes in polarization, or color, in the image when viewed with polarized light [16]. MO images have a spatial resolution on the order of 5  $\mu\text{m}$ , depending on the domain structure and thickness of the indicator film as well as the distance between the film and the sample surface [17]. A Bi-doped iron garnet ( $\text{Y}_3\text{Fe}_5\text{O}_{12}$ ) film with in-plane polarization domains that are sensitive only to the z-component of the local magnetic field above the sample was used. In this work, the polarizers are rotated such that black corresponds to regions where no magnetic field is penetrating the superconductor, and bright areas correspond to regions of locally reduced  $J_c$  where magnetic flux has penetrated the sample.

Figure 3-10 shows bright features, indicating locally reduced  $J_c$ , that are characteristic of the MO images of all RABiTS-type coated conductors. A typical MO image with YBCO grown by the  $\text{BaF}_2$  method is shown in Figure 3-10a. Regardless of YBCO deposition method (Figure 3-10b, c), MO images of RABiTS-type coated conductors show a network of bright features that are typically 50-100  $\mu\text{m}$  in diameter. This network morphology is unique to RABiTS coated

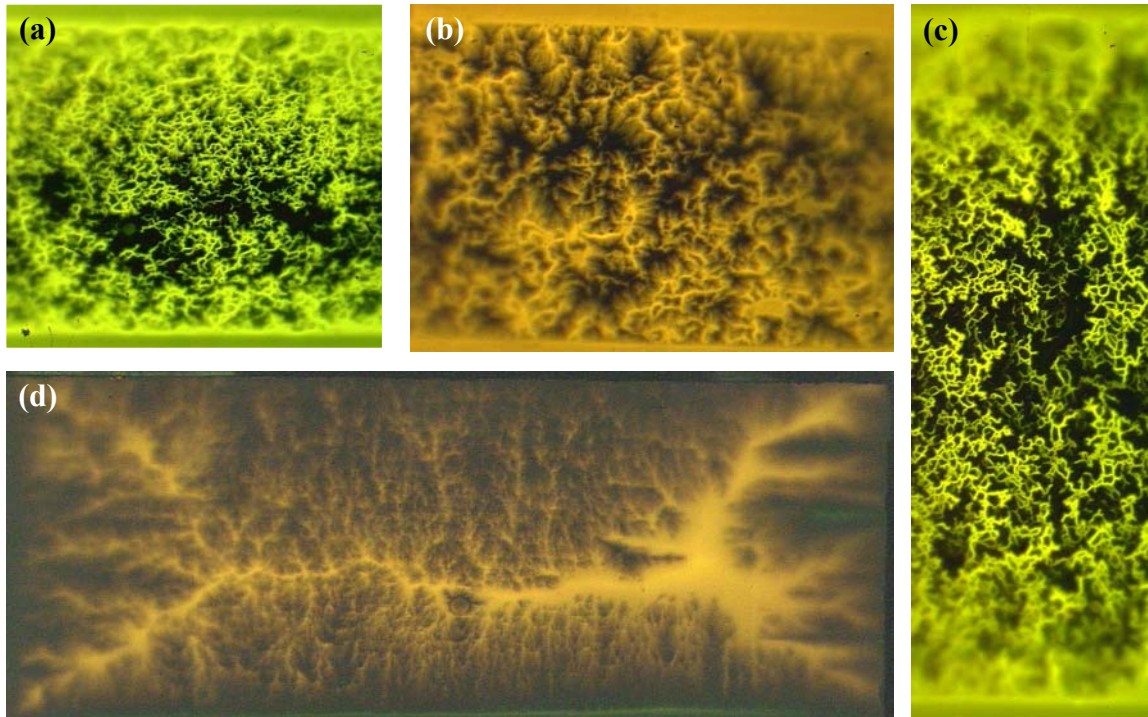


Figure 3-10. Zero-field-cooled MO images at 77K of RABiTS coated conductors with different YBCO deposition methods using (a) coevaporation of Y, BaF<sub>2</sub>, and Cu precursors (BaF<sub>2</sub> method); (b) Pulsed Laser Deposition (PLD method); and (c) Trifluoroacetate precursors (TFA method). For comparison, (d) is a MO image of IBAAD coated conductor showing different magnetic flux penetration patterns. In all images, bright regions show areas of magnetic flux penetration. The sample width is 3 mm. Courtesy of Matt Feldmann.

conductors; as shown in Figure 3-10d, MO images of IBAAD coated conductors have a much smaller scale flux penetration network.

In this study, MO images will be combined with microstructural and orientational imaging methods to show where and why flux is penetrating the coated conductor samples. Earlier studies of flux penetration in YBCO bicrystals [18, 19] have shown that grain boundaries become visible in MO images when the grain boundary (intergrain)  $J_c$  is smaller than the grain

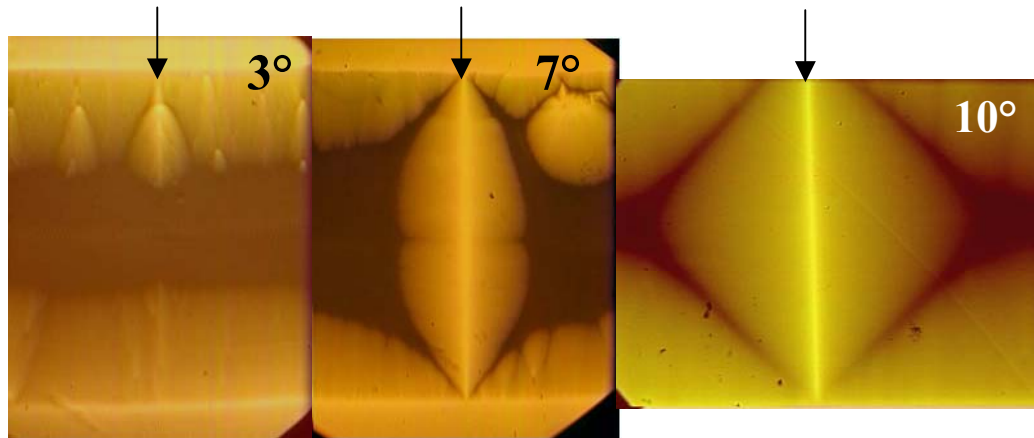


Figure 3-11. MO images of YBCO bicrystals with increasing grain boundary misorientation. At low angles, the flux is shielded from most of the grain boundary region, while flux totally penetrates the higher angle boundaries. Grain boundaries are marked with arrows. From [28].

interior (intragrain)  $J_c$ . The general conclusion from previous bicrystal experiments (Figure 3-11) is that the larger the misorientation angle, the brighter the boundary is in the MO image. Increasing brightness indicates that the grain boundary becomes a progressively weaker link with increasing angle, a result that is consistent with transport measurements on bicrystals. Thus, while it is difficult to exactly quantify the reduction of  $J_c$  in bright areas on coated conductors, the relative brightness of the image is a qualitative measure of the strength of the barrier.

### ***3-3. Focused Ion Beam Technology to Investigate Grain Boundary***

#### ***Microstructure***

This section describes the basics of the Focused Ion Beam (FIB) technique as well as how the FIB will be used to investigate current barriers in RABiTS-type YBCO coated conductors.

FIB is similar to SEM: a beam of charged particles impinges upon a sample in a vacuum chamber and the resulting interactions are analyzed using various detectors. Unlike an SEM, FIB uses a liquid Ga source that is drawn up a tungsten needle. The tip of the needle is coated in Ga and an extraction voltage is applied to ionize the Ga ions. The heavy ions are focused using electrostatic lenses [20].

For FIB analysis, a sample is attached to a 12 mm diameter stub with Ag paint. The sample is placed in a vacuum chamber where a beam of 25keV Ga ions is focused on the sample. Figure 3-12 shows by-products of the interaction between the Ga ions and the sample, including secondary particles (electrons, ions, and neutrals) and sputtered particles (neutrals, positive and negative ions). By rastering the incident Ga ion beam over the sample surface, images can be formed using the secondary electrons (as in an SEM) or secondary ions. A microchannel detector can be used to detect both secondary electrons and ions depending on whether the detector is biased positively or negatively. The images produced from detecting secondary electrons have contrast based on topography or crystallography. The contrast in secondary ion images is usually

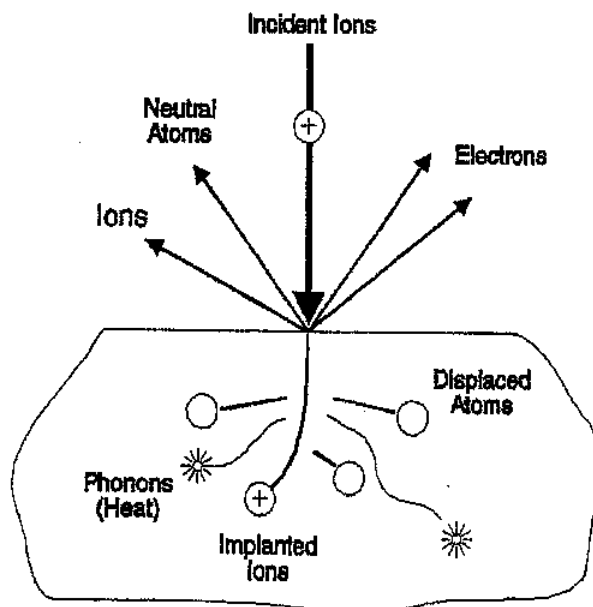


Figure 3-12. Schematic diagram showing the interactions of the incident Ga ion beam with the sample in a FIB. Courtesy of Bill Carmichael.

due to material contrast and is also more useful than secondary electron imaging when the sample is insulating.

By rastering the incident beam in a small user-defined region, the Ga ions sputter material off the sample, thereby “cutting” into the sample in a precisely controlled manner. This is how the FIB equipment was primarily used in these experiments. From the plan-view, one can identify a region of interest (in this case, a grain boundary groove that is visible in the YBCO layer) and use the incident Ga ions to sputter material away – in effect cutting down to the nickel substrate. An example of FIB-produced trenches (the rectangular features in the image outlined in white) is shown in Figure 3-13.



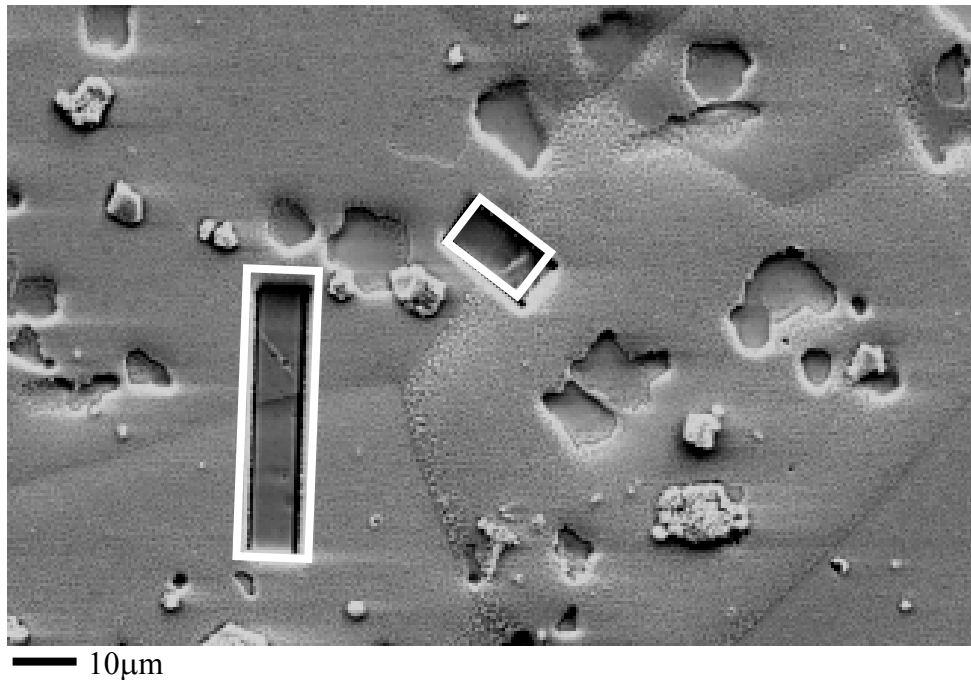


Figure 3-13. SEM image of a coated conductor surface with two FIB trenches (outlined in white) that were cut down to the substrate.

### 3-4. References

- [1] H. Wieland, *JOM* **46** #9 (1994) 37-41.
- [2] B.L. Adams, S.I. Wright and K. Kunze, *Met. Trans. A* **24** (1993) 819-31.
- [3] D.J. Dingley, *Scanning Electr. Microsc.* **11**(1984) 569-75.
- [4] J.A. Venables and C.J. Harland, *Phil. Mag* **27** (1973) 1193-1200.
- [5] T. Mason and B. Adams, *JOM* **46** #10 (1994) 43-45.
- [6] P. Camus, Noran Instruments Technical Notes series.
- [7] D.P. Field and D.J. Dingley, *Solid State Technology* **38** (1995) 91-6.
- [8] TSL Orientation Imaging Microscopy Technical Description.

- [9] D. Dingley and V. Randle, *J. Mat. Sci.* **27** (1992) 4545-66.
- [10] S. Wright, *J. Computer Assisted Microscopy* **5** (1993) 207-21.
- [11] D.B. Williams and C.B. Carter, *Transmission Electron Microscopy* (New York: Plenum Press, 1996).
- [12] OIM Academy tutorial notes.
- [13] Email from LEO sales representative Jeff Streger
- [14] A. Goyal, S.X. Ren, E.D. Specht, D.M. Kroeger, R. Feenstra, D. Norton, M. Paranthaman, D.F. Lee, and D.K. Christen, *Micron* **30** (1999) 463-478.
- [15] M.V. Indenbom, N.N. Kolesnikov, M.P. Kulakov, I.G. Naumenko, V.I. Nikitenko, A.A. Polyanskii, N.F. Vershinin and V.K. Vlasko-Vlasov, *Physica C* **166** (1990) 486.
- [16] L.A. Dorosinskii, M.V. Indenbom, V.I. Nikitenko, Y.A. Ossip'yan, A.A. Polyanskii and V.K. Vlasko-Vlasov, *Physica C* **203** (1992) 149-1992.
- [17] A.E. Pashitski, "Investigation of Magnetic Flux Distribution and Current Flow in High-Temperature Superconductors by Means of Magneto-Optical Imaging," Ph.D. thesis, 1998.
- [18] N. Heinig, R.D. Redwing, I.F. Tsu, A. Gurevich, J.E. Nordman, S.E. Babcock and D.C. Larbalestier, *Appl. Phys. Lett.* **69** (1996) 577-79.
- [19] A.A. Polyanskii, A. Gurevich, A.E. Pashitski, N.F. Heinig, R.D. Redwing, J. E. Nordman, and D.C. Larbalestier, *Phys. Rev. B* **53**(13) (1996), 8687-8697.
- [20] M.W. Phaneuf, *Micron* **30** (1999) 277-88.

## **4. YBCO Studies**

### ***4-1. Origin of current barriers***

Macroscale (1-100  $\mu\text{m}$ ) barriers to current in the YBCO layer of RABiTS-type coated conductors were investigated on two different types of sample using a combination of analysis techniques. The two sets of coated conductor samples had different methods of YBCO deposition. One method was Pulsed Laser Deposition (PLD) where YBCO target material was vaporized with a laser. In comparison, the  $\text{BaF}_2$  YBCO was grown using e-beam co-evaporation of Y,  $\text{BaF}_2$ , and Cu precursors followed by post-annealing to form YBCO. These two sets of samples were investigated using a combination of scanning electron microscope (SEM) imaging, magneto-optical (MO) imaging, Focused Ion Beam (FIB) cutting, and backscattered electron Kikuchi pattern (BEKP) analysis. Grain boundaries in the nickel substrate were shown to influence the microstructural connectivity of the YBCO grains and were shown to be the source for low  $J_c$  regions that limited the overall  $J_c$  of the sample.

### **PLD YBCO coated conductors**

Experiments to explore the cause of the spatial variations in  $J_c$  were conducted on multiple RABiTS-type coated conductor samples supplied by Tim Peterson and co-workers at AFRL. All buffer layers and the YBCO layer were deposited by PLD. 100nm of  $\text{CeO}_2$ , 500nm of YSZ, and 100nm of  $\text{CeO}_2$  were deposited on the nickel substrate. The difference between the samples was the YBCO layer thickness, which varied from 300-1200nm.  $J_c$  measurements in

self-field at 77K yielded a  $1.2\text{MA}/\text{cm}^2$  value for the 600nm thick sample;  $J_c$  was not measured on the other samples.

MO images obtained under standard imaging conditions [1, 2] were used to locate the areas of reduced  $J_c$  in the YBCO layer. The MO image of a sample with 300nm thick PLD YBCO is shown in Figure 4-1a; the polarizers were rotated such that higher  $J_c$  regions appear dark. Bright areas indicate the locations of magnetic flux penetration that correspond to regions of locally depressed  $J_c$ . The most striking features in the MO image in Figure 4-1a are electromagnetically well-connected regions surrounded by bright lines that range in diameter from 50-100  $\mu\text{m}$ . Figure 4-1b shows the light microscopy image of the surface of the YBCO. Figure 4-1c shows the overlay of the MO image and the light microscopy image. The overlay suggests that many, but not all, of the boundaries visible in the light microscope image of the YBCO correspond to bright lines, and thus regions of locally depressed  $J_c$ , in the MO image.

In addition, most of the low  $J_c$  regions in MO images are coincident with macroscale grain boundary grooves in the YBCO. Arrows on the left in Figure 4-2 highlight the grain boundary grooves visible in the representative plan-view SEM image of PLD YBCO. These grooves have also been seen in the substrate, buffer layers and YBCO layers of coated conductor samples grown by other groups using a wide variety of buffer and YBCO layer deposition methods [3-8]. The other defects visible in Figure 4-2 are small patches where the YBCO has “pulled off” during growth. These defects are also sometimes seen in the microstructure of PLD YBCO grown on  $\text{SrTiO}_3$  bicrystals [9].



To determine what was causing the macroscale boundaries in the YBCO, FIB was used to cut trenches across boundaries that appeared in the YBCO layer. A thin layer (about 1  $\mu\text{m}$ ) of Pt was deposited before cutting with the Ga ions in the FIB. Energy Dispersive spectroscopy (EDS) was used to confirm that the FIB cut down to the nickel substrate (Figure 4-3). The small Pt and Ga peaks in the EDS spectrum are from the FIB cutting process. The features in the bottom of the FIB trenches line up with the boundaries seen in the YBCO layer that are highlighted with arrows in Figure 4-4. BEKP analysis on the nickel at the bottom of the trenches confirmed that the features were indeed nickel grain boundaries with varying misorientation angles. Therefore, FIB trenches cut through all the buffer layers at the position of the grain boundary grooves in the YBCO confirm that these boundaries appear directly over grain boundaries in the nickel substrate to within the 1 micrometer resolution of the technique.

### **BaF<sub>2</sub> YBCO coated conductors**

Similar current barriers are observed in MO images of RABiTS-type coated conductors from Feenstra and Goyal and coworkers at ORNL. The architecture of these samples was YBCO/CeO<sub>2</sub>/YSZ/Y<sub>2</sub>O<sub>3</sub>/Ni. The YBCO was grown using the BaF<sub>2</sub> method on top of RF-magnetron sputtered buffer layers CeO<sub>2</sub> and YSZ. The Y<sub>2</sub>O<sub>3</sub> seed layer was grown by reactive evaporation from Y metal on top of rolled and recrystallized nickel. The bright features in the MO image of BaF<sub>2</sub> YBCO (Figure 4-5) are suggestive of the influence of the nickel substrate as seen in the PLD YBCO samples. The long, straight bright lines in Figure 4-5 are where the laser was used to cut a bridge for electrical characterization of the YBCO.







A plan-view SEM image of the BaF<sub>2</sub>-deposited YBCO is shown in Figure 4-6. Unlike the PLD YBCO samples, “pull-off” of the BaF<sub>2</sub> YBCO was not a problem; rather Cu-rich particles are common on the surface. In Figure 4-6 grain boundary grooves are highlighted with arrows. The extent of grooving is much less in BaF<sub>2</sub>-grown YBCO compared to PLD YBCO in the samples investigated. However, Figure 4-6 does show that grooving is present even in high J<sub>c</sub> (2.3 MA/cm<sup>2</sup>) BaF<sub>2</sub> YBCO samples. As with the PLD YBCO samples, bright regions in MOI images are associated with grooving in the BaF<sub>2</sub> YBCO. A general trend was seen when the microstructure of YBCO was investigated using plan-view SEM over large areas (mms). In general for both PLD and BaF<sub>2</sub> YBCO, grooved regions are bright in MOI, but not all MOI bright regions are grooved.

FIB trenches were cut through all buffer layers at the position of the grain boundary grooves in the BaF<sub>2</sub> YBCO (Figure 4-7). EDS again confirmed that the trenches were cut down to the nickel substrate and BEKP confirmed that the boundary (marked with an arrow in Figure 4-7) at the bottom of the FIB trenches was a nickel grain boundary. An SEM image of the FIB trenches confirm that boundaries in the YBCO appear directly over grain boundaries in the nickel substrate to within the 1 micron resolution of the technique.

#### ***4-2 Distribution of nickel grain boundaries***

The previous section showed that in both PLD and BaF<sub>2</sub> YBCO coated conductors with the RABiTS-type architecture, the boundaries visible in plan-view SEM images and the bright





features in MO images were due to underlying nickel grain boundaries. BEKP was used to investigate the character and distribution of the nickel grain boundaries in order to determine which boundaries induce weak-link behavior in the YBCO.

### **PLD YBCO coated conductors**

BEKP was used to determine the grain boundary distribution in a large region (hundreds of square microns) of the nickel substrate after the 1.2  $\mu\text{m}$  thick PLD YBCO and buffer layers were removed by chemical etching. The superconductor was removed using a 1% mixture of nitric acid in deionized water. The etchant for the buffer layers was a 2:3 mixture of  $\text{NH}_4\text{F}$  (40%) and HF (48%). EDS confirmed that the superconductor and the buffer layers were removed. The BEKP data was collected under the usual SEM conditions: 70° sample tilt, 20kV accelerating voltage, 120  $\mu\text{m}$  aperture, and 15mm working distance. The beam was rastered over a roughly 500  $\mu\text{m}$  wide region with 3  $\mu\text{m}$  step size.

A series of BEKP percolation maps from the nickel substrate plotted with tolerance angles from 1°-6° are shown in Figure 4-8. As described in Chapter 3, a grain in a percolation map is defined as a set of points for which each point has at least one neighbor with the same crystallographic orientation within the specified tolerance angle. Each grain is shaded a different color in the percolation map. The 1° percolation map correlates well to the light microscope image of the nickel substrate.



Figure 4-8 shows that increasing the threshold angle of the BEKP percolation map reduces the number of grains shown in the map, while the average grain size increases.

Percolation maps with varying tolerance angles ( $0.5^\circ$ ,  $1^\circ$ ,  $2^\circ$ ,  $2.5^\circ$ ,  $3^\circ$ , and  $5^\circ$ ) from the literature [10] are shown in Figure 4-9 for comparison. With increasing tolerance angle, the percolation maps again show a reduction in the number of grains and an increase in the average grain size. At a certain point, the percolation map becomes almost monochromatic; all of the points in the BEKP scan have neighbors that are within a certain tolerance angle of each other. In Figure 4-9, the tolerance angle where the percolation map becomes almost entirely monochromatic is  $3^\circ$ , while in Figure 4-8 the percolation map becomes monochromatic at  $4^\circ$ . The slightly smaller tolerance angle in the literature may be related to the different texture of that nickel substrate compared to the texture of the PLD YBCO substrate. Figure 4-10 shows pole figures from the two samples. The BEKP data plotted in both pole figures shows the same cube-on-cube texture, but the colored regions in the literature pole figure are slightly smaller in diameter than the colored regions in the PLD YBCO pole figure. The smaller diameter, colored regions indicate a better texture in the nickel.

This single color in a percolation map represents a percolatively connected region. According to interpretations in the literature [10, 11], the  $4^\circ$  percolation map in Figure 4-8 and the  $3^\circ$  percolation map in Figure 4-9 suggest that the majority of the sample is single-crystal-like with respect to current flow. However, this interpretation does not agree with the many bright regions, indicative of locally reduced  $J_c$ , visible in the MO images of RABiTS-type coated conductors. In fact, it is possible for a percolation map to be monochromatic with a low tolerance





angle when the sample contains high angle grain boundaries. This will be discussed in more detail later.

Figure 4-11 is a collection of grain boundary maps. Each map shows the location of all grain boundaries for which the grain boundary misorientation angle,  $\theta$ , is greater than the value indicated on the image, in this case from  $2^\circ$  through  $7^\circ$ . The  $\theta > 2^\circ$  map shows the densest grain boundary network, while the  $\theta > 7^\circ$  map in Figure 4-11 has the least dense grain boundary network. Figure 4-12 is a histogram of the fraction of the total grain boundary length as a function of grain boundary misorientation angle. For the 96 grain boundaries in this region of the sample, the histogram shows that the almost half of the grain boundary line length is very low angle – about  $1-2^\circ$ .

Figure 4-13 is a comparison of the  $\theta > 4^\circ$  grain boundary map, the  $4^\circ$  percolation map, and the MO image. There is an almost one-to-one correlation between the location of nickel grain boundaries with  $\theta > 4^\circ$  and the flux penetration network visible in the MO image. This comparison indicates that the YBCO that grows above nickel grain boundaries with  $\theta > 4^\circ$  has reduced  $J_c$ . It is important to note that several high angle grain boundaries that are visible in the grain boundary map and MO images are not evident in the percolation map. This comparison indicates that percolation maps do not show all barriers to current flow.

The difference between, and the importance of, percolation maps and grain boundary maps is illustrated in Figures 4-14 and 4-15. Figure 4-14 is an example of how a  $2^\circ$  percolation





map is made. Figure 4-14a shows a hexagonal array of points with given orientations. The numbers in each hexagon represent the hypothetical misalignment of each point with respect to the sample reference frame. Consider the points in the first row of the array (which are outlined in bold for emphasis) in Figure 4-14b. To make a  $2^\circ$  percolation map, a neighboring point will be shaded green if the neighboring point is within  $2^\circ$  of the point in the first row. For this example, the assumption is that the misorientation between two points is given by subtracting the two angles. In Figure 4-14b, X marks a point that is greater than 2 degrees from the first row neighboring grain and thus not shaded green.

Now consider the outlined points in the second row of the array in Figure 4-14c. Again, neighbors are shaded green if they are within the  $2^\circ$  criterion of the percolation map. Notice that the point previously marked with an X in Figure 4-14b can now be shaded green in Figure 4-14c because it is within 2 degrees of a second row point.

By repeating this procedure for all the rows (Figure 4-14d-f), the entire map is shaded green. The interpretation of the map in Figure 4-14f is that the entire region is percolatively connected within  $2^\circ$ . For superconductors, this interpretation in the literature implies that there is a current path throughout the sample such that the current never has to cross a boundary with misorientation angle greater than  $2^\circ$ .

However, the grain boundary map in Figure 4-15a shows that there are some grain boundaries (highlighted in red) that have misorientation angles greater than  $2^\circ$ . These boundaries can have a dramatic effect on current flow. In the most basic case, consider one-dimensional





current flow as depicted in Figure 4-15b. The solid black arrows show uninterrupted current flow from bottom to top; the dashed black arrows depict current that is blocked by boundaries greater than  $2^\circ$ . In this case, as well as in the case of current flow from left to right shown in Figure 4-15c, 50% of the cross-sectional area is blocked by  $2^\circ$  boundaries.

As this hypothetical example illustrates, monochromatic percolation maps imply that there is a fully connected path through the microstructure that is within the chosen tolerance angle criterion of the map. However, it is the grain boundary map that displays the constrictions of the current path. The grain boundary map also correlates to the observed regions of reduced  $J_c$  in the superconducting layer. Thus it is the grain boundary map and its correlation to the MO image that confirms the role of the nickel grain boundaries in the constriction of the current flow in the epitaxial YBCO layer. Grain boundary maps are an important tool, preferable to percolation maps, for measuring the improvement of the coated conductor by identifying remaining high angle grain boundaries that will restrict current flow.

The magnitude of flux penetration in the YBCO above more than 60 of the nickel grain boundaries was estimated by measuring the MO image intensity, which is roughly proportional to the penetrating magnetic field. The MO images used for this measurement were recorded when the sample was in its critical state; in other words, further increasing the magnetic field did not lead to any more grain boundaries becoming bright in the MO image. A plot of the MO image intensity vs. nickel grain boundary misorientation angle in Figure 4-16 shows that there is an abrupt change in MO intensity at  $4^\circ$ : magnetic flux does not preferentially penetrate grain boundaries with  $\theta < 4^\circ$ , while boundaries with  $\theta > 4^\circ$  exhibit MO contrast. Above the  $4^\circ$  threshold



angle, the magnitude of flux penetration varies considerably and not very systematically with  $\theta$ . Possible causes of this variation may include grain boundary contamination or grooving as well as the unknown effect of the grain boundary plane or the mosaic spread in the YBCO layer. The possible influence of mosaic spread, which is the local orientation variations from island to island in the YBCO layer, will be discussed in section 4-3.

To summarize, the character and distribution of nickel grain boundaries was shown with BEKP percolation and grain boundary maps. Percolation maps are useful in showing that there is a percolatively connected region for current flow in coated conductors. However, caution must be used in further interpretation of percolation maps, since this work has shown that it is possible for a percolation map to be monochromatic with a low tolerance angle while still containing high angle grain boundaries. The correlation between microstructure and electromagnetic properties was best illustrated with the BEKP grain boundary, not percolation, maps and MO images. BEKP grain boundary maps were used to define a threshold angle in the nickel substrate – the grain boundary angle in the nickel above which the boundary in the YBCO appears bright, indicating depressed  $J_c$ , in MO images. The presence of a sharp threshold angle at  $4^\circ$  suggests that one way to improve  $J_c$  in coated conductors is to make nickel substrates where all of the grain boundaries have  $\theta < 4^\circ$ .

### **BaF<sub>2</sub> YBCO coated conductors**

As previously described, the ORNL coated conductors studied were BaF<sub>2</sub>-grown YBCO on RABiTS substrate for which the overall  $J_c$  was 2.3MA/cm<sup>2</sup>. The grain boundary distribution

in ORNL substrates was determined using BEKP analysis on three regions of the nickel substrate after the 0.3  $\mu\text{m}$  thick YBCO and buffer layers were removed. As with the AFRL samples, the superconductor was removed using a 1% mixture of nitric acid in deionized water. The buffer layers were sputtered off instead of being chemically removed since NiO was sometimes observed after chemical etching. EDS confirmed that the superconductor and the buffer layers were completely removed.

A laser was used to cut three "bridges" of different lengths and widths in the sample to limit the region current could flow through. Each of these bridges was MO imaged with the YBCO layer intact. Plan-view secondary electron SEM images were taken of the surface before and after removing the superconductor and buffer layers. BEKP grain boundary maps were produced on the nickel substrate.

Figure 4-17 shows the results from bridge 1, which was the largest bridge that was cut. Figure 4-17a is a plan-view SEM image of the nickel substrate after the superconductor and buffer layers were removed. The horizontal lines near the top and bottom of the image are where the laser was used to cut the bridge that was 1.5 mm long by 275  $\mu\text{m}$  high. The contrast in the SEM image is due to the differing orientations of the nickel grains. The average nickel grain size was determined to be 60  $\mu\text{m}$  by the linear intercept method, while the grains ranged in diameter from 20-150 $\mu\text{m}$ .

Figure 4-17b is a BEKP grain boundary map with  $\theta > 1^\circ$ . This map correlates well with the location of the grain boundaries shown by the change in contrast in Figure 4-17a. Figure 4-17c is a MO image overlaid with the  $5^\circ$  grain boundary map (shown in red). Figure 4-17c shows



a good correlation between boundaries that are bright in the MO image and boundaries that have misorientations greater than  $5^\circ$ . Thus in these BaF<sub>2</sub> YBCO samples, the threshold angle of the nickel substrate was approximately  $5^\circ$ . In other words, the YBCO above nickel grain boundaries with  $\theta < 5^\circ$  could carry as much current as the bulk YBCO. This threshold angle is not very different from the  $4^\circ$  threshold angle observed in the PLD YBCO coated conductor substrates. Within the  $0.5^\circ$  precision of the BEKP technique, the threshold angle of the AFRL and ORNL samples are almost the same.

While there are fewer grain boundaries present in the  $5^\circ$  map compared to the  $2^\circ$  map, the  $5^\circ$  grain boundaries still comprise a rather large fraction of the total number of grain boundaries. Figure 4-18 is a histogram showing the grain boundary line length as a function of misorientation angle. For the 250 grain boundaries in this region of the sample, this histogram shows that over 60% of the total grain boundary line length has misorientation angle greater than  $5^\circ$ , with almost one quarter of the line length having misorientations greater than  $9^\circ$ . This is in contrast to the nickel used for the PLD samples shown in Figure 4-12 where only 5% of the total grain boundary length had  $\theta > 9^\circ$ .

The high angle ( $\theta > 9^\circ$ ) nickel grain boundaries are not uniformly distributed throughout the bridge. Figure 4-19 shows a clustering of these boundaries near the center of, and almost completely spanning, the bridge. When the critical current of this bridge was measured, the  $J_c$  was only  $0.7 \text{ MA/cm}^2$ , compared to the  $J_c = 2.3 \text{ MA/cm}^2$  of the entire sample. The clustering of the





high angle grain boundaries near the center of the bridge was largely responsible for the relatively low  $J_c$  of the bridge.

### **4-3. Influence of nickel grain boundaries**

The previous section described the character and distribution of nickel grain boundaries in the substrate of both PLD YBCO and BaF<sub>2</sub> YBCO coated conductors. Despite having different YBCO deposition methods, the samples from AFRL and ORNL had similar threshold angles of 4-5° in BEKP grain boundary maps of the nickel substrate. This section describes first how the underlying nickel grain boundaries influence the orientation and morphology of the PLD YBCO layer at a small number of nickel grain boundaries. For a large number of nickel grain boundaries, texture transfer was examined in the case of the BaF<sub>2</sub> YBCO on RABiTS substrate where it was possible to characterize large areas of the YBCO with BEKP.

#### **PLD YBCO coated conductors**

BEKP was used to investigate the difference in PLD YBCO grain orientation near one grain boundary groove that appeared bright in a MO image and near 3 boundaries that did not appear in the MO image. A BEKP map of the 300 nm thick PLD YBCO was very noisy due to the surface roughness. Individual Kikuchi patterns were obtained from locally smooth regions on the YBCO surface using a very low noise CCD camera with long acquisition times at Noran Instruments' facility. Figure 4-20 shows the Kikuchi patterns from adjacent grains. The same Kikuchi pattern was formed from all four grains, but there was a difference in the positioning of the Kikuchi pattern from one grain to another. To qualitatively illustrate the change in Kikuchi



pattern positioning that represents the grain boundary misorientation in the YBCO layer, a triangle formed by the intersection of bands in the Kikuchi pattern was traced on pattern D in Figure 4-20. Comparing the rotation of the Kikuchi pattern in B relative to the fixed triangle position in D shows that there was a small misorientation between grains B and D. In contrast, the difference in Kikuchi pattern position in A and B indicates a larger misorientation. To quantify the grain boundary misorientation in the YBCO, BEKP software was used to determine the Euler angles that described the orientation of each grain; the misorientation between each grain was manually calculated. A diagram of the four YBCO grain boundary grooves labeled with the grain boundary misorientation angle and axis is shown in Figure 4-20. A comparison of the MO image and the misorientation data shows that the bright boundary in the MO image, indicative of locally depressed  $J_c$ , corresponds to a higher misorientation angle in the YBCO, specifically  $4.2^\circ$ , between grains A and B.

To determine the nickel grain boundary misorientation in this same region, the YBCO and buffer layers were chemically removed. Unfortunately, a thick layer of NiO formed after the chemical etching. After polishing off the NiO, it was impossible to find the exact same region on the nickel substrate. Experiments were done on different samples (discussed in a later section) to determine how the nickel grain boundary misorientation angles are transferred to the buffer and YBCO layers.

In addition to the YBCO grain orientation, the morphology of the YBCO grains was influenced by nickel grain boundary angles greater than  $4^\circ$ . Figure 4-21 is a representative plan-view SEM image of PLD YBCO. The YBCO grain morphology in region B appears poorly



connected and porous compared to region A. FIB cutting was used to remove the YBCO and buffer layers. BEKP maps were made on the underlying nickel substrate. The average of ten nickel grain boundary misorientation measurements is labeled near the YBCO grain boundary grooves in Figure 4-21. The SEM image shows that the YBCO that grew above higher angle nickel grain boundaries ( $4.4^\circ$  and  $5.6^\circ$ ) appears more porous than the YBCO that grew above a smaller angle boundary ( $3.3^\circ$ ).

Combined BEKP analysis and SEM and MO imaging on PLD YBCO coated conductors show that the grain boundary grooves between YBCO regions that are misoriented by more than  $4^\circ$  have locally reduced  $J_c$  and a less dense morphology. This was in good agreement with the  $4^\circ$  threshold angle determined on the nickel substrate.

### **BaF<sub>2</sub> YBCO coated conductors**

To show how texture was transferred from substrate to buffer layers to superconductor, BEKP scans needed to be taken over large areas on the YBCO and buffer layers and nickel substrate. There were several difficulties that needed to be overcome in order to obtain BEKP data on large areas of the superconductor. The nature of the coated conductor samples makes data collection difficult for two main reasons: sub-micron YBCO island size and surface inhomogeneity. The small island size of the YBCO (as illustrated in Figure 4-22a) makes it necessary to use a very small step size in BEKP scans, and thus limits the size of the area that can be examined in a reasonable time frame. Surface inhomogeneity due to the presence of contaminants, second phase particles, pores, and the island-like structure of the YBCO itself



produce a lot of noise in the scans because BEKP was very sensitive to surface roughness. Also, the YBCO surface degrades over time with exposure to air, so “fresh” samples, where the YBCO was grown and the samples mailed out the same day, were a necessity.

Smooth, fresh BaF<sub>2</sub> YBCO coated conductors were obtained from Feenstra and coworkers at ORNL for texture transfer studies. The architecture of these samples was YBCO/CeO<sub>2</sub>/YSZ/Y<sub>2</sub>O<sub>3</sub>/Ni. These coated conductor samples, grown on commercial nickel substrates, had a J<sub>c</sub> of 0.58 MA/cm<sup>2</sup>. According to Feenstra, coated conductor samples grown on commercial nickel to date have a maximum J<sub>c</sub> of 1.1 MA/cm<sup>2</sup>. Two plan-view SEM images of these samples are shown in Figure 4-22. The secondary electron image taken at 5kV in Figure 4-22a shows the YBCO island size on the order of 0.5 μm. Figure 4-22b is a SEM image taken at 20kV when the sample was tilted 70° for BEKP analysis and shows a network of grooves in the YBCO that most likely delineate the underlying nickel grain boundaries. BEKP maps 300 μm wide were made on the superconductor, YSZ buffer layer, and nickel substrate to investigate texture transfer from the nickel to the BaF<sub>2</sub> YBCO.

Figure 4-23 compares the grain boundary network in the nickel substrate and the YSZ buffer layer. The grain boundary maps are shown in three sets; in Figure 4-23a for example, the gray boundaries are 2-3°, the blue boundaries are 3-4°, the green boundaries are 4-5°, and the red boundaries are >5°. At first inspection, the grain boundary network looks almost the same in the substrate and in the buffer layer. However, there are some grain boundaries that change misorientation from the nickel to the buffer layer. For example, the white solid arrows in Figure 4-23a show grain boundaries in the nickel that become lower misorientation angle in the buffer





layer, while the white dashed arrows show nickel boundaries that become higher angle in the YSZ. All six of the BEKP maps in Figure 4-23 were examined to find the 29 grain boundaries that changed misorientation angle out of the approximately 170 total number of grain boundaries. Table I shows the comparison of these grain boundaries misorientation angles in the nickel and the YSZ. Often a grain boundary in the BEKP map was shaded with two colors; in this case the average grain boundary misorientation angle is listed. In the table,  $\Delta$  represents the change in misorientation angle from nickel to YSZ. A positive  $\Delta$  represents an improvement in texture; in other words, the misorientation across the underlying nickel grain boundary was larger than that of the YSZ grain boundary above it. A negative  $\Delta$  indicates that the misorientation angle was smaller in the nickel than in the YSZ.

Table I

Grain boundary misorientation angles (in degrees) for select boundaries in the nickel substrate and YSZ later.  $\Delta$  represents the change in misorientation angle from substrate to buffer.

Nickel	YSZ	$\Delta$ (°)
1.5	3	-1.5
5.5	3.5	+2
2	1	+1
5.5	4.5	+1
3.5	1.5	+2
4	5	-1
4	4.5	-0.5
1.5	2.5	-1
7.5	4.5	+3
8.5	4.5	+4
6	5	+1
8	10	-2
10	8	+2
6	9	-3
6	8.5	-2.5

Nickel	YSZ	$\Delta$ (°)
6	7	-1
11.5	13	-1.5
13	11	+2
10	8	+2
12	11	+1
11.5	13	-1.5
11	9	+2
11	13	-2
11	9	+2
10	12.5	-2.5
9	8	+1
8	8.5	-0.5
11	8	+3
9	8	+1

According to Table I, about half (16 of 29) of the grain boundaries in the nickel became lower angle when YSZ was epitaxially grown on it. The average texture improvement was  $1.9^\circ \pm 0.9^\circ$ , although three boundaries improved by 3-4°. The other thirteen grain boundaries in the YSZ had higher misorientation angles than the original nickel boundary. The average texture worsening for these specific boundaries was  $1.6^\circ \pm 0.8^\circ$ , with a range of 0.5-1.5°. Overall, there appears to be no substantial improvement in grain boundary misorientation – for these 29

boundaries that changed orientation from nickel to YSZ, about half of the boundaries improved by  $\sim 2^\circ$  while the other half of the boundaries worsened by  $\sim 1.5^\circ$ . The change in misorientation angles may be due to the mosaic spread in the buffer layer.

The previous analysis provides statistics of a small number of select grain boundaries. To get a more global picture of texture transfer from substrate to buffer layer, BEKP grain orientation maps were compared in Figure 4-24. The grain orientation was depicted according to the legend in Figure 4-24 – gray represents a-axis misalignment by  $0-5^\circ$ , red represents a-axis misalignment by  $5-10^\circ$ , and white represents a-axis misalignment by  $10-15^\circ$ . Black regions are either noise (a BEKP pattern was not formed due to surface contamination) or a misalignment by more than  $15^\circ$ . Similarly,  $0-5^\circ$ ,  $5-10^\circ$ , and  $10-15^\circ$  c-axis misalignment is represented by blue, green, and white respectively. On first inspection, Figure 4-24 qualitatively shows that the texture in the substrate and the buffer layers is quite similar. In order to quantify a texture change from nickel to YSZ, Photoshop<sup>TM</sup> was used to measure the number of pixels of each color in the grain orientation maps of Figure 4-24. Table II shows the calculated area fraction of each color (representing a range of grain orientations) in each map.



Table II

Area percentage of a-axis and c-axis alignment in grain orientation maps of Figure 4-24.

a-axis			c-axis		
	Nickel	YSZ		Nickel	YSZ
0-5°	38.1%	30.3%	0-5°	38.9%	33.9%
5-10°	46.7%	53.8%	5-10°	53.0%	55.5%
10-15°	15.2%	15.9%	10-15°	8.1%	10.6%

The a-axis alignment appears to remain about the same from nickel to YSZ in the high angle ( $>10^\circ$ ) range. In the  $\theta < 10^\circ$  range, the texture slightly worsens. In other words, the area fraction of YSZ grains with a-axis and c-axis orientation of 0-5° with respect to the sample reference frame decreased by 8% and 5% respectively compared to the nickel. This BEKP grain orientation data confirms texture measurements by x-ray diffraction. X-ray experiments show that the texture, as measured by the FWHM (full-width-half-maximum) of x-ray pole figures, is approximately the same or slightly worse in the buffer layer compared to the nickel substrate of RABiTS-type coated conductors. The FWHM of the [111] pole figure on the rolled and recrystallized nickel substrate was 8-9°, while the FWHM of the buffer layer was 8-10°[12].

Next the texture of the superconductor was investigated. BEKP analysis of one YBCO region is shown in Figure 4-25. Figure 4-25 shows three BEKP grain boundary maps (2°, 5°, 10°); grain orientation maps showing a-axis alignment (green shading) and c-axis alignment (red shading); a light microscope image of the surface of the YBCO; and two inverse pole figures.







Grain boundary maps on the BaF<sub>2</sub>-deposited YBCO (Figure 4-25 a-c) show that high angle boundaries are not completely eliminated in the superconductor layer. Many of the visible grain boundaries in the light microscope image (Figure 4-25f) correspond to grain boundaries shown in the  $\theta > 5^\circ$  and  $\theta > 10^\circ$  BEKP grain boundary map. Previous experiments have shown that YBCO grain boundary grooves that are visible in the SEM and light microscope correspond to underlying nickel grain boundaries and often are visible as regions of flux penetration, and reduced  $J_c$ , in MO images. Therefore, the remaining high angle grain boundaries shown in the  $\theta > 10^\circ$  grain boundary map may be responsible for the rather low  $J_c$  (0.58MA/cm<sup>2</sup>) of this sample.

The grain orientation maps in Figure 4-25d-e are shaded such that the differences in green and red show differences in a-axis and c-axis alignment respectively. Similarly, in Figure 4-25g-h, the BEKP data points in both pole figures tend to cluster quite closely to the  $\langle 001 \rangle$  and  $\langle 011 \rangle$  showing the c-axis and a-axis alignment, respectively.

After analysis of the BaF<sub>2</sub> YBCO layer, it was chemically removed with a 1% nitric acid in water solution. EDS confirmed that the YSZ layer remained after chemical etching. Figure 4-26 is a comparison of the grain orientation maps from the same region on the YSZ buffer layer and superconductor. In previous grain orientation maps, a-axis and c-axis alignment were shown by shading of green and red respectively. To highlight differences in grain orientation, the color shading was changed according to the legend in Figure 4-26 – gray represents a-axis misalignment by  $0-5^\circ$  with respect to the RD reference direction ( $[110]$  or in-plane alignment)



while red and white represent a-axis misalignment by 5-10° and 10-15° respectively. Similarly, 0-5°, 5-10°, 10-15° c-axis misalignment with respect to the sample normal direction ([001] or out-of-plane alignment) is represented by blue, green, and white respectively. Black color in both maps represents either noise or grain orientation >15° with respect to the directions in the sample reference frame.

Qualitatively, Figure 4-26 shows that there is more red and less gray in the superconductor map than in the buffer layer map; in other words, a-axis alignment worsens from the YSZ to the YBCO layer. In comparison, the c-axis alignment improves (more blue and less green) from the buffer to the superconductor. In both maps, there is a relatively small fraction of grain area that is oriented 10-15° from the [110] or [001] directions in the sample reference frame. In order to quantify this texture change from YSZ to YBCO, Photoshop<sup>TM</sup> was used to measure the number of pixels of each color in the grain orientation maps of Figure 4-26. The results are shown in Table III.

Table III

Area percentage of a-axis and c-axis alignment in grain orientation maps of Figure 4-26.

	a-axis	
	YSZ	YBCO
0-5°	63.8%	44.4%
5-10°	27.8%	35.5%
10-15°	1.5%	4.0%
black	6.9%	16.1%

	c-axis	
	YSZ	YBCO
0-5°	24.6%	41.1%
5-10°	62.2%	45.5%
10-15°	5.9%	1.4%
black	7.3%	12.0%

Table III shows a marked change in both in-plane and out-of-plane texture. The area fraction of sample with a small ( $0-5^\circ$ ) c-axis misalignment with respect to the sample normal direction increases by  $\sim 15\%$  in the superconductor compared to the buffer layer. In addition, the area fraction of sample with a larger ( $5-10^\circ$ ) c-axis alignment decreases by  $\sim 15\%$ . This result, that c-axis alignment improves in the superconductor, agrees with what other researchers have seen in x-ray diffraction experiments. Figure 4-27 shows x-ray rocking curves from all layers of a RABiTS-type coated conductor [13]. The out-of-plane alignment significantly improves from buffer to YBCO layer, as shown by the FWHM decreasing from  $5^\circ$  in the YSZ to  $1^\circ$  in the YBCO.

BEKP analysis on all layers of  $\text{BaF}_2$  YBCO coated conductor shows the texture transfer from the substrate to buffer layer to the superconductor. Most grain boundaries in the nickel were replicated in the YSZ with the same misorientation angle. Approximately 9% of the grain boundaries in the buffer layer had lower misorientation angles ( $1.9^\circ \pm 0.9^\circ$ ) compared to the underlying nickel grain boundaries, while 8% of YSZ boundaries had higher misorientation angles ( $1.6^\circ \pm 0.8^\circ$ ) than the underlying nickel boundaries. This variation in misorientation angle from substrate to buffer may be due to mosaic spread in the buffer layer. Mosaic spread in the superconductor may be responsible for the improvement in c-axis alignment in the YBCO compared to the buffer layer. However, the YBCO mosaic spread did not eliminate high angle grain boundaries, since  $>5^\circ$  boundaries were still too common in YBCO grain boundary maps.



#### **4.4. Summary**

Current barriers in high temperature superconductors occur on many length scales. Eliminating them is critical to making superconductors more viable for commercial applications. In state-of-the-art RABiTS-type YBCO coated conductors, the most significant barriers limiting current in short lengths of tapes are grain boundaries. On the scale of several tens of micrometers, the role of grain boundaries in the nickel substrate was investigated using a combination of plan-view SEM, BEKP analysis, MO imaging, and FIB cutting. The combined techniques showed enhanced magnetic flux penetration, and hence reduced  $J_c$ , in the YBCO above nickel grain boundaries that had  $\theta > 4-5^\circ$  in PLD and  $\text{BaF}_2$ -grown YBCO films. BEKP percolation maps show that the YBCO layer is single-crystal-like below a percolation limit of a few degrees. The BEKP grain boundary maps displays the constrictions of the current path on the scale of 50-100  $\mu\text{m}$ . BEKP grain orientation maps show improved c-axis texture in the superconductor layer, while BEKP grain boundary maps show evidence of remaining high angle ( $>5^\circ$ ) grain boundaries in the YBCO. The results of this study suggest that that the way to improve the superconducting properties in the YBCO is to eliminate  $\theta > 4^\circ$  boundaries in the nickel substrate in order to eliminate high angle boundaries in the superconductor.

## 4.5. References

- [1] A. Polyanskii, A. Gurevich, A.E. Pashitski, N.F. Heinig, R.D. Redwing, J.E. Nordman and D.C. Larbalestier, *Phys. Rev. B* **53** (1996) 8687-8697.
- [2] E. Pashitski, A. Gurevich, A.A. Polyanskii, D.C. Larbalestier, A. Goyal, E.D. Specht, D.M. Kroeger, J.A. DeLuca and J.E. Tkaczyk, *Science* **275** (1997) 367-369.
- [3] T.G. Truchan, F.H. Rountree, M.T. Lanagan, S.M. McClellan, D.J. Miller, K.C. Goretta, M. Tomsic, and R. Foley *IEEE Trans. Appl. Super* **10** (2000) 1130-3.
- [4] S.E. Babcock, C.Y. Yang, J.L. Reeves, Y. Wu, A.E. Pashitski, A. Polyanskii, D.C. Larbalestier, A. Goyal, M. Paranthaman, F.A. List, D.P. Norton, D.M. Kroeger, and A. Ichinose, *Materials-Science-Forum*, **294-296** (1999) 165-8.
- [5] J. Eickemeyer, D. Selbmann, R. Opitz, B. de Boer, B. Holzapfel, L. Schultz and U. Miller *Super. Sci. Tech.* **14** (2001).
- [6] A. Ichinose, C.Y. Yang, D.C. Larbalestier, S.E. Babcock, A. Kikuchi, K. Tachikawa, and S. Akita, *Physica C* **324** (1999) 113-22.
- [7] G. Sipos, B. Utz, W. Schmidt, H.W. Neumueller, and P. Mueller, *Physica-C* **.341-348** (2000) 1457-8.
- [8] He-Qing, D.K. Christen, R. Feenstra, D.P. Norton, M. Paranthaman, E.D. Specht, D.F. Lee, A. Goyal, and D.M. Kroeger, *Physica-C* **314** (1999) 105-11.
- [9] private communication with George Daniels

- [10] Goyal, S.X. Ren, E.D. Specht, D.M. Kroeger, R. Feenstra, D. Norton, M. Paranthaman, D.F. Lee and D.K. Christen, *Micron* **30** (1999) 463-478.
- [11] A.J. Schwartz, J. Kumar, B.L. Adams, *Electron Backscatter Diffraction in Materials Science*, Plenum Publishers, 2000.
- [12] A.P. Malozemoff, S. Annavarapu, L. Fritzemeier, Q. Li, V. Prunier, M. Rupick, C. Thieme, and W. Zhang, *EUCAS conference proceedings*, (1999).
- [13] D. Norton, *Ann. Rev. Mat. Sci.*, **28** (1998) 299-343 and references contained therein.

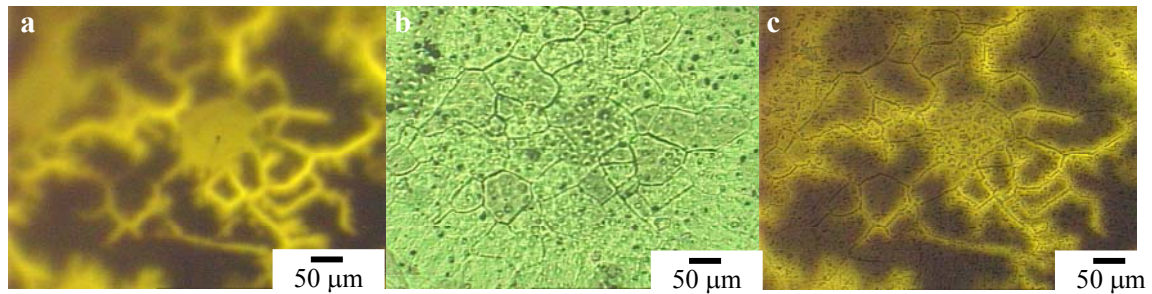


Figure 4-1. Images of YBCO coated conductor surface: (a) MO image; (b) light microscope image; (c) overlay MO and light microscope images to show that many, but not all, boundaries that are visible in the light microscope image are visible in the MO image. Courtesy of Matt Feldmann.

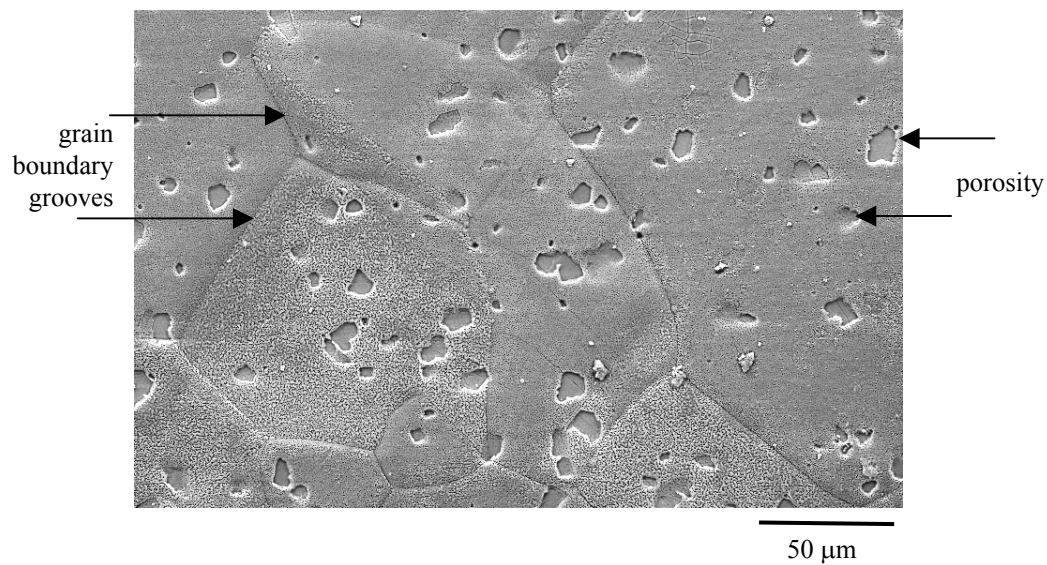


Figure 4-2. Plan view SEM image of a coated conductor showing grain boundary grooves and porosity in the PLD YBCO surface.

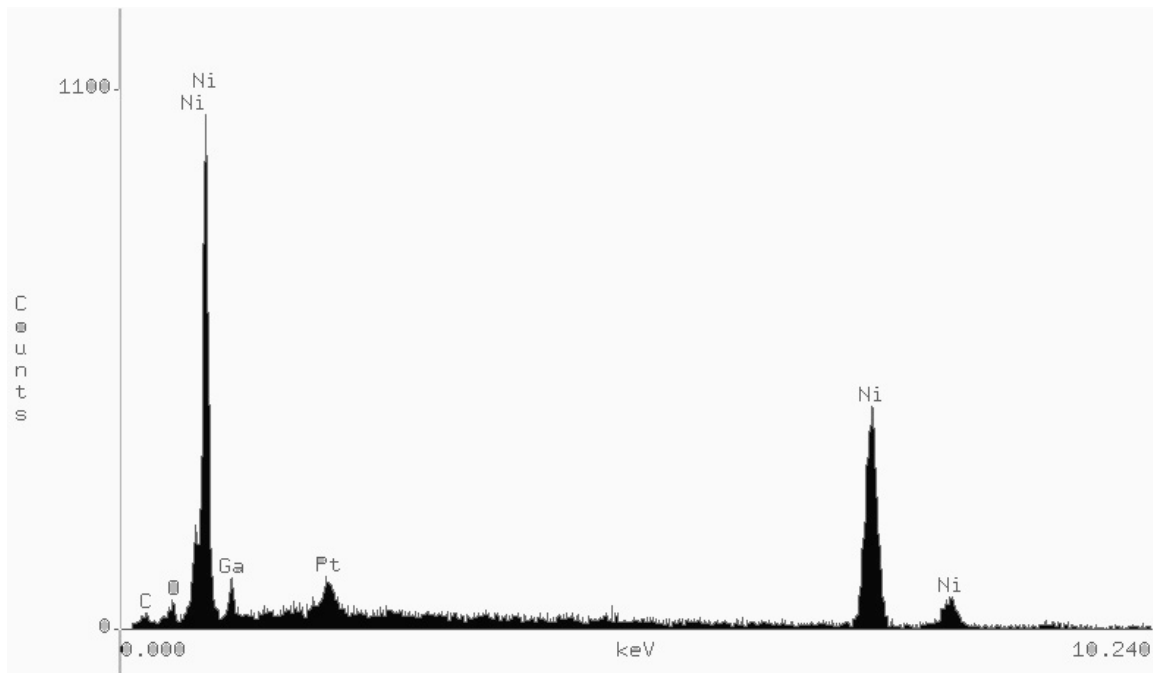


Figure 4-3. EDS spectrum showing bare nickel after chemical etching to remove YBCO and buffer layers. The Ga and Pt peaks remain after the FIB cutting of the Pt-coated surface.

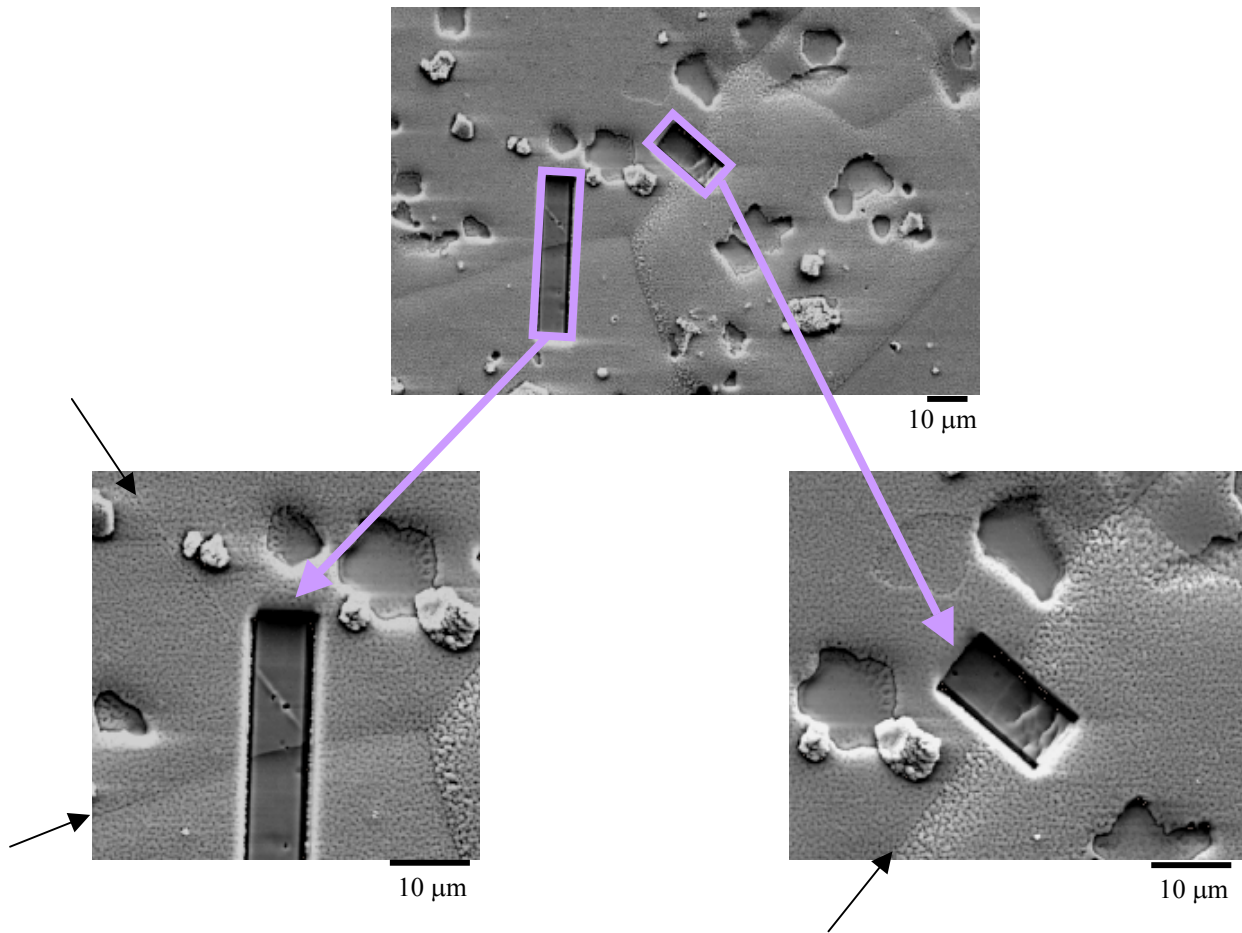


Figure 4-4. FIB trenches (outlined in purple) cut down to the nickel substrate of PLD YBCO coated conductor. The underlying nickel grain boundaries that correspond to YBCO boundaries (denoted with black arrows) are visible at the bottom of the FIB trenches.

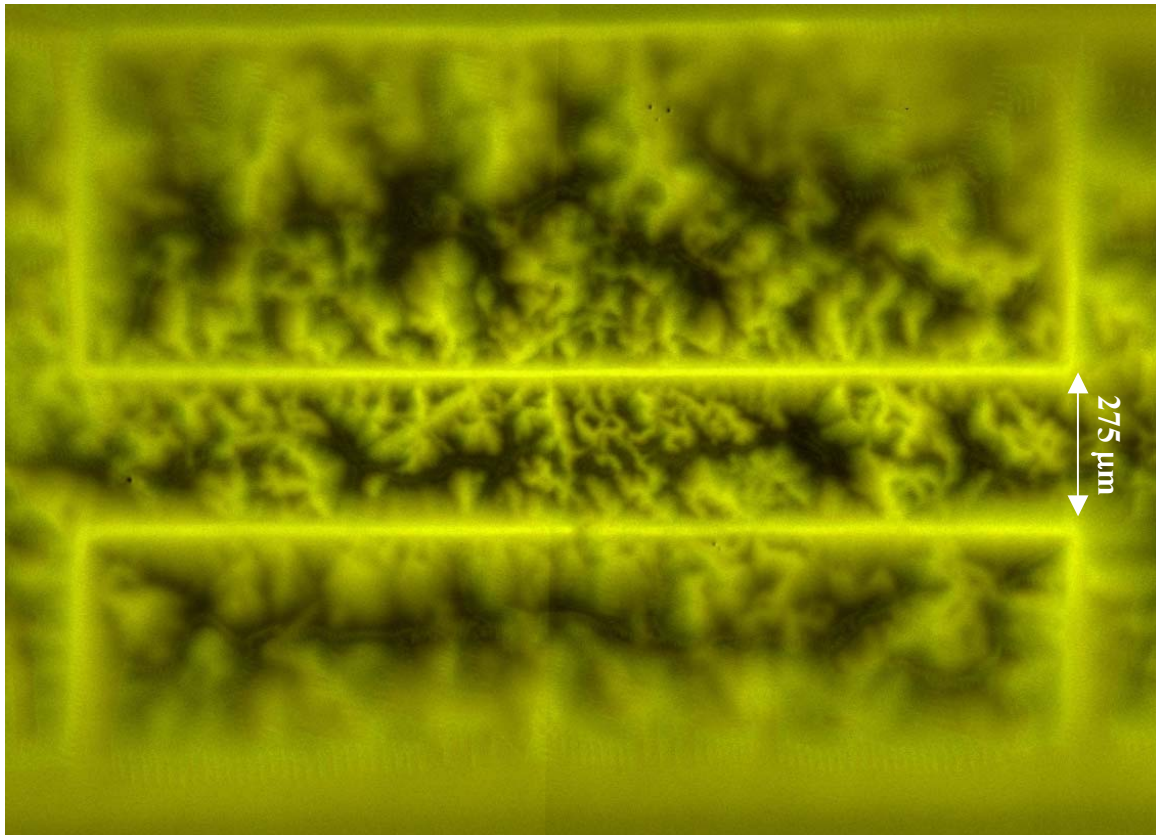


Figure 4-5. Zero-field cooled MO image of BaF<sub>2</sub> YBCO taken at an applied field of 400G at 77K. Bright regions are where magnetic flux has penetrated the sample. The long bright lines are where the laser was used to cut a bridge for electrical characterization of the YBCO. Courtesy of Matt Feldmann.

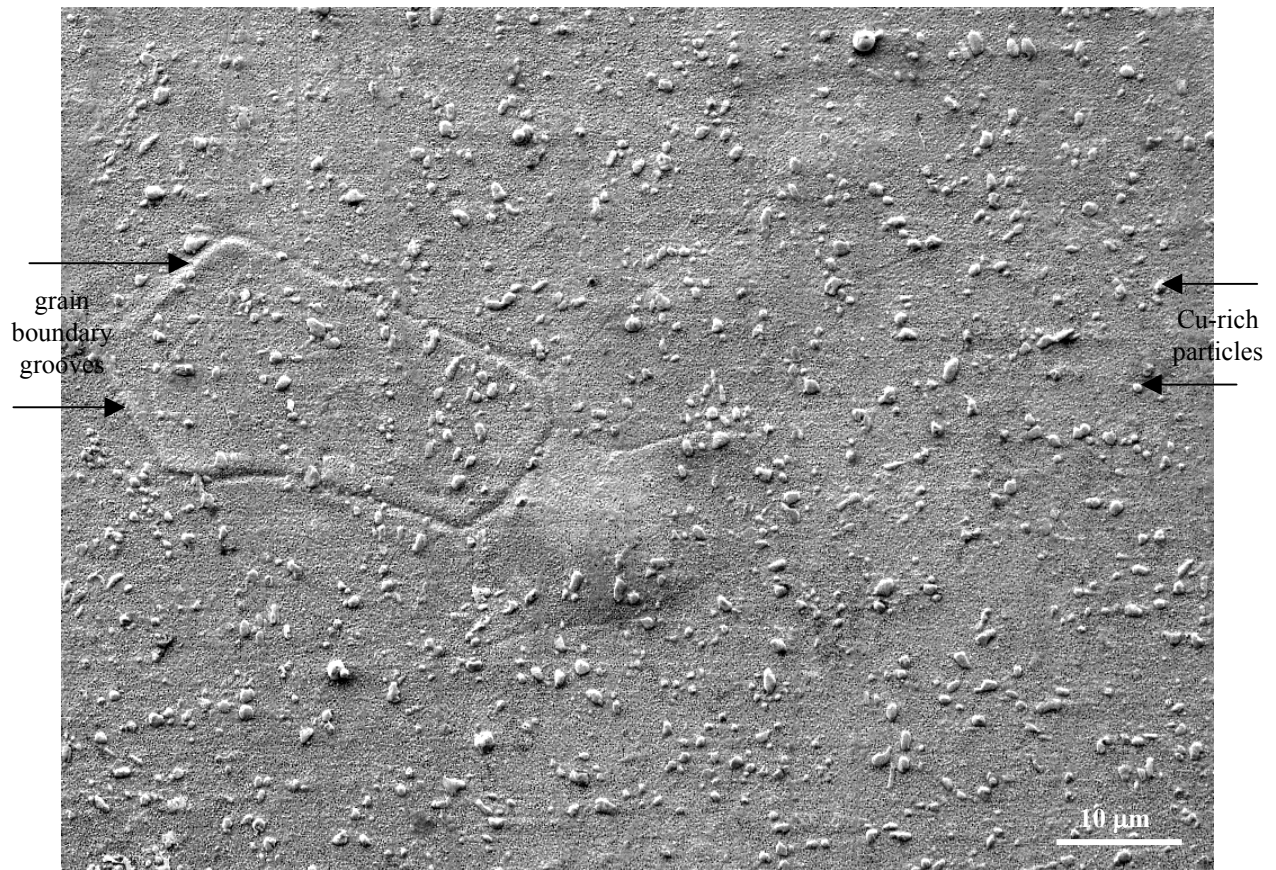


Figure 4-6. Plan-view SEM images of BaF<sub>2</sub>-grown YBCO showing grooved boundaries on the surface due to underlying nickel grain boundaries.

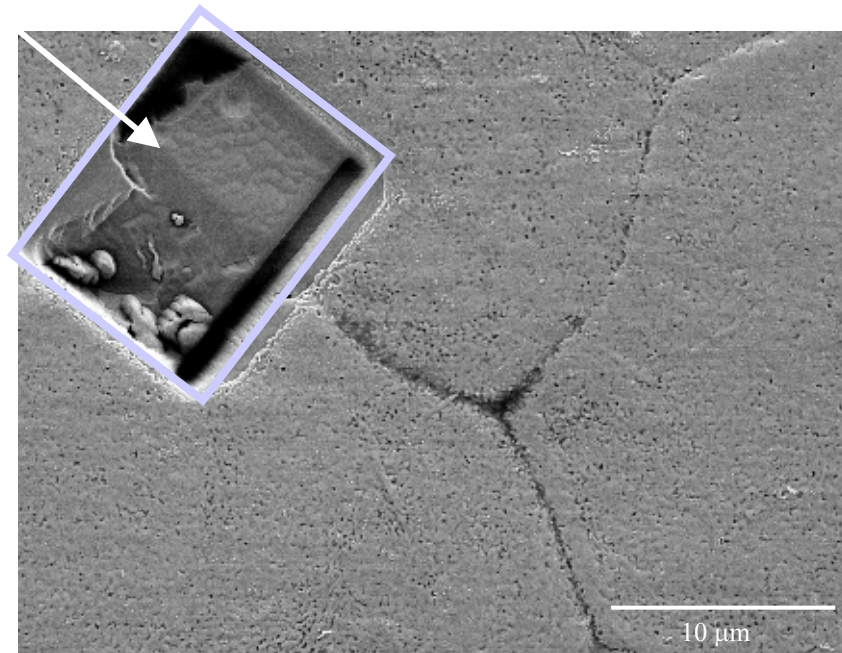


Figure 4-7. FIB trench (outlined in purple) cut in BaF<sub>2</sub> YBCO coated conductor. The underlying nickel grain boundary (marked with the white arrow) is visible at the bottom of the FIB trenches.

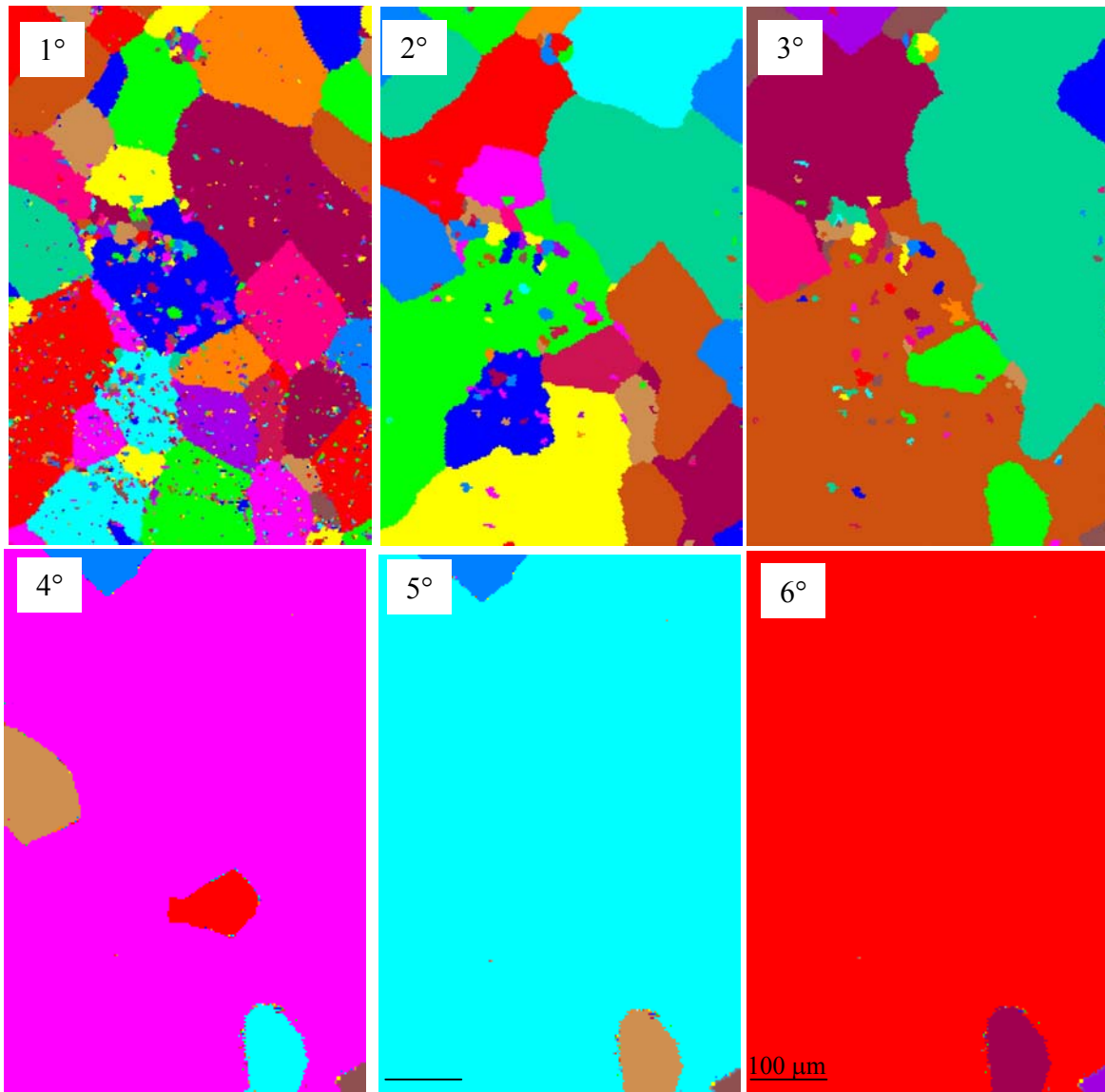


Figure 4-8. Percolation maps with varying tolerance angles of 1-6°. The colored speckles in the maps are unfiltered noise in the BEKP data.

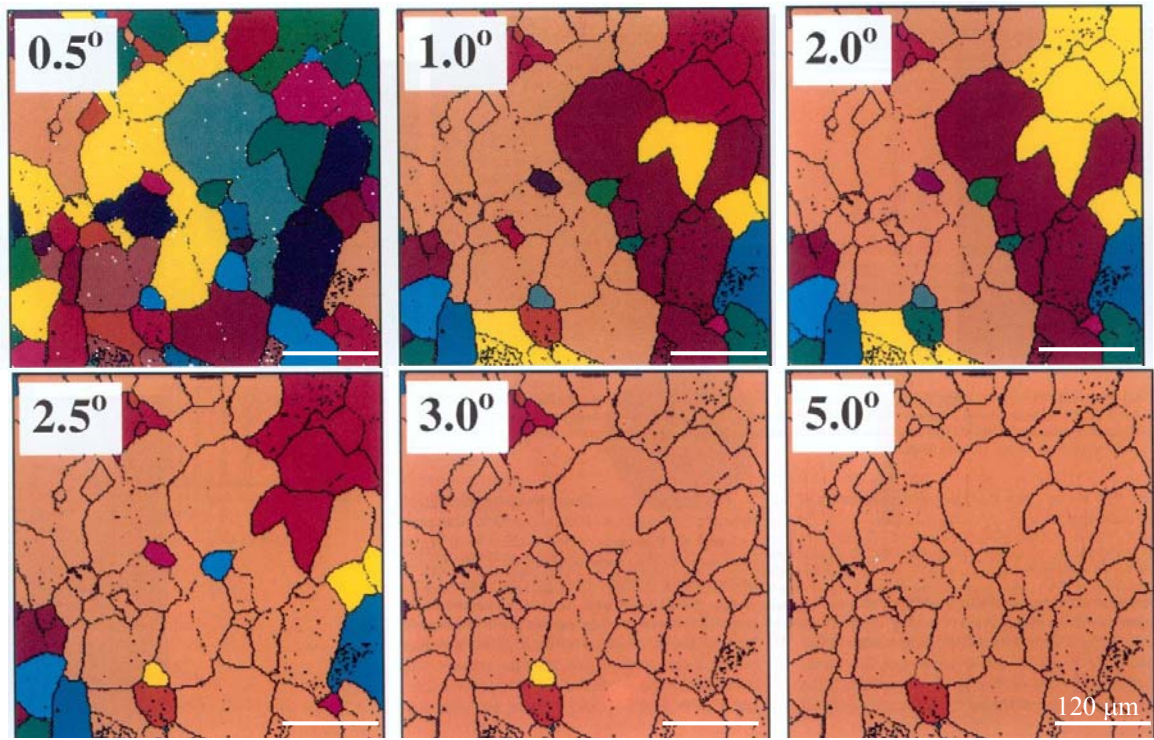


Figure 4-9. Percolation maps on nickel substrates of coated conductors with varying tolerance angles from [10].

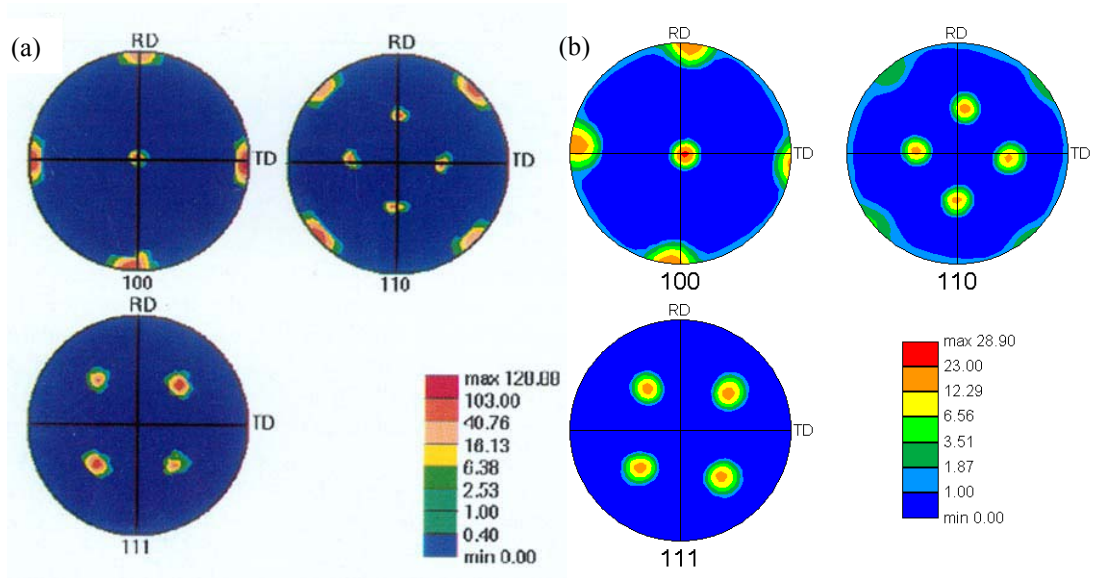


Figure 4-10. Pole figures for the BEKP data gathered from the region shown (a) in Figure 4-9 [10] and (b) in Figure 4-8.

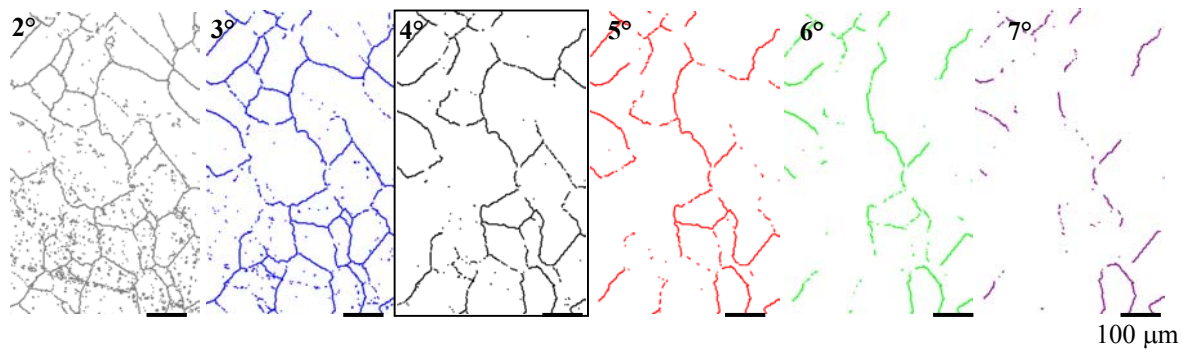


Figure 4-11. Grain boundary maps. The boundary criteria is 2, 3, 4, 5, 6, 7° from left to right, with the  $\theta > 4^\circ$  grain boundary map outlined for emphasis.

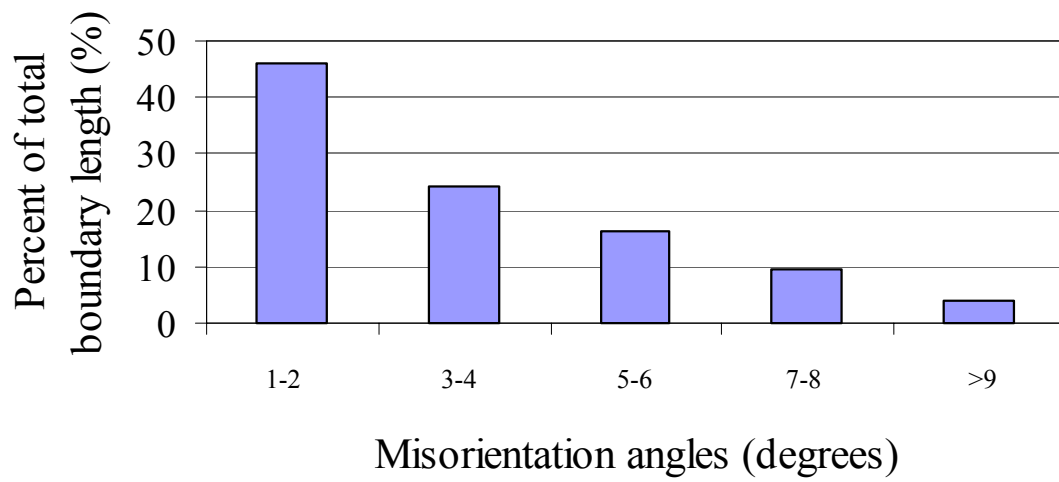


Figure 4-12. Distribution of grain boundary misorientations in the nickel substrate of the PLD YBCO sample from AFRL.

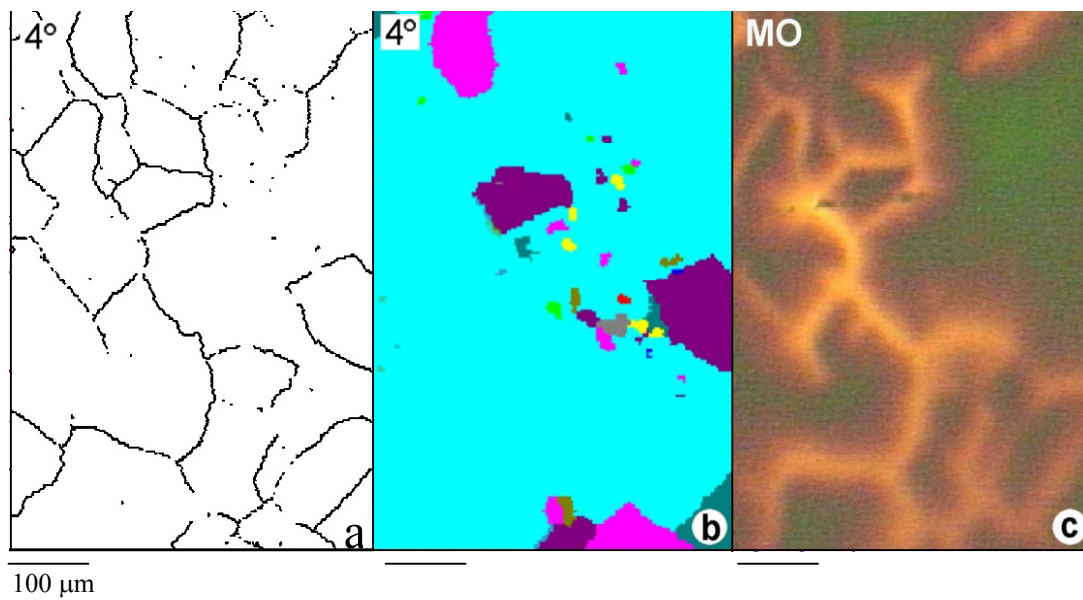


Figure 4-13. Comparison of (a) BEKP  $\theta > 4^\circ$  grain boundary map, (b)  $4^\circ$  percolation map, and (c) MO image (c) that shows a good correlation between the grain boundary map and the MO image.

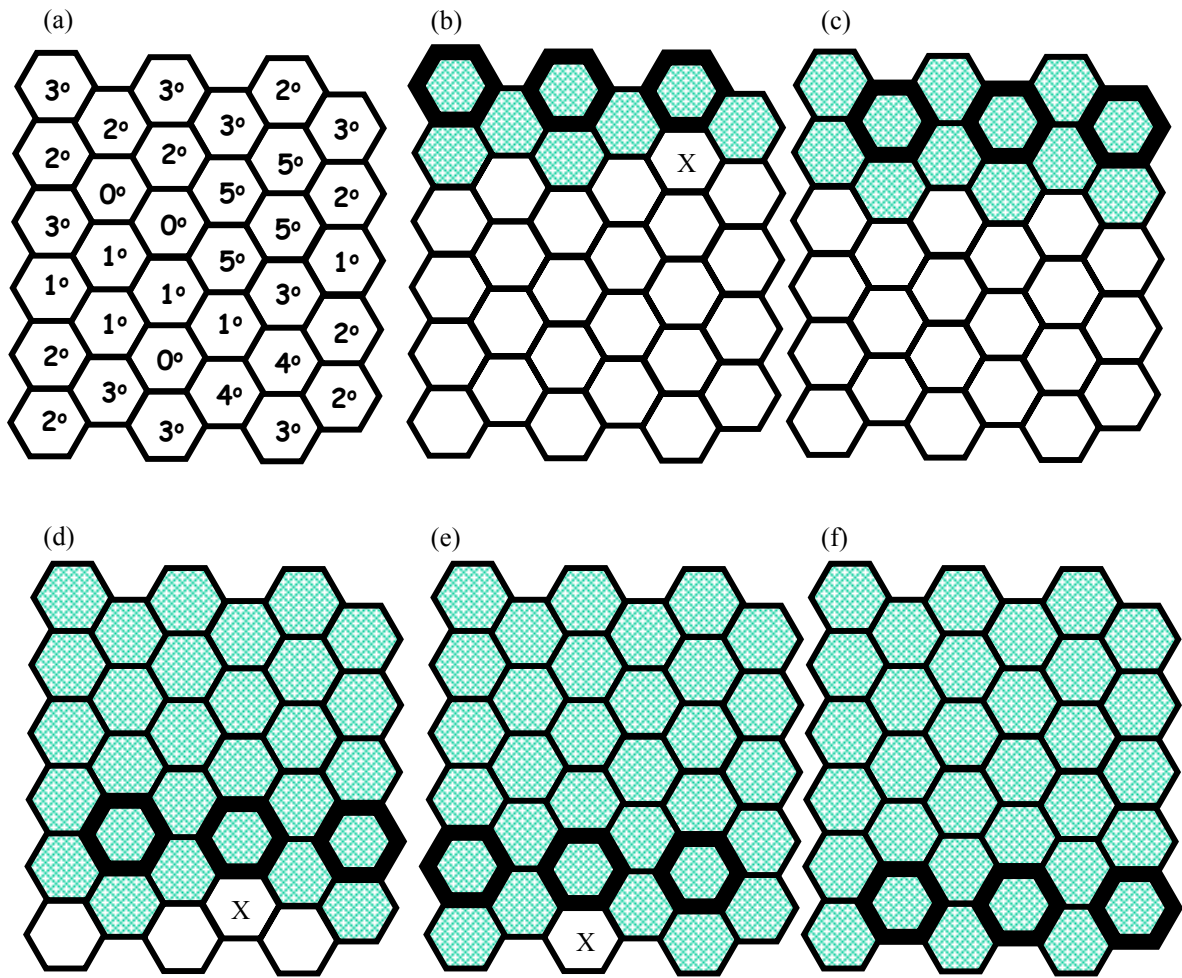


Figure 4-14. Diagrams showing generation of a  $2^\circ$  percolation map. See text for discussion.

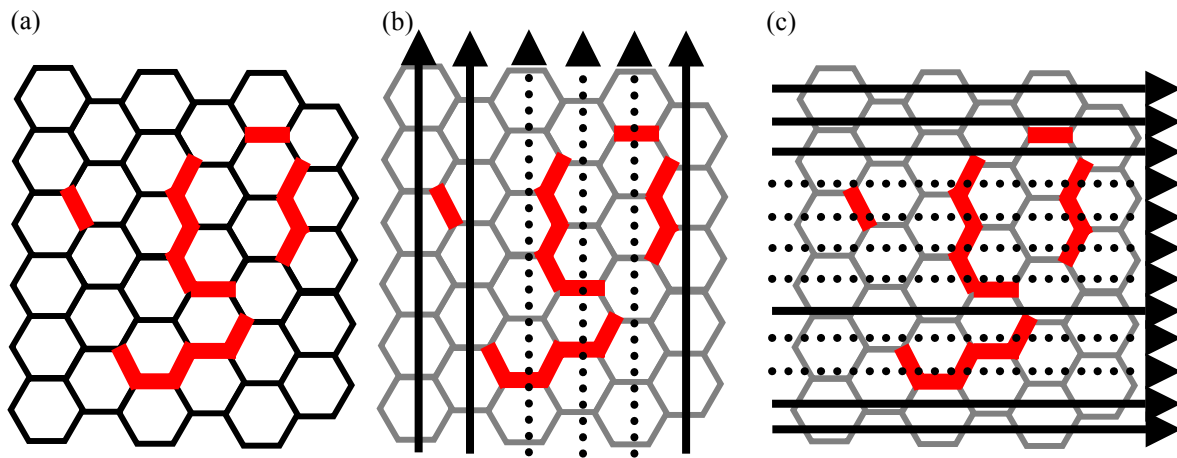


Figure 4-15. Diagrams showing (a) generation of grain boundary maps and (b, c) effect on current flow. In (a), red lines illustrate the position of grain boundaries greater than  $2^\circ$  based on the distribution of grain orientations shown in Figure 4-13a. In (b,c), dashed arrows show one-dimensional current flow that is blocked by grain boundaries greater than  $2^\circ$ .

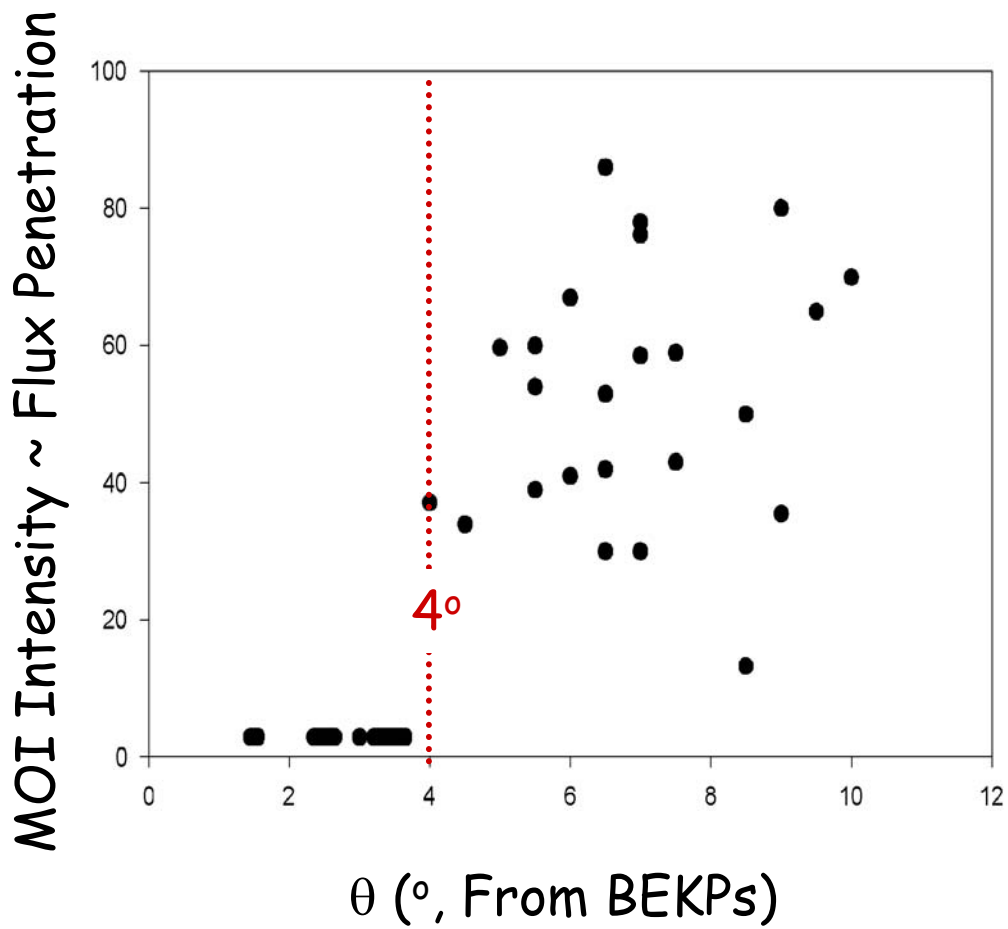


Figure 4-16. Plot of MO image intensity, which is proportional to magnetic flux penetration at the grain boundary, vs. grain boundary misorientation angle ( $\theta$ ).

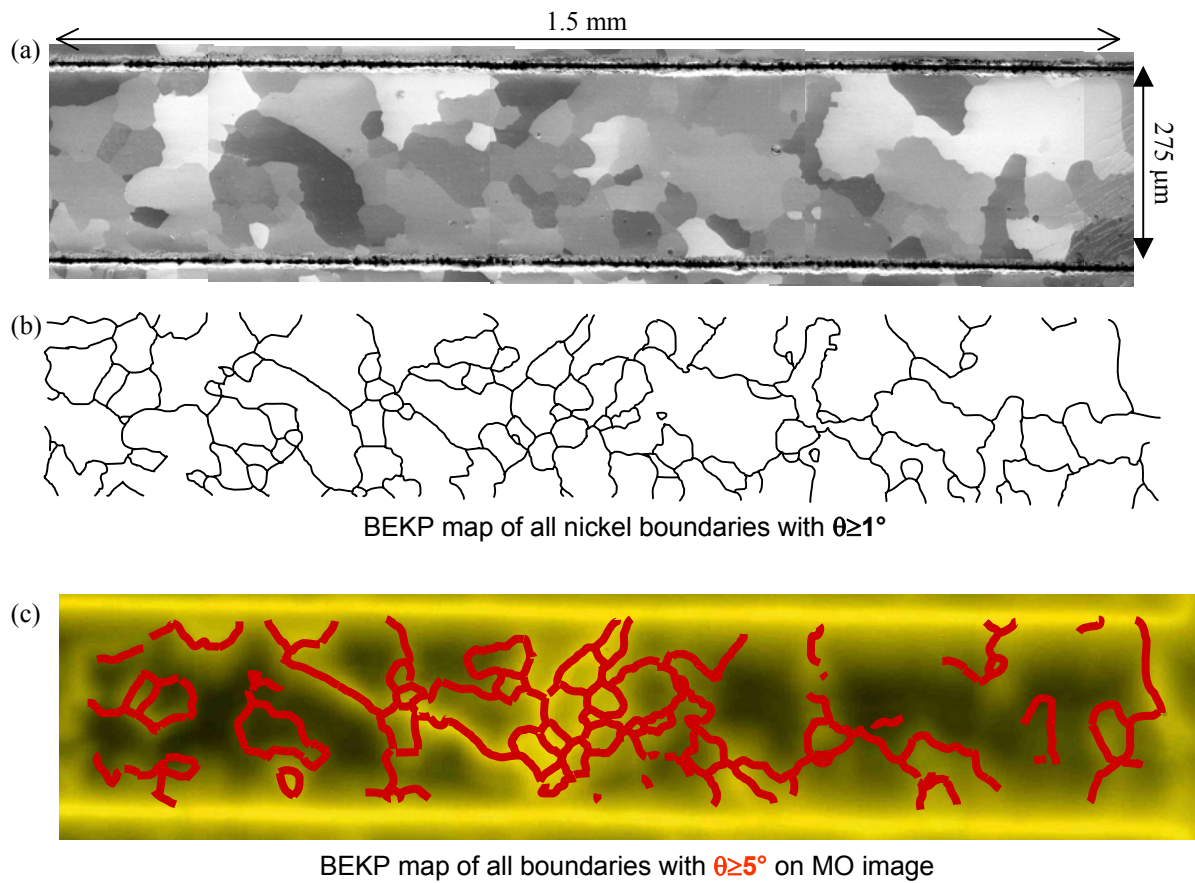


Figure 4-17. Data on a bridge cut into a  $\text{BaF}_2$  YBCO sample from ORNL: (a) SEM image of nickel grains after removing superconductor and buffer layers; (b) BEKP grain boundary map with  $\theta > 1^\circ$ ; (c) BEKP grain boundary map with  $\theta > 5^\circ$  overlaid on zero-field cooled MO image at 600G and 40K.

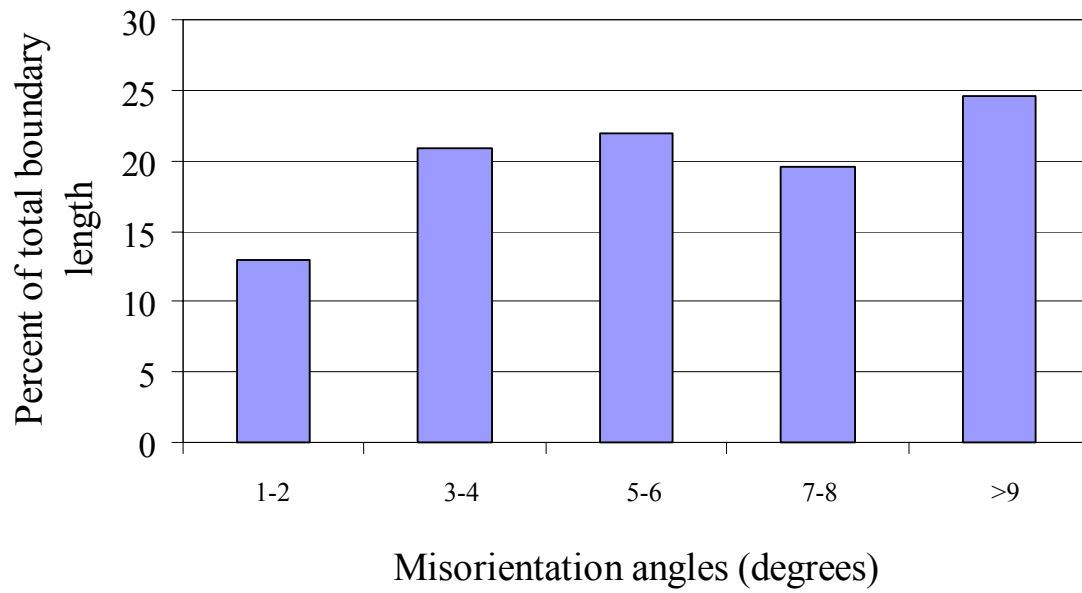


Figure 4-18. Distribution of grain boundary misorientations in the nickel substrate of the BaF<sub>2</sub> YBCO sample from ORNL.

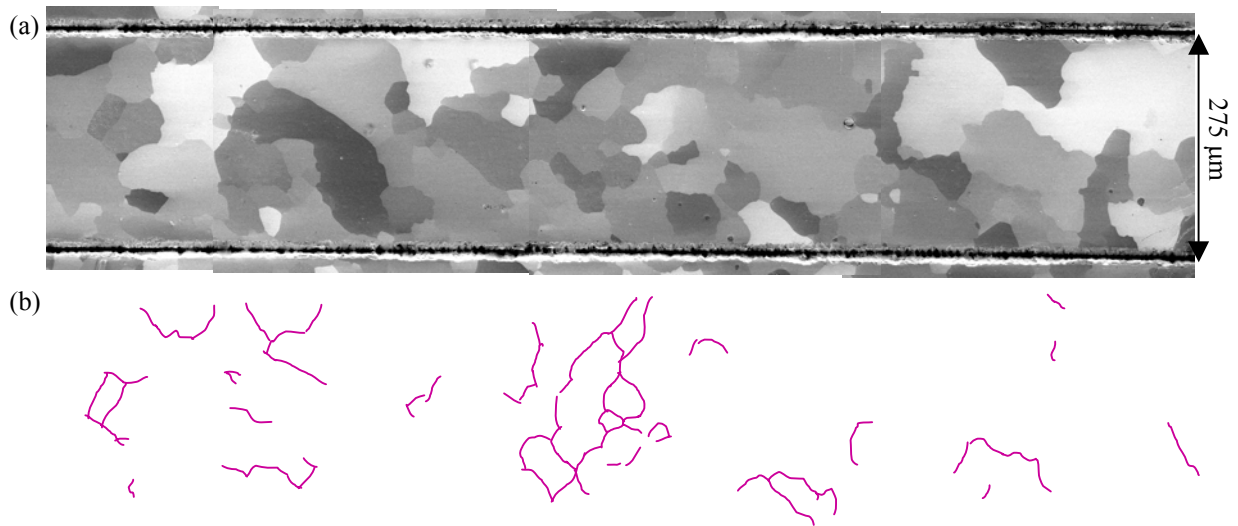


Figure 4-19. (a) SEM image of the nickel substrate and (b) BEKP grain boundary map with  $\theta > 9^\circ$  from bridge 1.

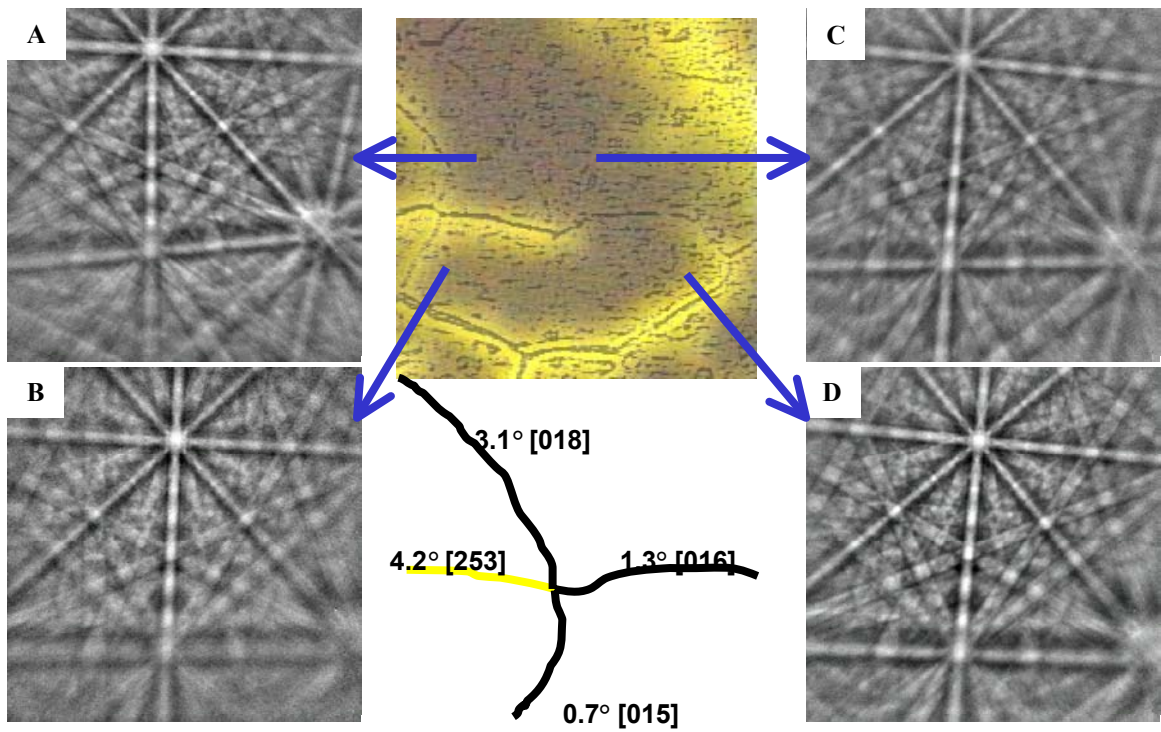


Figure 4-20. Representative Kikuchi patterns from three areas on the PLD YBCO surface. The amount of misalignment is qualitatively shown by the change in position of the Kikuchi pattern. The misorientation angle and axis are labeled in the schematic below the MO image.

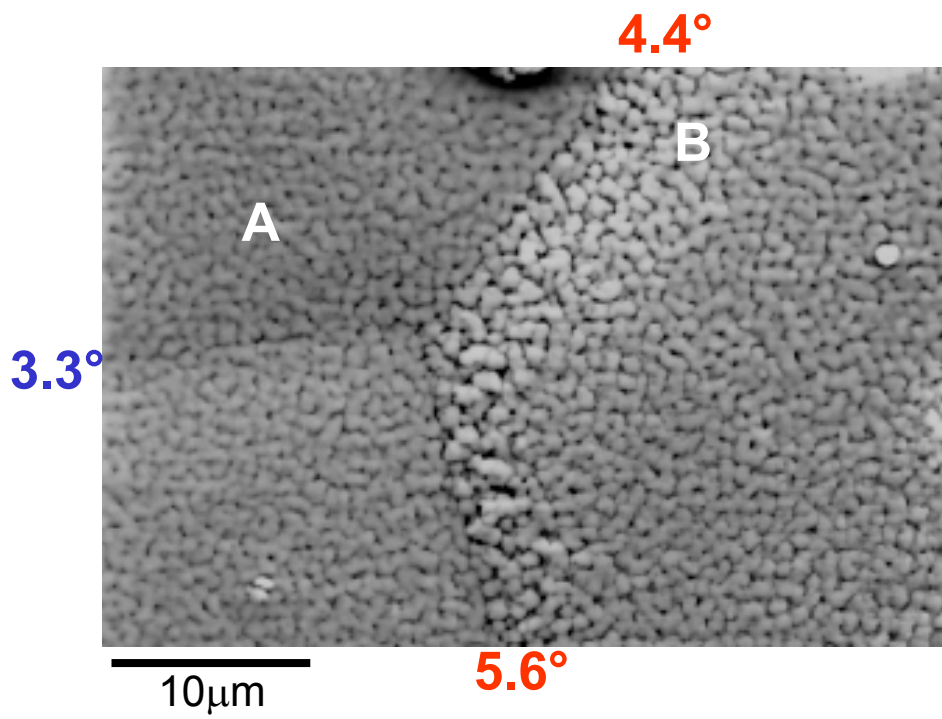


Figure 4-21. Morphology of PLD YBCO above nickel grain boundaries with labeled misorientations. The YBCO looks less dense and less well connected in region B compared to region A.

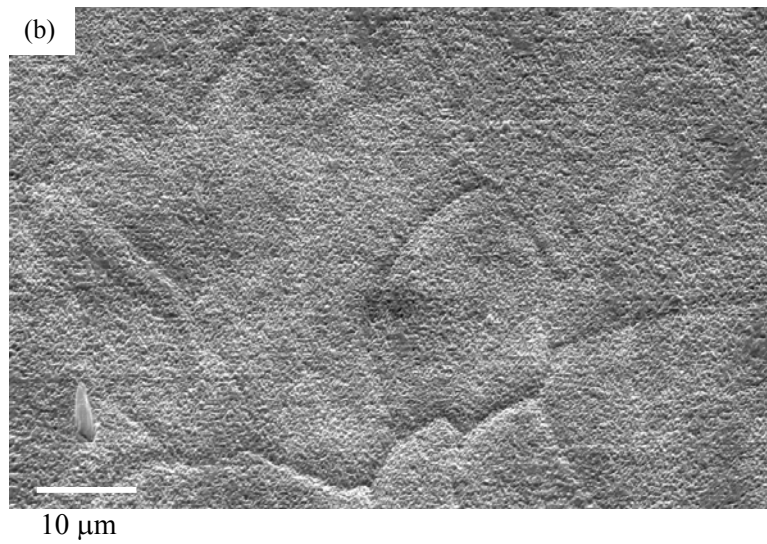
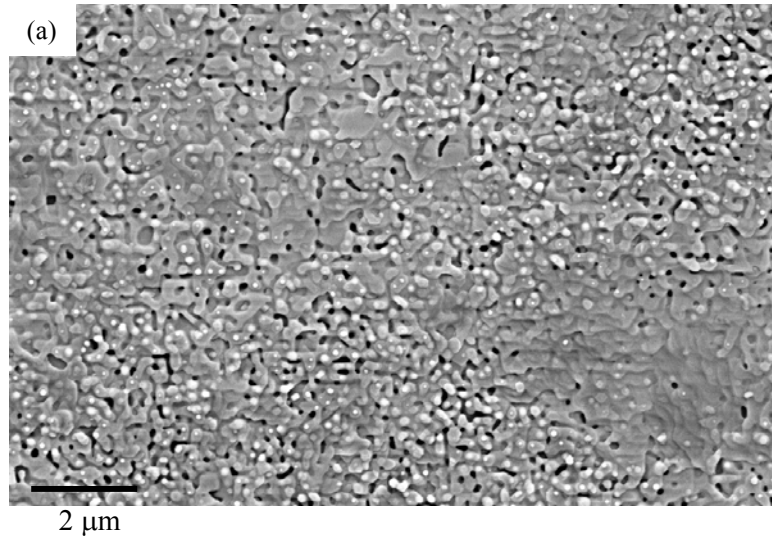


Figure 4-22. Secondary electron images of the  $\text{BaF}_2$  YBCO surface taken at (a) 5kV with no tilt and (b) 20kV with  $70^\circ$  tilt.

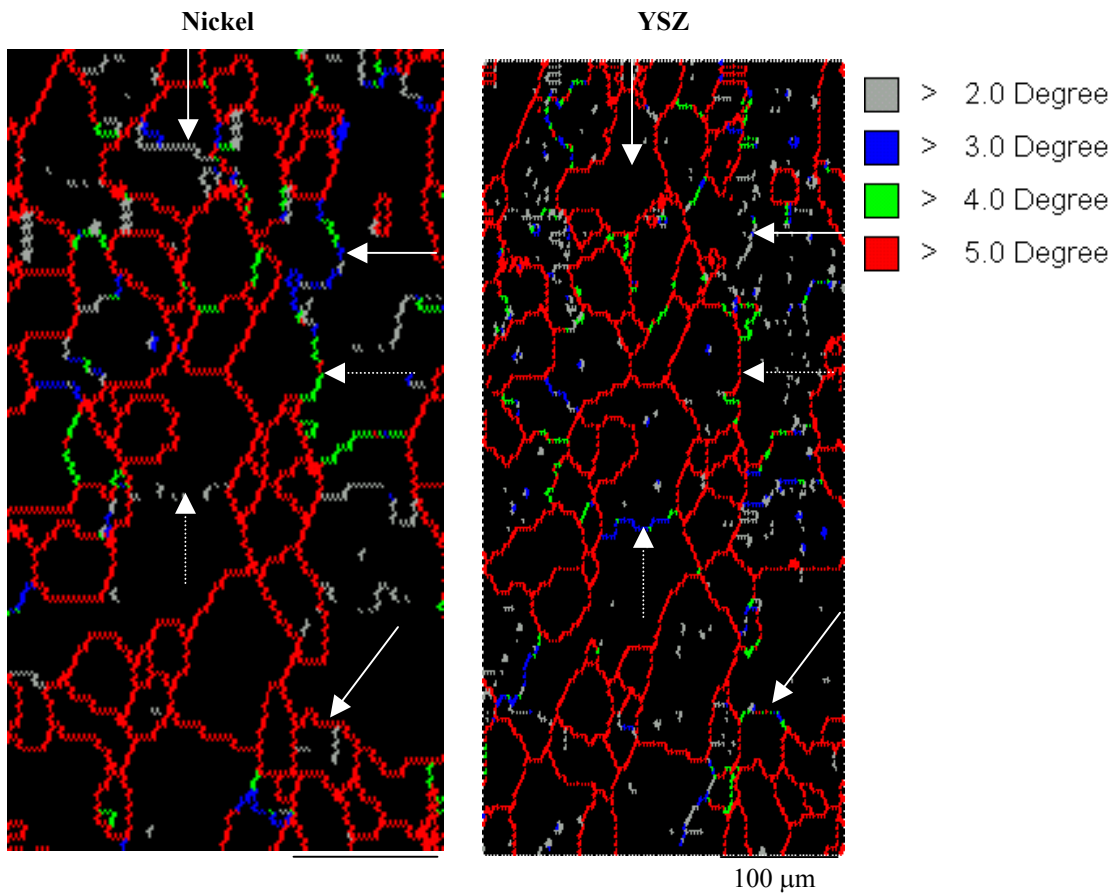


Figure 4-23a. BEKP grain boundary maps of the nickel and buffer layers of a BaF<sub>2</sub> YBCO coated conductor sample. Arrows highlight grain boundaries that change misorientation angle from substrate to buffer layer.

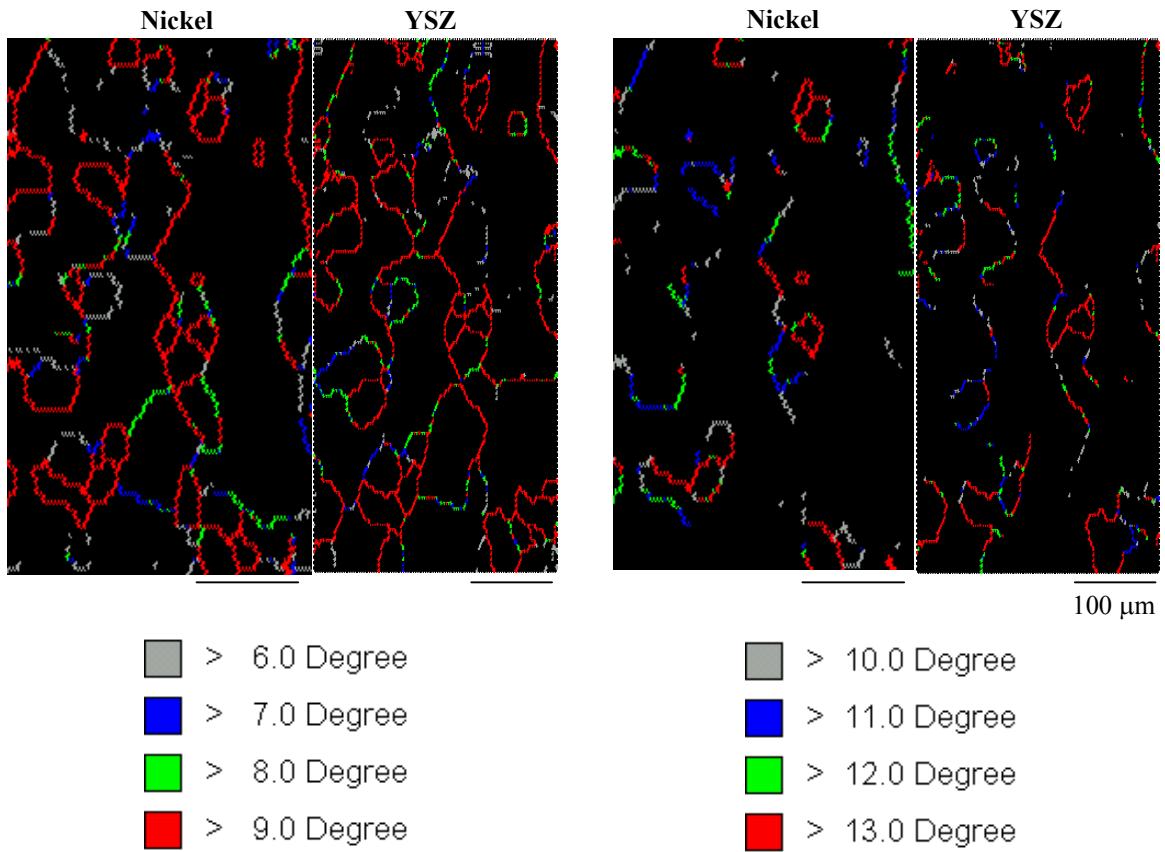


Figure 4-23b. BEKP grain boundary maps of the nickel and buffer layers of a BaF<sub>2</sub> YBCO coated conductor sample at more misorientation angle ranges.

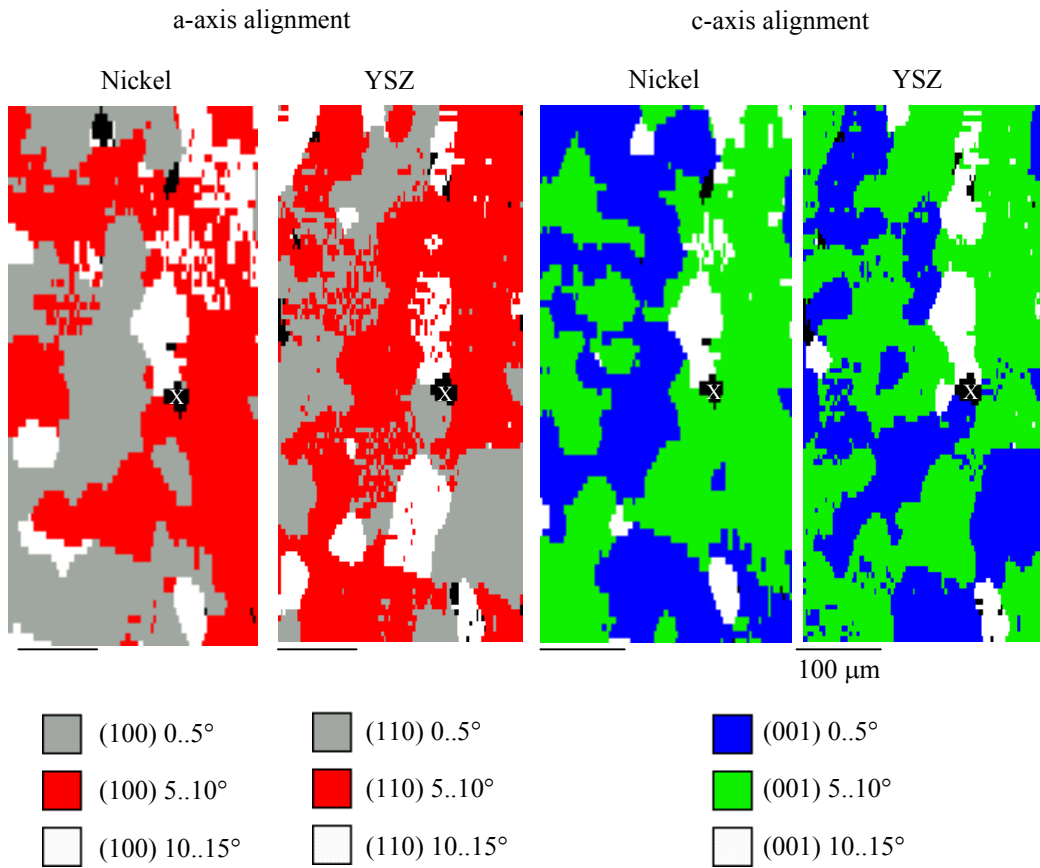


Figure 4-24. Comparison of BEKP grain orientation maps from the substrate and buffer layers.

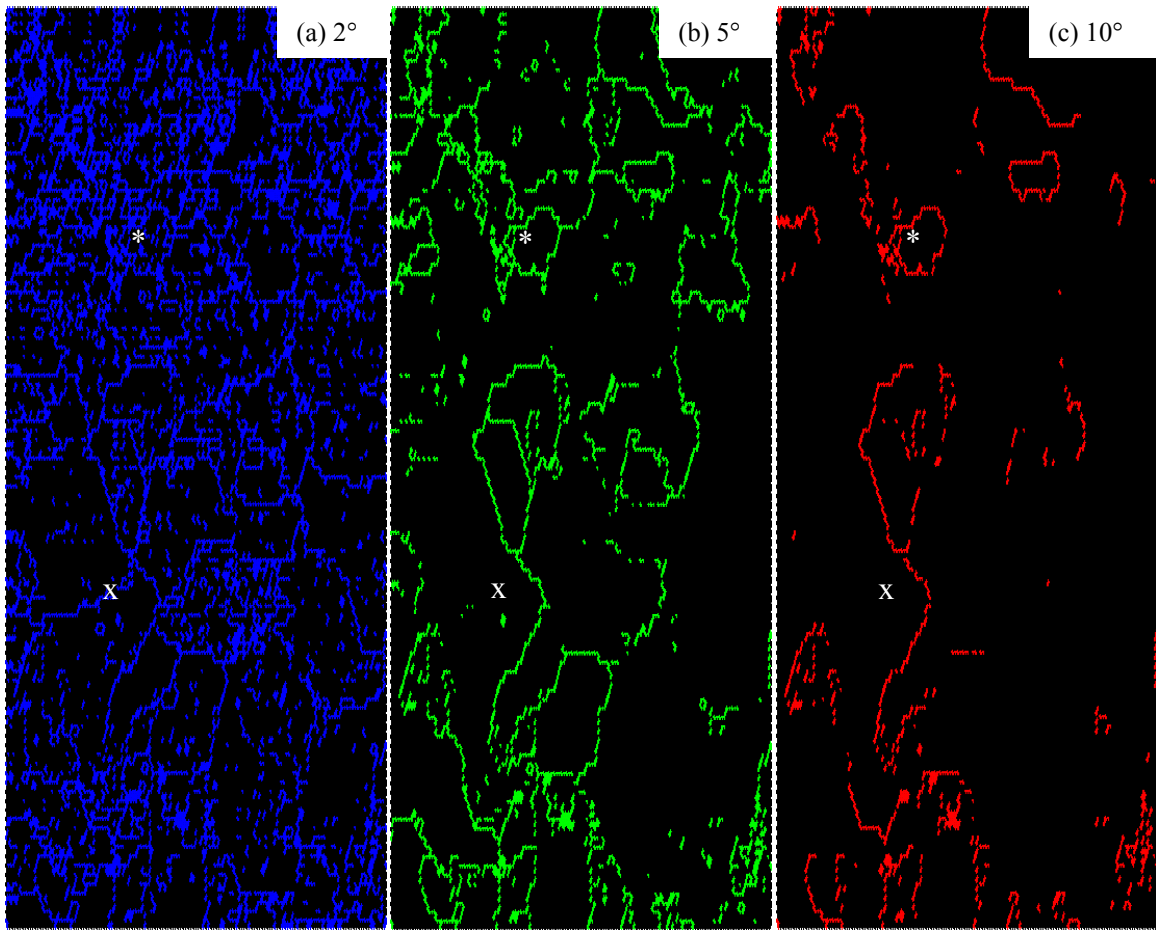


Figure 4-25. BEKP data from BaF<sub>2</sub> YBCO: (a) 2° grain boundary map, (b) 5 grain boundary map, (c) 10 grain boundary map. The “X” and “\*” mark the same point in all maps.

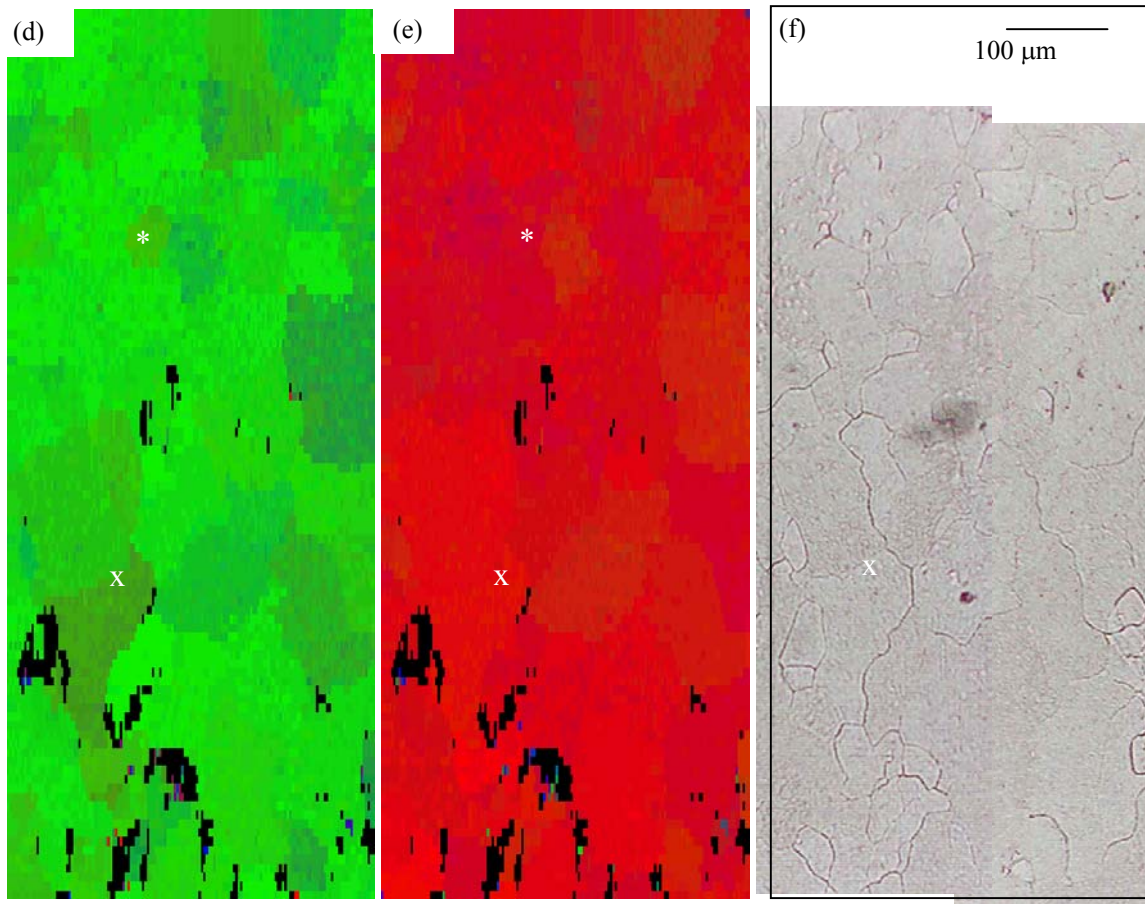


Figure 4-25 (cont.). BEKP data from  $\text{BaF}_2$  YBCO: grain orientation maps showing (d) a-axis alignment and (e) c-axis alignment, (f) light microscope image. The “X” and “\*” mark the same point in all maps.

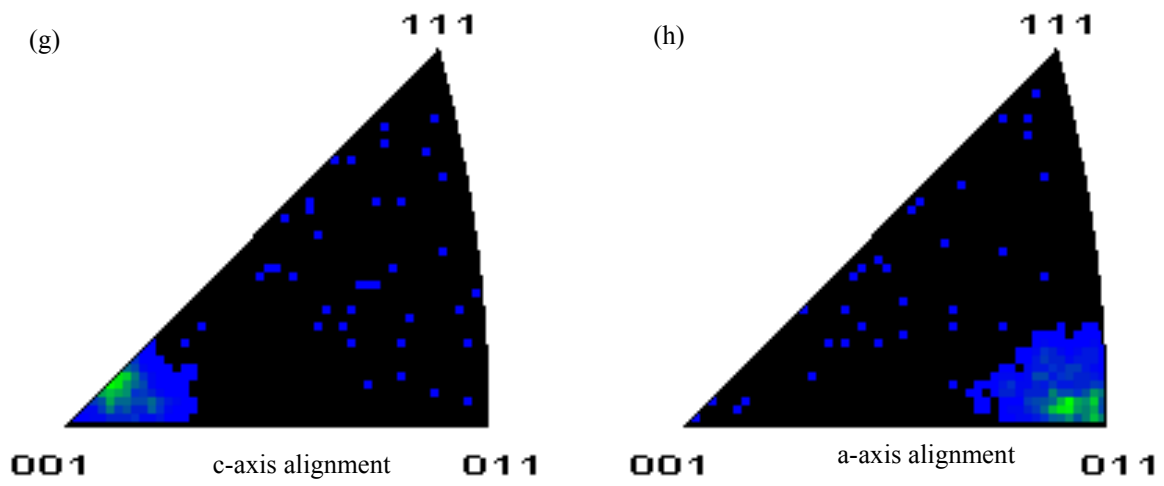


Figure 4-25 (cont.). BEKP data from BaF<sub>2</sub> YBCO: inverse pole figures showing (g) c-axis alignment and (h) a-axis alignment with respect to the sample reference frame.

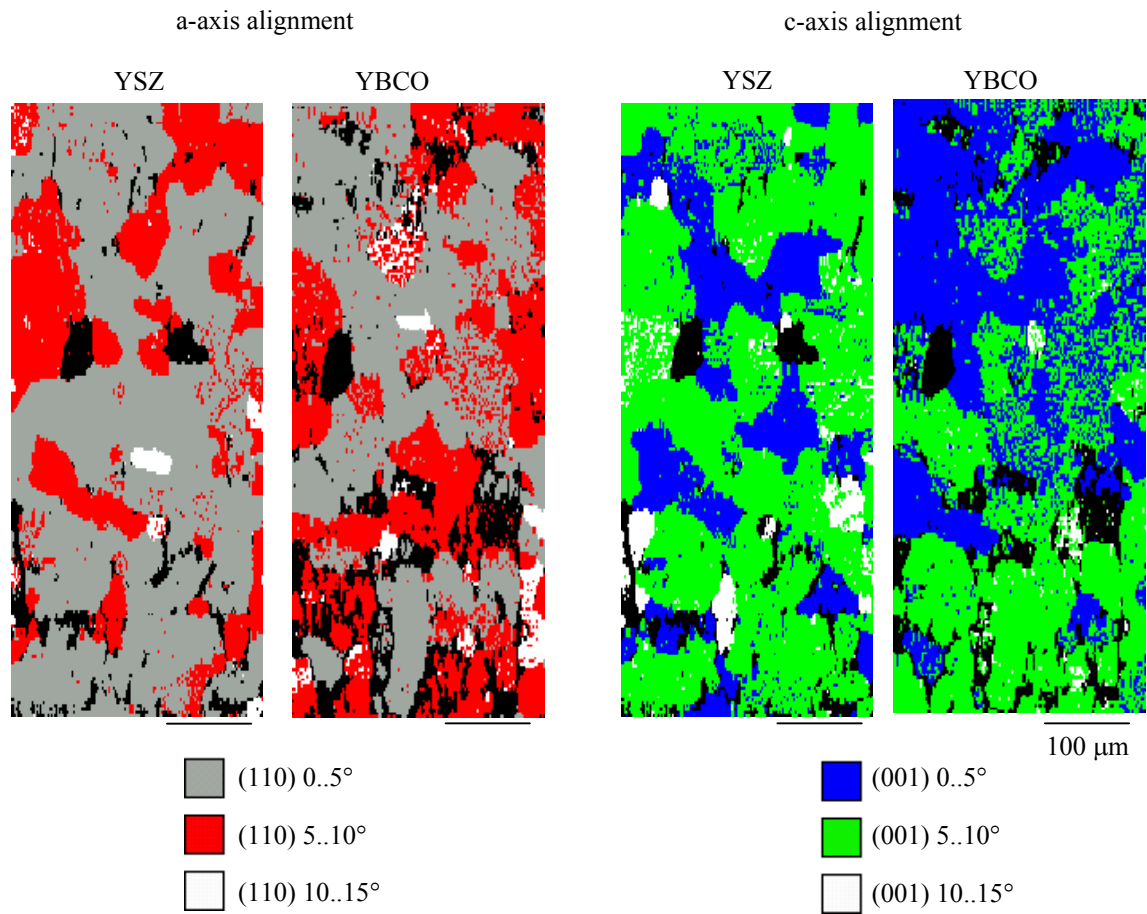


Figure 4-26. Comparison of the grain orientation maps from the buffer and superconductor layers.

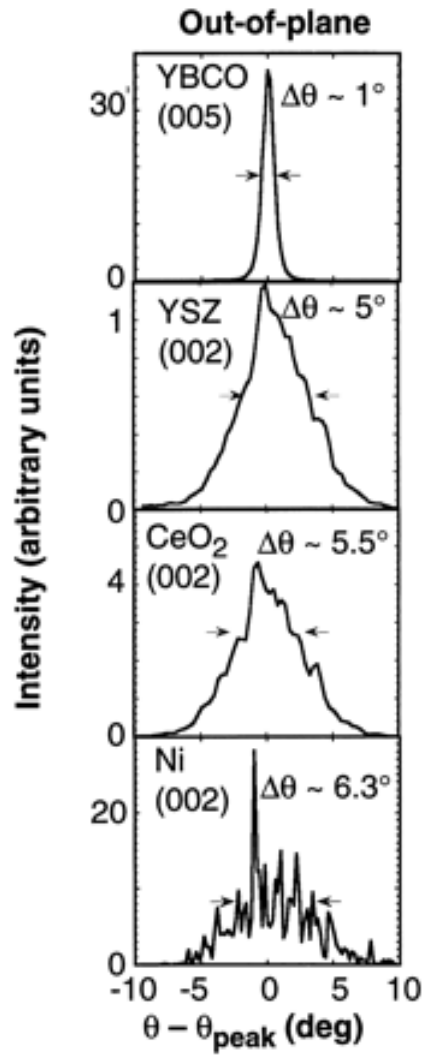


Figure 4-27. Comparison of the out-of-plane, or c-axis, texture in all layers of a RABiTS-type coated conductor. From [13].

## 5. Conclusions

BSCCO is the first generation high temperature superconductor wire to come to market. Specifically, long (kilometer) lengths of silver-sheathed Bi-2223 wires, tapes and multifilaments are commercially produced for electric power applications such as motors, generators, transformers, and fault current limiters. Bi-2212 wire is currently being produced for high field applications such as an insert magnet to increase the field strength of magnetic resonance imaging (MRI) devices.

This thesis has described the microstructural improvements in Bi-2212 tapes and multifilaments using overpressure processing, developed here at UW-Madison, and PAIR processing, developed in Japan. Overpressure processing was shown to stop the bubbling of the silver sheath and decrease porosity in the Bi-2212 core. PAIR was found to reduce porosity and the volume fraction of second phase particles and optimize grain alignment at the superconductor/silver interface. Applying pressure during or incorporating pre-annealing into the heat treatment of industrially produced Bi-2212 conductors will improve the current-carrying capability of the superconductor.

Bi-2212 materials are used for only a narrow range of applications at low temperatures (~20K). Bi-2223 is more useful for weak field applications such as cables at higher temperatures near 77K and at 25-30 K for field coils for transformers and for motors. However, there may be limitations to the commercial viability of Ag-sheathed Bi-2223 and Bi-2212 conductors, as the price of silver always has the potential to be a major raw material cost in the production of these

BSCCO conductors. To get the cost per kiloamp-meter down, it is essential to raise the current density. Understanding and engineering out barriers to current flow, as my thesis focus has shown, is an important way to do this.

YBCO coated conductors are the second generation of high  $T_c$  superconductor wire. The advantages of YBCO coated conductors compared to BSCCO materials are better performance (higher  $I_c$  and higher  $J_c$  on the order of  $MA/cm^2$ ) in high external applied magnetic fields at 77K and less expensive substrate materials (nickel is less expensive than silver). Currently, the coated conductor technology is not as mature as the BSCCO technology. Companies and national labs are still trying to make microstructurally and electromagnetically uniform coated conductors in meter long lengths. YBCO coated conductors will not be able to compete with BSCCO until kilometer lengths of YBCO can be produced and have uniform properties.

This thesis has shown that a major limitation in RABiTS-type coated conductors is the imperfect texture of the metal substrate in which moderately high angle grain boundaries ( $\theta > 5^\circ$ ) are retained in the microstructure. This work also showed that best way to illustrate current barriers due to the non-optimized texture is with grain boundary and grain orientation maps instead of BEKP percolation maps. BEKP grain boundary maps and MO images showed that the  $\theta > 4-5^\circ$  grain boundaries in the nickel substrate correspond to regions of reduced  $J_c$  in the superconductor. This work has also shown that most grain boundaries in the nickel, even high angle boundaries, were replicated in the buffer layer. Also, the YBCO mosaic spread did not eliminate high angle grain boundaries, since  $\theta > 5^\circ$  boundaries were still seen in a series of YBCO grain boundary maps that spanned approximately  $1 \text{ mm}^2$  of the sample surface. BEKP grain

orientation maps showed improvement in the c-axis alignment of the YBCO grains compared to the buffer layer, which is consistent with published x-ray diffraction studies.

Improving the texture of the RABiTS substrate by eliminating or reducing high angle grain boundaries in the nickel will be a major improvement to YBCO coated conductors. In short, this study has shown that better substrates will make better YBCO coated conductors.

## Appendix

### **Research-Related Publications**

Reeves, et al. Current Barriers in Y-Ba-Cu-O Coated Conductors, *IEEE Trans. Appl. Supercon.* **11** (1) pp. 3863-7, 2001.

Feldmann, Reeves, et al. Magneto-Optical Imaging of Transport Currents in  $\text{YBa}_2\text{Cu}_3\text{O}_{7-x}$  on RABiTS, *IEEE Trans. Appl. Supercon.* **11** (1) pp. 3772-5, 2001.

Reeves, et al. Effect of PAIR Process on Microstructure of Ag-Sheathed Bi-2212 Tapes, *Physica C* **341-348** pp. 2021-2022, 2000.

Rikel, Reeves, et al. Effect of Various Processing Variables on Grain Alignment at Bi-2212/Ag Interface, *Physica C* **341-348** pp. 2573-2574, 2000.

Feldmann, Reeves, et al. Influence of nickel substrate grain structure on  $\text{YBa}_2\text{Cu}_3\text{O}_{7-x}$  supercurrent connectivity in deformation-textured coated conductors, *Appl. Phys. Lett.*, **77** (18), pp. 2906-8, 2000.

Lehndorff, Reeves, et al. Influence of Thickness on Overpressure-processed Bi-2212/Ag Multifilamentary Tapes, *European Conference on Applied Superconductivity (EUCAS) proceedings*, 1999.

Reeves, et al. Effects of Overpressure Processing on Porosity in Bi-2212 Multifilamentary Wires with Various Geometries, *IEEE Trans. Appl. Supercon.* **9** (2) pp. 1836-9, 1999.

Babcock, Dunn, Zhou, Reeves, et al. Microstructure of Epitaxial (InGa)As on a Borosilicate Glass-Bonded Compliant Substrate, *Mater. Sci. Forum* **294**, pp. 783-6, 1999.

Babcock, Yang, Reeves, et al. Electrical Connectivity and Microstructure in  $\text{YBa}_2\text{Cu}_3\text{O}_{7-\delta}$  Films on Rolling-Assisted Biaxially-Textured Substrates, *Mater. Sci. Forum* **294**, pp. 165-8, 1999.

Reeves, et al. Overpressure Processing of Ag-Sheathed Bi-2212 Tapes, *IEEE Trans. Appl. Supercon.* **7** (2) pp. 1541-1543, 1997.

Pierson, Reeves, et al. Total Sputtering Yield of Ag/Cu Alloys for Low Energy Argon Ions, *Nucl. Instrum. Meth. B* **108** (3) pp. 290-299, 1996.

### **Research-Related Oral and Poster Presentations**

Reeves, et. al. Nickel Grain Boundary Induced Current Barriers in YBCO Coated Conductors, symposium talk presented at the Materials Research Society (MRS) conference, Boston, MA, November 2000.

Reeves, et. al. Influence of the Substrate Grain Structure on the Structure and Properties of YBCO Coated Conductors, invited talk at ASC 2000, Virginia Beach, VA, September 2000.

Larbalestier, Babcock, Daniels, Feldmann, Gurevich, Polyanskii, Reeves. Properties of Low Angle Grain Boundaries in High Temperature Superconductors, plenary talk presented at

the 6<sup>th</sup> International Conference on Materials and Mechanisms of Superconductivity and High Temperature Superconductors (M2S-HTSC-VI), Houston, TX, February 2000.

Babcock, Yang, Reeves, et al. Microstructure in YBCO Coated Conductors, symposium talk presented at the Materials Research Society (MRS) conference, Boston, MA, November 1999.

Feldmann, Reeves, et al. Influence of Nickel Substrate Grain Structure on YBCO Connectivity in Coated Conductors, poster presented at the 9<sup>th</sup> International Workshop on Critical Currents (IWCC), July 1999.

Reeves, et al. OIM Characterization of Metal Substrates for YBCO Coated Conductors, symposium talk presented at the American Physics Society (APS) conference, Los Angeles, CA, March 1998.

Lendorff, Reeves, et al. Overpressure Processing Effects on Microstructure and  $J_c$  of Ag-Sheathed Bi-2212 Multifilamentary Wires, poster presented at the International Cryogenic Materials Conference (ICMC), Portland, OR, July 1997.

Reeves, et al. Overpressure Processing of Ag-Sheathed  $\text{Bi}_2\text{Sr}_2\text{CaCu}_2\text{O}$  Tapes -- Effect on Microstructure and Critical Current, poster presented at the International Workshop on Superconductivity, Big Island, HI, June 1997.

Reeves, et al. Overpressure Processing of Ag-Sheathed Bi-2212 Coils, poster presented at the Materials Research Society (MRS) conference, Boston, MA, November 1995.

Zhang, Reeves, et al. Study on Melt Processing Long Lengths of Ag-Sheathed 2212 Tape, symposium talk presented at the Materials Research Society (MRS) conference, Boston, MA, November 1995.

### ***Teaching-Related Publications and Presentations***

Courter, Lewis, Reeves, et al. Aligning Foundation Coalition Core Competencies and Professional Development Opportunities: A University of Wisconsin – Madison Case Study in Preparing a New Generation of Engineers, accepted for publication in *American Society for Engineering Education conference proceedings*, 2001.

Reeves, et al. Change Agents: Immediately Implementable Teaching and Educational Hints from the Engineering Education Scholars Program, published in *American Society for Engineering Education conference proceedings*, 1999.

Reeves, et al. Course Portfolios: A Systematic Mechanism to Document Teaching and Learning, published in *Frontiers in Education conference proceedings*, 1998.

Reeves, et al. Course Portfolios: A Practical Tool for Teaching and Learning, workshop presented at the National Conference on the Education and Employment of Graduate Teaching Assistants, Minneapolis, MN, November 1997.